SPLITS:
A Spectral Light Transport Model
for
Sand

by

Bradley W. Kimmel

A thesis

presented to the University of Waterloo

in fulfillment of the

thesis requirement for the degree of

Master of Mathematics

in

Computer Science

Waterloo, Ontario, Canada, 2005

©Bradley W. Kimmel 2005

I hereby declare that I am the sole author of this thesis.

I authorize the University of Waterloo to lend this thesis to other institutions or individuals for the purpose of scholarly research.

Bradley W. Kimmel

I further authorize the University of Waterloo to reproduce this thesis by photocopying or other means, in total or in part, at the request of other institutions or individuals for the purpose of scholarly research.

Bradley W. Kimmel

Abstract

Despite the ubiquity of sands in outdoor environments, little attention has been paid to the predictive rendering of this medium. In this thesis, we present a new spectral light transport model for sand (SPLITS). The model simulates both the spectral and spatial (BRDF) responses of sand. Furthermore, the parameters specifying the SPLITS model are based on the physical and mineralogical properties of sand. The model is evaluated quantitatively, through comparisons with measured data. Good spectral reconstructions were achieved for the reflectances of several real sand samples. The model was also evaluated qualitatively, and compares well with descriptions found in the literature.

Acknowledgements

First, I would like to thank my advisor, Gladimir Baranoski, for his wisdom, insight, and his ability to see the way forward during periods of doubt. I would also like to thank my colleagues from the Natural Phenomena Simulation Group: Aravind Krishnaswamy, Michael Lam, and Denise Eng, as well as Ian Bell, my thesis readers Justin Wan and Peter Forsyth, and everyone else at the University of Waterloo who contributed their time and insight. I am also grateful to my parents, Bill and Gail, for their support in this endeavour. Finally, I would like to thank my wife, Erin, for her assistance with AutoCAD™, and for her immeasurable love and support, without which this would not have been possible.

This work is supported by the National Sciences and Engineering Council (NSERC Grant 213281) and the Canadian Foundation for Innovation (CFI Project 6218).

Table of Contents

1 Introduction **1**

2 Properties of Sand **5**

2.1 What is Sand? 5

2.2 Factors Affecting Light Transport 8

2.2.1 Mineral Composition 8

2.2.2 Water 9

2.2.3 Grain Size and Shape 9

2.2.4 Additional Factors 10

3 Related Work **13**

3.1 Geometric Models 13

3.1.1 Landscape Formation 14

3.1.2 Sand Displacement 14

3.2 Reflection Models 15

3.2.1 General Models 15

3.2.2 Related Models 16

3.2.3 Simulation of Specific Effects 16

4 Optics **19**

4.1 Conventions and Nomenclature 19

4.1.1 Complex Refractive Index 19

4.2 Birefringence 21

4.3 Mixed Materials 21

4.4 Generalization of Snell's Law for an Absorbing Medium 22

4.5 Reflectance at a Plane Surface 23

5 Data **25**
5.1 Mineral Properties . . . 25
5.1.1 Occurrence of Iron Oxides . . . 25
5.1.2 Refractive Indices . . . 26
5.1.3 Density . . . 28
5.2 Grain Properties . . . 28
5.2.1 Particle Size Distribution . . . 29
5.2.2 Roundness and Sphericity . . . 29
5.2.3 Coating Thickness . . . 30
5.3 Properties of a Sand Medium . . . 30
5.3.1 Depth . . . 30
5.3.2 Porosity . . . 31
5.3.3 Water Content . . . 31

6 The SPLITS Model **39**
6.1 Concept . . . 39
6.2 Construction . . . 40
6.2.1 Extended Boundaries . . . 42
6.2.2 Pore Space . . . 42
6.2.3 Particle Geometry . . . 42
6.2.4 Particle Composition . . . 44
6.2.5 Particle Types . . . 44
6.2.6 Shape and Size Distribution . . . 49
6.3 Light Transport Simulation . . . 51
6.3.1 Extended Boundaries . . . 51
6.3.2 Pore Space . . . 53
6.3.3 Generating a Sand Particle . . . 53
6.3.4 Light Propagation Within a Sand Particle . . . 56
6.4 Extensibility . . . 57

7 Formal Sand Particle Distributions **59**
7.1 Motivation . . . 59
7.2 Prerequisites . . . 60
7.3 Abstract Particle Distributions . . . 62
7.3.1 Definitions . . . 62
7.3.2 Fixed Particle Distributions . . . 64
7.3.3 Discrete Particle Distributions . . . 66

7.3.4 Continuous Particle Distributions 66
7.3.5 Separability 67
7.3.6 Separating Size and Shape 68
7.3.7 Orientation 70
7.3.8 Convex Particles 71
7.4 Concrete Particle Distributions 72
7.4.1 The Particle Distribution used in SPLITS 72
7.4.2 Other Particle Distributions 74
7.5 Computing the Traits of a Particle using Monte Carlo Methods 77
7.5.1 Geometric Cross Section 77
7.5.2 Volume 78

8 Evaluation **79**
8.1 Data Availability 79
8.2 Comparisons with Measured Data 80
8.2.1 Measurement Setup 81
8.2.2 Results of Comparisons 81
8.3 Qualitative Characteristics 83
8.4 Images 86

9 Conclusion **87**
9.1 Strengths and Limitations 87
9.2 Future Work 88

A Generating a Point on a Spheroid **89**
A.1 Prolate Spheroid 91
A.2 Oblate Spheroid 92

B Mixing Minerals **95**
B.1 Density of a Mixture 95
B.2 Converting Between Mass and Volume Fractions 96
B.3 Coated Particles 97

List of Figures

1.1 Images of sand around the world. *Top Left*: Outside Natal, Brazil (courtesy of Gladimir Baranoski). *Top Right*: A sand trap on a golf course (courtesy of Jan Tik). *Bottom Left*: The Ubari sand sea in Libya (courtesy of Miles Hunter). *Bottom Right*: A beach near Kyoto, Japan (courtesy of Chris Gladis). 2

2.1 A photograph of sand showing a close up of sand grains. 6

2.2 The texture triangle depicting the percentages (by mass) of clay, silt and sand-sized particles in the various soil textural classes [129]. 7

2.3 The shaded region indicates the permissible range for the relative proportions (by mass) of the silt, clay, and sand-sized particles in sand [129]. 7

2.4 A demonstration of the effect caused by iron oxide contamination in quartz. The dotted line in both plots represents the spectral reflectance of a pure quartz sample [22]. The dashed line represents the spectral reflectance of a pure iron oxide sample. The solid line represents the spectral reflectance of an artificially prepared mixture consisting of 98% (by mass) quartz and 2% iron oxide. *Left*: The iron oxide is hematite [22]. *Right*: The iron oxide is goethite [22]. The spectral features of hematite (respectively goethite) are clearly visible in the mixed samples. 8

2.5 Projection of a sand grain onto a plane. The circles indicate measurements used in the calculation of the Riley sphericity. 10

4.1 Refraction at the interface between two media. 23

5.1 Complex refractive index of water. *Top Left*: Real part from 0.2 to 200 μm [45], *Top Right*: Imaginary part from 0.2 to 200 μm [45], *Bottom Left*: Real part in the visible region [67], *Bottom Right*: Imaginary part in the visible region [45]. 32

5.2 Refractive index of quartz [113, 139]. The extinction index of quartz is negligible in the visible region [108]. *Left*: Separate ordinary and extraordinary ray refractive indices over entire domain in which Equation (5.1) is valid. *Right*: Ordinary ray refractive index restricted to the visible range. 33

5.3 Complex refractive index of hematite [130]. *Top Left*: Real part, *Top Right*: Imaginary part, *Bottom Left*: Real part restricted to the visible range (weighted average (Section 4.2) of the ordinary and extraordinary rays), *Bottom Right*: Imaginary part restricted to the visible range (weighted average (Section 4.2) of the ordinary and extraordinary rays). 34

5.4 Complex refractive index of limonite (goethite) [32]. Only the ordinary ray refractive index was provided. *Top Left*: Real part, *Top Right*: Imaginary part, *Bottom Left*: Real part restricted to the visible range, *Bottom Right*: Imaginary part restricted to the visible range. 35

5.5 Complex refractive index of magnetite [119]. Only the ordinary ray refractive index was provided. *Top Left*: Real part, *Top Right*: Imaginary part, *Bottom Left*: Real part restricted to the visible range, *Bottom Right*: Imaginary part restricted to the visible range. 36

5.6 Complex refractive index of kaolinite [32]. Only the ordinary ray refractive index was provided. *Top Left*: Real part, *Top Right*: Imaginary part, *Bottom Left*: Real part restricted to the visible range, *Bottom Right*: Imaginary part restricted to the visible range. 37

6.1 Modeled sand medium. 40

6.2 An example of the light propagation through a modeled sand particle. *Left*: The particle consists of a core and an optional coating. The small box around the photon path at the coating interface corresponds to the layer interface diagram to the right. *Right*: A closer look at the modeled interface between the core, coating, and/or the surrounding medium. 42

6.3 Prolate spheroid. 43

6.4 Flowchart outlining the light transport algorithm used by the SPLITS model. The dashed line indicates the main loop. The term *inner* boundary refers to the inside of either extended boundary, whereas the *outer* boundary is the outside of the surface extended boundary. 52

6.5 Generating the next particle for the photon to interact with. *Left*: The distance to the next particle, the sphericity, roundness, particle size, orientation, and the point on the surface of the particle to be intercepted is generated randomly. *Right*: The particle is positioned so that the ray intercepts the particle at the selected point. . . 53

6.6 Tests performed before accepting the generated sand particle. *Left*: A particle that intersects an extended boundary is rejected. *Middle*: A particle that intersects the previous leg of the path is rejected. *Right*: Otherwise, the particle is accepted. . . . 56

7.1 The bold blue line indicates the set of points that are exposed by the particle geometry to the indicated vector. 64
7.2 Rays are cast toward the bounding sphere of a particle to determine its cross sectional area using Monte Carlo [46] techniques. *Left*: The ray hits intersects the particle. *Right*: The ray misses the particle. 77
7.3 Points are selected randomly from within the bounding box of a particle to compute its volume using Monte Carlo [46] techniques. *Left*: The point lies within the particle. *Right*: The point is outside the particle. 78

8.1 Comparisons between real and simulated sand. The solid line indicates the reflectance of the sand sample. The dashed line indicates the modeled reflectance. The parameters used and corresponding RMS errors are provided in Table 8.1. *Top Left*: TEC #10019201, *Top Right*: TEC #10039240, *Bottom Left*: TEC #13j9823, *Bottom Right*: TEC #19au9815. 82
8.2 Images showing variation of sand colour with moisture as predicted by the model. The degree of saturation varies from $\mathcal{S} = 0$ at the top of each image to $\mathcal{S} = 1$ at the bottom. From left to right, the samples are TEC #10019201, TEC #10039240, TEC #13j9823, and TEC #19au9815. 83
8.3 Spectral reflectance curves predicted by the SPLITS model for two of the TEC sand samples, varying the degree of saturation, $\mathcal{S}$. *Left*: TEC #13j9823, *Right*: TEC #19au9815. 83
8.4 Qualitative behaviour of simulated sand. The solid line in each plot indicates the spectral response from the SPLITS model with $\vartheta_{hg} = 0.01$, $r_{hg} = 0.00$, $\vartheta_m = 0.00$, $\zeta_1 = 0.00$, $\zeta_2 = 0.10$, $\zeta_3 = 0.90$, and $\mu'_p = \mu'_m = \mu'_c = 1/3$. *Top Left*: Varying ϑ_{hg}, *Top Right*: Varying r_{hg}, *Bottom Left*: Varying ϑ_m, *Bottom Right*: Varying the texture (ζ_1,ζ_2,ζ_3). 84
8.5 Images showing variation of sand colour as various parameters are changed. The image on the left (base image) corresponds to the solid lines in Figure 8.4. The remaining images correspond to the spectral responses from the SPLITS model with the same parameters as in the base image except, from left to right, $\vartheta_{hg} = 0.05$, $r_{hg} = 0.90$, $\vartheta_m = 0.30$, $\zeta_3 = 1.0$. 84
8.6 BRDF of simulated sand. Profiles along the principal plane are shown on the left (the dashed line indicates the incident direction). Three dimensional plots of the BRDF are shown on the right. *Top*: Normal incidence, *Middle*: For light incident 30° from the normal, *Bottom*: For light incident 60° from the normal. 85
8.7 Images demonstrating potential rendering applications of the SPLITS model to provide the spectral response for sands in various scenes. 86

A.1 The two types of spheroids, *Left*: Prolate, *Right*: Oblate. The bold, blue line denotes the indicatrix (Equation (A.2)). 90

List of Tables

2.1 Soil separates (particle size classes) defined by various agencies [17]. *From Left to Right*: the United States Department of Agriculture (USDA), the International Soil Science Society (ISSS), and the British Standards Institute (BSI). In this thesis, we shall use the system developed by the USDA [129]. 6

5.1 Summary of physical and optical properties of minerals found in sands. All densities and chemical formulae are provided by Mottana *et al.* [90]. 26

5.2 Constants used in Equation (5.1) to compute the ordinary and extraordinary ray refractive indices of quartz [113, 139]. 27

5.3 Geometric mean particle diameter (d_g) and standard deviation (σ_g) for sands with various mixtures of clay, silt and sand-sized particles. The parameters d_g and σ_g are listed for the entire soil and for each of the soil separates individually. The data is provided by Shirazi *et al.* [123]. 29

5.4 Roundness and sphericity statistics for sand-sized grains from sand samples collected from various sites by Vepraskas and Cassel [143]. The average mean and standard deviation across all five sites, and the union of the ranges, are used in the SPLITS model. 30

6.1 A summary of the model parameters, along with typical ranges and values used. . . 41

6.2 Mass fractions, μ_j, of each of the different classes, j, of particles. The quantities β_q and β_{hg} are unknowns, given by Equations (6.7) and (6.6) respectively. 45

6.3 Mass concentration, $\vartheta_{j,\ell}$, of the constituent minerals, ℓ, in each of the different classes j of particles. The quantities ϑ'_k and ϑ''_k are unknowns given by Equations (6.8) and (6.9) respectively. 45

7.1 Formulae used to compute geometric attenuation coefficients for particle distributions with fixed sized, randomly oriented shapes. Derivations for the surface areas of the prolate and oblate ellipsoids are given in Appendix A. All other formulae are provided by Zwillinger [151]. 75

7.2 Formulae used to compute geometric attenuation coefficients for particle distributions with fixed size and orientation. The parameters α', β', and γ' are the incident direction cosines with respect to the particle's local x, y, and z axes (respectively). The parameter $\theta = \cos^{-1}\gamma'$ is the incident angle with respect to the particle's local z axis. The geometrical cross section for a spheroid is provided by Asano [2]. The remaining cross sections are special cases of Equation (7.24). All formulae for volumes provided by Zwillinger [151]. 76

8.1 The parameters used in the SPLITS model for each of the four sand samples, and the root-mean-square error (RMSE) between the actual and simulated reflectances. An RMSE smaller than 0.03 indicates a good spectral reconstruction [64]. 82

List of Symbols

Ψ	Riley sphericity	10
D_i	diameter of an inscribed circle	10
D_c	diameter of a circumscribed circle	10
η	complex refractive index	20
n	real part of the refractive index	20
k	extinction index (imaginary part of the refractive index)	20
κ	absorption index	20
α	absorption coefficient	20
λ	wavelength	20
η_o	ordinary ray complex refractive index	21
η_e	extraordinary ray complex refractive index	21
ε	dielectric constant (square of the complex refractive index)	21
v_i	volume fraction of the inclusions	21
θ_i	incident angle	22
θ_t	transmitted angle	22
n_i	real refractive index of the incident medium	22
n_t	real refractive index of the transmitted medium	22
θ_i	polar angle of incidence	22
θ_t	polar angle of refraction	22
θ_t'	real angle of refraction	22
$\mathbb{R}$	the real numbers	23
r_{TE}	reflection coefficient for the transverse electric mode	24
r_{TM}	reflection coefficient for the transverse magnetic mode	24
R_{TE}	reflectance at a plane surface for the transverse electric mode	24
r_{TM}	reflection coefficient for the transverse magnetic mode	24
R	reflectance at a plane surface for unpolarized light	24
n_w	refractive index of water	26

n_q	refractive index of quartz	27
I	intensity	27
I_0	initial intensity	27
$\mathcal{A}$	absorbance	27
d_g	geometric mean particle diameter	29
σ_g	standard deviation of the geometric mean particle diameter	29
$\mathcal{S}$	degree of saturation	31
η_h	complex refractive index of hematite	41
η_g	complex refractive index of goethite	41
η_m	complex refractive index of magnetite	41
η_k	complex refractive index of kaolinite	41
γ_q	density of quartz	41
γ_h	density of hematite	41
γ_g	density of goethite	41
γ_m	density of magnetite	41
γ_k	density of kaolinite	41
ζ_1	mass fraction of the clay separate	41
ζ_2	mass fraction of the silt separate	41
ζ_3	mass fraction of the sand separate	41
$\mathcal{D}$	depth of the sand medium	42
$\mathcal{P}$	porosity	42
w	volumetric water content	42
a	semiminor axis (prolate spheroid)	43
c	semimajor axis (prolate spheroid)	43
s	particle size	43
h	coating thickness	43
h'	coating thickness relative to the particle size	43
$\mathbf{n}'$	microfacet normal	43
$\mathbf{n}$	normal vector	43
$\mathbf{X}$	normally distributed random variable	44
σ	standard deviation	44
$\mathcal{R}$	particle roundness	44
β_q	unknown mass fraction of pure quartz particles	45
β_{hg}	unknown mass fraction of pure hematite and goethite particles	45
μ_j	mass fraction of particle type j	45
ϑ'_k	unknown mass concentration of kaolinite in hematite coated quartz particles	45

ϑ_k''	unknown mass concentration of kaolinite in goethite coated quartz particles	45
$\vartheta_{j,\ell}$	mass concentration of mineral ℓ within particles of type j	45
ϑ_h	mass concentration of hematite	45
ϑ_g	mass concentration of goethite	45
ϑ_m	mass concentration of magnetite	45
ϑ_{Fe}	mass concentration of iron oxides	45
ϑ_{hg}	mass concentration of hematite and goethite	46
r_{hg}	ratio denoting the relative mass concentrations of hematite and goethite	46
μ_p'	mass fraction of pure particles	46
μ_m'	mass fraction of mixed particles	46
μ_c'	mass fraction of coated particles	46
ν_{coat}	volume fraction of coating for a coated particle	47
A_S	surface area	47
V	volume	47
A_V	surface area to volume ratio	48
γ_j	density of a particle of type j	48
γ_ℓ	density of the mineral ℓ	48
γ	particle density	48
$\nu_{j,\ell}$	volume concentration of the mineral ℓ within particles of type j	49
ν_j	volume fraction of particles of type j	49
$\mathfrak{f}_g$	log-normal particle size distribution defined by Shirazi *et al.* [123]	49
a_g	base 10 logarithm of the geometric mean particle diameter	49
b_g	base 10 logarithm of the standard deviation of the geometric mean particle diameter	49
$\mathfrak{F}_m$	mass fraction of particles within a given size range	50
Φ	normal cumulative density function	50
K	geometric attenuation coefficient	54
d_j	path length to the nearest particle of type j	54
ξ	canonical random variable	54
Φ'	normal probability density function	54
f_X	probability density function for the random variable X	54
d	path length	55
$\mathbf{r}$	reflected vector	57
$\mathbf{t}$	transmitted vector	57
T	transmittance	57
F_X	cumulative density function for the random variable X	60

Pr	probability	61
$\mathbf{x}$	a particle geometry	62
$(\mathsf{X},\mathfrak{N})$	a particle distribution	63
X	a set of particle geometries	63
$\mathfrak{N}$	number of particles per unit volume	63
2^{X}	the set of subsets of X	63
$f:\mathsf{A}\to\mathsf{B}$	f is a function mapping A to B (*i.e.*, $b=f(a)$, were $a\in\mathsf{A}$ and $b\in\mathsf{B}$)	63
$\varnothing$	the empty set	63
$\mathfrak{n}$	derivative of the number of particles per unit volume	63
$r(t)$	a ray $\mathbf{p}+t\mathbf{v}$	64
$\mathsf{E}_{\mathbf{x},\mathbf{v}}$	set of points exposed (Definition 7.3.4) by the geometry $\mathbf{x}$ to the vector $\mathbf{v}$	64
C_t	region in which a particle centered within would intersect the ray r at $r(t)$	64
$\mathsf{C}_{(0,t_0)}$	region in which a particle centered within would intersect the ray r between $r(0)$ and $r(t_0)$	65
M	subset of an infinite medium	65
$\lvert\mathsf{X}\rvert$	cardinality (size) of the set X	66
$\mathfrak{N}_j$	number of particles per unit volume with geometry $\mathbf{x}_j$	66
$\mathsf{A}\times\mathsf{B}$	Cartesian product of the sets A and B (*i.e.*, the set of pairs (a,b) with $a\in\mathsf{A}$ and $b\in\mathsf{B}$)	67
$\mathbb{R}^+$	the positive real numbers	68
$\mathfrak{F}_{\mathfrak{v}}$	fraction of volume occupied by particles within a given size range	69
$\mathfrak{f}_{\mathfrak{v}}$	derivative of $\mathfrak{F}_{\mathfrak{v}}$	69
ν	total fraction of volume occupied by particles	69
$\mathfrak{f}_{\mathfrak{n}}$	number density function	69
ω	direction vector in three dimensional space	70
$\mathfrak{S}$	the unit sphere	70
$\overline{G}$	mean geometric cross sectional area (taken over all directions $\omega\in\mathfrak{S}$)	70
$\mathfrak{C}$	the unit circle	70
M	mass	95

Chapter 1

Introduction

Sand is found in a variety of outdoor scenes such as beaches, deserts, golf courses, and even in a child's sandbox. In computer graphics, however, little attention has been paid to the predictive rendering of sand. Usually, a diffuse reflection model is assumed and texture mapping [51] or bump mapping [14] is used to apply spatial variation [102]. The colour is then painstakingly tweaked by an artist to yield a believable result. There is clearly room for improvement in the rendering of this widespread (Figure 1.1), yet under appreciated, material.

In this thesis, we present a *sp*ectral *li*ght *t*ransport model for *s*and, hereafter referred to as SPLITS. Although much has been published in the computer graphics and remote sensing literatures on the topic of sand, these previous research efforts have emphasized the mechanical aspects of sand [88, 103] or the simulation of particular effects, such as wetness [65] or surface roughness [21]. A more thorough synopsis of related work is given in Chapter 3. SPLITS represents, to the best of our knowledge, the first attempt to simulate the spectral reflection properties of sand using its physical and mineralogical properties, henceforth referred to as *characterization data*, as input.

There are several reasons for modeling sand in terms of its characterization data rather than in terms of arbitrary parameters not directly relating to sand. For computer graphics, it is important that the parameters make intuitive sense, and that one can predict the consequences of modifying

Figure 1.1: Images of sand around the world. *Top Left*: Outside Natal, Brazil (courtesy of Gladimir Baranoski). *Top Right*: A sand trap on a golf course (courtesy of Jan Tik).* *Bottom Left*: The Ubari sand sea in Libya (courtesy of Miles Hunter).† *Bottom Right*: A beach near Kyoto, Japan (courtesy of Chris Gladis).‡

a particular parameter [1, 8]. The animator's task of selecting an appropriate colour and reflection properties may then be automated to a large extent, by eliminating much of the trial and error involved. Hyperspectral remote sensing with satellite or aircraft based equipment is used to investigate properties of land surfaces without having to physically survey the area [64, 126]. For other worlds, such as Mars, a field survey may not be possible. In this case, spectral signatures may be the only clue available for determining surface characteristics [89, 127]. For these scientific applications, this relationship between model parameters and the physical properties is necessary so that sand characterization data may be obtained by inverting the model. Finally, for the model to be

evaluated objectively, the parameters must relate to the material that one is trying to simulate.

The main results of this thesis are

- The SPLITS model is, to the best of our knowledge, the first comprehensive spectral light transport model for sand, using an extensive set of sand characterization data as input and yielding both the spectral and the spatial responses (the *measurement of appearance*). The model compares well with measured data and with phenomena observed in the literature.
- Usually, the simulation of light transport in natural materials is performed under the assumption that such materials may be represented using layers and that the directional changes of travelling photons can be modeled using precomputed phase functions[§] [47, 63, 71, 110, 133]. In this thesis, we suggest an alternative approach in which these directional changes are computed on the fly, but without explicitly storing the material constituents. This approach strikes a balance between the use of precomputed phase functions, which do not relate to any particular material, and a conventional ray tracing approach, which, among other difficulties, requires much storage space. Although in the context of this thesis the focus is on sand, this approach can potentially be applied to other materials such as plant or human tissues.
- A recurring theme throughout this thesis is the difficulty in obtaining adequate data. These difficulties are seen in two contexts, both in terms of spectral data for the mineral constituents used in the SPLITS model (Chapter 5) and in terms of the measurement data used to evaluate the model (Chapter 8). Despite the efforts of numerous researchers, much work still needs to be done to obtain spectral and scattering measurements for natural materials along with the data characterizing those particular samples, so that they may be used to evaluate proposed models in an accurate and objective fashion.

[*] Cropped from "Discouragement" by Jan Tik (`http://www.flickr.com/photos/jantik/6055252/`), licensed under Creative Commons (Attribution 2.0, `http://creativecommons.org/licenses/by/2.0/`).

[†] "Ubari sand sea" by Miles Hunter (`http://www.flickr.com/photos/milesh/72387927/`), licensed under Creative Commons (Attribution-NonCommercial 2.0, `http://creativecommons.org/licenses/by-nc/2.0/`).

[‡] "The Beach 02" by Chris Gladis (`http://www.flickr.com/photos/mshades/39696839/`), licensed under Creative Commons (Attribution 2.0, `http://creativecommons.org/licenses/by/2.0/`).

[§] A phase function describes the angular distribution of scattered light relative to the incident direction after a single scattering event or after multiple scattering events [142].

The remainder of this thesis is organized as follows. Background information about sand is given in the next chapter. In Chapter 3, previous work relating to sand in the computer graphics and remote sensing literatures is outlined. Relevant optics issues are discussed in Chapter 4. The data required to implement the model is provided in Chapter 5. A general description of the model is provided in Chapter 6, and key mathematical concepts used in its algorithmic formulation are derived in Chapter 7. The evaluation approach and the results are discussed in Chapter 8. We conclude and outline directions for future work in Chapter 9.

Chapter 2

Properties of Sand

In this chapter, the relevant background information on sand is provided. We begin by defining precisely what sand is. The pertinent factors affecting light transport with sand are then described. The following, however, is not a complete treatise on sand. Interested readers are referred to works by Pettijohn *et al.* [107], Brady [17], or Gerrard [41].

2.1 What is Sand?

Sand is a particular type of *soil*. Soil is composed of particles of weathered rock and sometimes organic matter immersed in a medium of air and water (the *pore space*) [41]. Figure 2.1 shows a close up view of sand grains.

Soils are classified according to the size distribution of the mineral particles [17]. This is accomplished first by assigning individual particles to classes, called *soil separates*, according to their size. The relative masses of each of the soil separates are then compared to determine the *texture* of a soil sample, not to be confused with texture mapping [51].

Various agencies have differing definitions for soil separates and textural classes [17]. In this work, we use the system developed by the United States Department of Agriculture (USDA) [129]. The USDA defines three soil separates, called *sand*, *silt*, and *clay*, as delineated in Table 2.1.

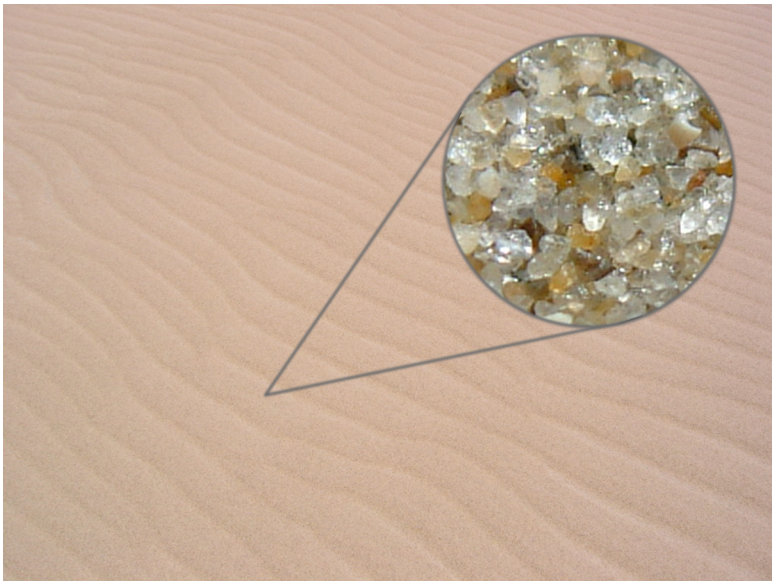

Figure 2.1: A photograph of sand showing a close up of sand grains.

	USDA		ISSS		BSI	
Separate	**Min.**	**Max.**	**Min.**	**Max.**	**Min.**	**Max.**
sand	0.05	2.0	0.02	2.0	0.06	2.0
silt	0.002	0.05	0.002	0.02	0.002	0.06
clay	-	0.002	-	0.002	-	0.002

Table 2.1: Soil separates (particle size classes) defined by various agencies [17]. *From Left to Right*: the United States Department of Agriculture (USDA), the International Soil Science Society (ISSS), and the British Standards Institute (BSI). In this thesis, we shall use the system developed by the USDA [129].

Particles larger than 2 mm are classified as rock fragments and are not considered to be part of the soil. Figure 2.2 graphically depicts the textural classes defined by the USDA [129]. A sand textured soil contains at least 85% sand-sized particles. Figure 2.3 shows the range for the relative proportions of clay, silt and sand-sized particles in sand.

That the term *sand* is used to describe both a soil *separate* and a soil *texture* may be a source of confusion. In the remainder of this thesis, the term *sand* is used to refer to a soil texture unless otherwise stated (for instance, by referring to *sand-sized* particles).

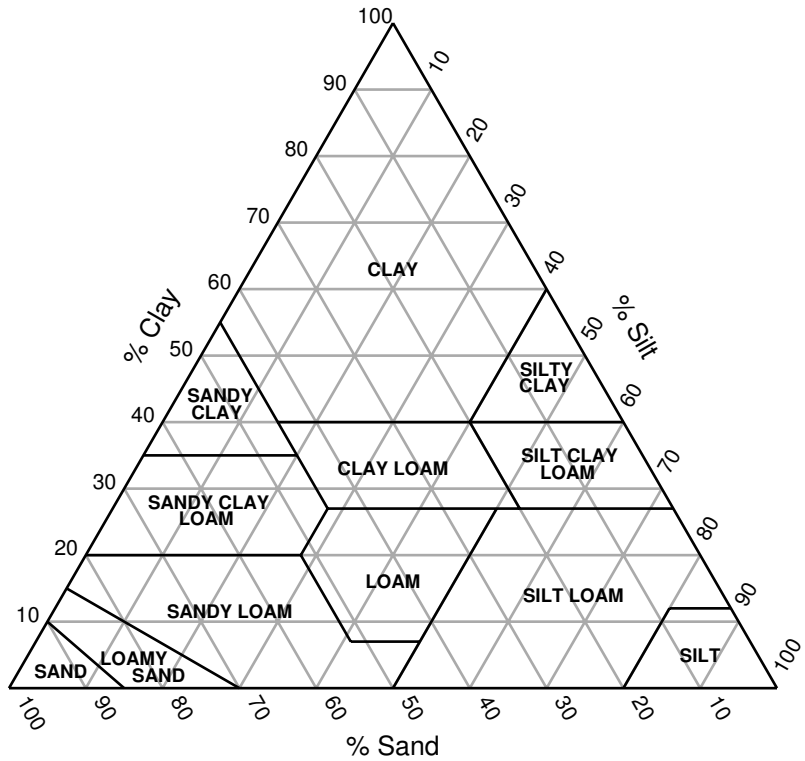

Figure 2.2: The texture triangle depicting the percentages (by mass) of clay, silt and sand-sized particles in the various soil textural classes [129].

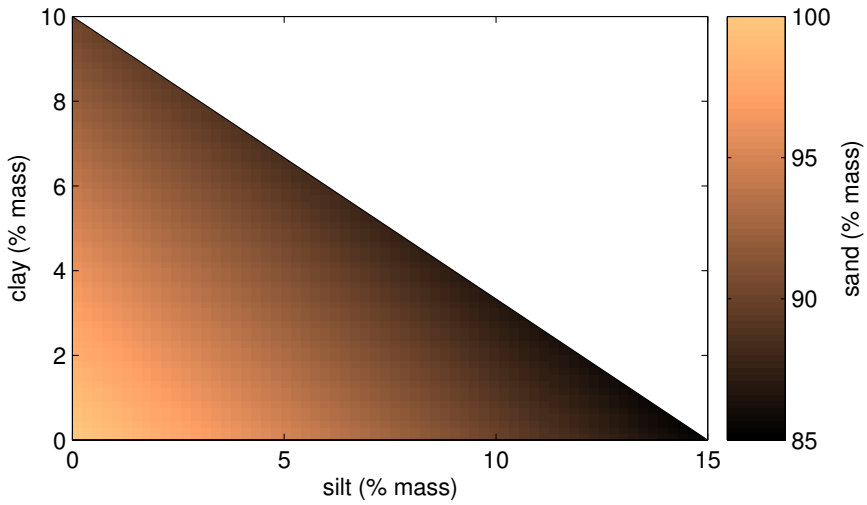

Figure 2.3: The shaded region indicates the permissible range for the relative proportions (by mass) of the silt, clay, and sand-sized particles in sand [129].

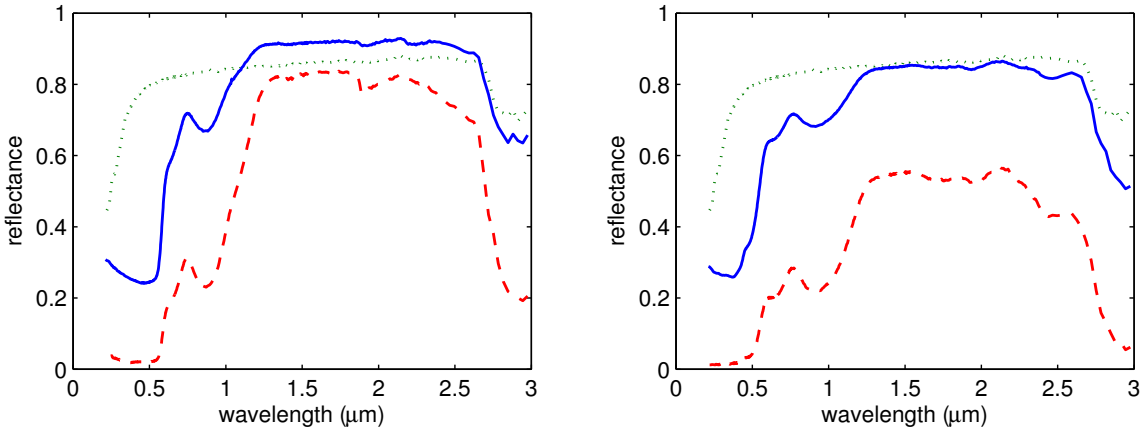

Figure 2.4: A demonstration of the effect caused by iron oxide contamination in quartz. The dotted line in both plots represents the spectral reflectance of a pure quartz sample [22]. The dashed line represents the spectral reflectance of a pure iron oxide sample. The solid line represents the spectral reflectance of an artificially prepared mixture consisting of 98% (by mass) quartz and 2% iron oxide. *Left*: The iron oxide is hematite [22]. *Right*: The iron oxide is goethite [22]. The spectral features of hematite (respectively goethite) are clearly visible in the mixed samples.

2.2 Factors Affecting Light Transport

The reflectance of sand generally increases with wavelength [26]. Additionally, sand reflection is non-Lambertian [98, 25]. In particular, sand exhibits *retro-reflection* [25], which is reflection in the direction toward the source of illumination. Sand also reflects light in the forward direction, peaking at an larger angle to the normal than that of the direction of specular reflection [25].

The most important factors contributing to the reflectance of soils in the visible range are its mineral composition (and iron oxides in particular), moisture, and particle size and shape [11].

2.2.1 Mineral Composition

As sand is composed primarily of weathered rock [107], the optical properties of that rock may influence light transport within sand. The *parent material* is the rock that is the source of the mineral part of the sand. This is typically a silicate mineral [17] such as quartz, gypsum or calcite, with quartz being the most common [17, 77]. While these minerals are colourless in pure form, trace amounts of contaminants may substantially affect their colour [55], as demonstrated in Figure 2.4.

Iron oxide gives sand its distinctive hues. Indeed, the two most significant minerals that determine soil colour, hematite and goethite [36], are iron oxides. Goethite, also known as *yellow ochre* [36] or *limonite* [90], is one of the most common minerals found in soils [36]. It colours soils yellow to brown [138]. Hematite, or *red ochre* [36], imparts a red colour to soils and may mask the colour of goethite except when in small quantities [138]. Hematite is usually found in tropical regions and is rare in temperate or cool climates [24]. Iron oxides may be present as contaminants in the parent material [90]. They are also found, typically within a kaolinite or illite matrix, as coatings, approximately 1–5 μm thick, that form on the grains during aeolian* transport [149].

Additionally, magnetite and ilmenite are often found in beach and river sands [56]. These minerals are spectrally very similar. They are opaque and are black in colour [56].

2.2.2 Water

The presence of water darkens sand. The principal reason for this is that the reduced contrast between the refractive index of the pore space and that of the mineral particles (typically quartz) induces stronger forward scattering at particle interfaces [140, 76]. In addition, water will tend to adhere to solid particles in the soil due to a phenomenon called hydrogen bonding [17]. Internal reflections at the air-water interface may trap light within this film of water [11].

2.2.3 Grain Size and Shape

Grain size affects reflectance by influencing the number of scattering interfaces per unit distance through the medium [145]. Smaller particles, and thus a higher density of scattering interfaces, result in higher reflectances [11, 77].

Grain shape may also affect scattering properties [11]. The shape of the grain is described by two quantities: *sphericity* and *roundness*. Sphericity refers to the general shape of a particle by expressing its similarity to that of a sphere [146]. In this thesis, we use the sphericity measure proposed by Riley [114], which is a *projection* sphericity measure, meaning its definition is based

*Aeolian means "by wind."

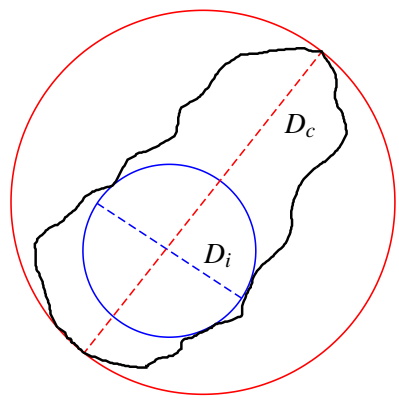

Figure 2.5: Projection of a sand grain onto a plane. The circles indicate measurements used in the calculation of the Riley sphericity.

on the projection of the particle onto a plane. The *Riley sphericity*, Ψ, of a particle is given by

$$\Psi = \sqrt{\frac{D_i}{D_c}}, \tag{2.1}$$

where D_i is the diameter of the largest inscribed circle and D_c is the diameter of the smallest circumscribed circle, as shown in Figure 2.5.

In contrast, *roundness* can loosely be described as a measure of detail in the features on the grain surface [146]. A higher roundness value indicates a smoother surface. Roundness is determined by comparing the particle to images on a roundness chart [74].

2.2.4 Additional Factors

There are several other factors that may effect the reflectance of soils. The following factors, however, either show themselves primarily outside the visible region of the spectrum, are less applicable to sands than to finer soils, or affect reflectance indirectly.

Organic matter, or *humus*, consists of decomposed plant and animal remains [17]. It is a black substance that tends to darken soils [11]. In addition, concentrations of organic matter higher than approximately 2% mask the effects of iron oxide [11, 40]. Sandy soils, however, typically have lower concentrations of organic matter than other types of soils [17, 38].

The total negative charge density at the surface, known as the *cation exchange capacity* (CEC) [41], is highly correlated with reflectance in the infrared region [11]. However, its effects are likely indirect, since the CEC also correlates well with other factors that are known to influence soil reflectance characteristics, such as organic matter content [11].

Surface roughness plays an important role in effecting the reflectance of soils [84]. Individual soil particles may aggregate into clods, forming a rough surface [17]. This is not so important for sand, however, as sandy soils are less cohesive than finer soils [107].

Human activity indirectly affects soil reflectance. Matthias *et al.* [84] demonstrated that different tillage instruments have varying effects on soil reflectance. Tillage breaks up aggregates, which affects surface roughness. It also facilitates incorporation of organic matter. Transportation, by vehicle or on foot, compacts soil. This smooths the soil surface and also makes it impenetrable to water or plant roots [17]. The resulting decrease in water and organic matter content, as well as surface roughness, will increase reflectance.

Chapter 3

Related Work

Research into sands and soils in the computer graphics and remote sensing literatures is extensive. These efforts fall into two broad categories. Geometric modeling aspects, such as landscape generation and displacement, have received much attention from the computer graphics community. In contrast, appearance models for sand have been relatively scarce in the computer graphics literature. We will, in this chapter, also discuss some general purpose reflection models that may be applied to sand and models related to sand. Premŏze [111] provides a survey of additional light transport methods. Finally, we shall discuss several models that deal with specific effects applicable to sand, such as moisture.

3.1 Geometric Models

The following are methods for representing the shape and movement of sand. The model for representing the geometry of a sand surface is independent from the model proposed in this thesis, and this summary is included for completeness.

The geometric models may be further subdivided into two families: landscape development methods and models for simulating the displacement caused by the impact of another object.

3.1.1 Landscape Formation

Numerous models exist for simulating the formation of sand dunes and dune fields. These techniques generally model the dune field as a height map and simulate aeolian transport by reducing the height at one cell and increasing the height at another cell downwind correspondingly. This process is repeated many times. Examples of such models include those proposed by Momiji [88] and by Nishimori and Ouchi [96]. A more extensive summary of dune field simulation methods is provided by Momiji [88]. Onoue and Nishita [102] and Nishita and Dobashi [97] used the model proposed by Nishimori and Ouchi [96] to generate a bump map which was then used to create appealing images of a dune field.

Additionally, Roudier *et al.* [117] has developed a model simulating erosional and depositional processes to create realistic landforms. Fearing [37] proposed a model to simulate the accumulation of snow. Although not specifically designed for sand, it may be adapted for this purpose [37].

3.1.2 Sand Displacement

The displacement of sand or soil resulting from contact with a solid object has been modeled extensively in the computer graphics literature. Li and Moshell [78] provide a model to represent soil slippage and displacement caused by various excavation activities (*e.g.*, digging, piling, dumping). Chanclou *et al.* [19] present a particle-based method to model the effects of moving objects travelling across a soil surface. Sumner *et al.* [136, 137] simulate the displacement of sand, mud, and snow caused by the impact of a rigid body. A height map is used to represent the initial surface. The sand from cells struck by the object are then compressed and displaced toward neighbouring cells. Onoue and Nishita [103, 104] allow for displacement caused by a concave object by storing a series of *height spans* at each cell instead of a representing the surface as a simple height map. The objects that impact the sand are also modeled using these height spans. Zhu and Bridson [150] animate sand by treating it as a fluid. Bell *et al.* [13] represent granular materials as a system of individual particles. The forces acting on each grain are then simulated to model the impact of another object.

3.2 Reflection Models

The following are models which simulate characteristics relating to the appearance of sand. We describe first some general purpose models that may be adapted to sand. We then outline the various models available for simulating particular effects.

3.2.1 General Models

Some general models available in the computer graphics literature may be applied to sand. Oren and Nayar [105] generalized the widely used Lambertian model [148] by representing a surface using a collection of symmetrical V-shaped cavities. The authors compare the output from their model to a sand sample. This model, however, only simulates reflectance in the spatial domain. Spectral reflectance data is required as input to the model. Hanrahan and Krueger [47] proposed a scattering model consisting of layers of various materials. Reflection, transmission, subsurface scattering and absorption are simulated within each layer using Monte Carlo techniques [46]. Scattering events are simulated with the Henyey-Greenstein phase function [52], the widespread use of which has recently been called into question [6, 7, 8, 80]. The Henyey-Greenstein phase function is an empirical function with a single parameter which bears no relation to the sand characterization data [80].

There have also been models for particulate media presented in the optics and geophysics literatures. Hapke [48] proposed an analytic radiative transfer model for particulate surfaces, which was then used to simulate reflectances from planetary surfaces [50]. Emslie and Aronson [35] modeled particulate surfaces, treating large particles separately from those smaller than the wavelength of light. Large particles were modeled using spheres of the same volume as actual particles and absorption was simulated at small scale *asperities* on the surface of the particle. However, their model was only applicable to the far infrared [31]. Egan and Hilgeman [31] subsequently rectified this by simulating scattering, in addition to absorption, at these asperities.

The preceding models are intended to simulate a wide variety of materials. As such, their parameters do not specifically relate to sand. This list, however, is by no means a complete list of

widely applicable reflection models. The interested reader is referred to the work of Premŏze [111] for a broader survey, including more detailed descriptions of some of the models listed here.

3.2.2 Related Models

Soulié *et al.* [131] used Voronoï diagrams [3] to model a compact granular material, such as granite. Subsurface scattering within the medium is accomplished using the Henyey-Greenstein phase function [52]. Their model is not directly applicable to sand because sand is a loose granular material [107]. The model proposed by Soulié *et al.* does not account for pore space.

3.2.3 Simulation of Specific Effects

The following models simulate various effects described in Section 2.2.

Moisture

Various methods exist to achieve the darkening effect caused by water. A simple technique would be to apply a wetness map to scale the reflectance of the material, as done by Kass and Miller [66]. Jensen *et al.* [65] use an extension of the Henyey-Greenstein phase function previously used by, among others, Irvine [60] and Uesugi *et al.* [141]. Jensen *et al.* adjust the degree of forward scattering to achieve varying levels of wetness. A layer of water over the surface is also modeled. Lobell and Asner [81] use an exponential function to empirically model reflectance in terms of moisture content. Neema *et al.* [93] analytically model the sand medium using layers of reflective spheres coated by a thin film of water, the thickness of which is a function of moisture content.

Iron Oxides

Barron and Montealegre [10] apply Kubelka-Munk theory [75] to model the influence of iron oxides on soil colour. Torrent *et al.* [138] relate hematite and goethite concentrations to a function of the Munsell colour [94] of the soil, which Torrent *et al.* call the *redness rating*. Okin and Painter [100]

use spherical, hematite coated quartz particles to study the effect of grain size on the reflectance of desert sands.

Roughness

There are several models in the remote sensing literature for simulating the scattering of light at rough soil surfaces. Many of these models follow the work of Egbert [33], simulating shadowing and masking effects using occluders distributed over a plane. Cierniewski [20] proposed a mathematical model to derive the reflectance of an arbitrary rough soil surface relative to the reflectance of a smooth surface consisting of the same soil. The rough surface is modeled using spheres distributed uniformly across a tilted plane. This model has subsequently been improved by, among other changes, using spheroids instead of spheres and accounting for specular reflection. These improvements are summarized by Cierniewski and Karnieli [21]. Norman *et al.* [98] represent the soil surface as regularly spaced boxes over a plane.

Other models for rough soil surfaces include that proposed by Irons and Smith [59]. They used the Minnaert [87] function to investigate the effect of surface roughness on reflectance. Walthall *et al.* [147] model the bidirectional reflectance of soil surfaces as a simple empirical function of roughness. Despan *et al.* [30] analytically model rough soil surfaces using a Gaussian function for the surface height. Cooper and Smith [23] used ray tracing methods to simulate a soil surface whose height is described by periodic function over the XY-plane.

Li *et al.* [79] examine roughness on a smaller scale by modeling soil particles as two randomly oriented plane boundaries. Reflection and transmission through the particle is computed analytically, accounting for polarization.* A doubling algorithm [32] is then applied to extend the individual particle model to represent a half space of soil. Li *et al.* [80] have subsequently expanded this model to include one level of multiple reflection by allowing multiple planes for the upper boundary of the particle.

*Polarization arises from the difference in phase between the electric and magnetic wave components of light [16].

Organic Matter

Ingleby and Crow [58] propose a method for determining the organic matter content of soils from soil reflectance. Islam *et al.* [62] use principal component analysis to determine various soil parameters, including organic matter content, from reflectance.

Chapter 4

Optics

In the following, relevant issues from optics are discussed. First, we shall address the inconsistency with which various optical terms are used and clarify the optical terminology as used in this thesis. Next, we will review some results from optics that are required to implement the SPLITS model. The reader may wish to refer back to this chapter from time to time while progressing through the remainder of this thesis.

4.1 Conventions and Nomenclature

Due to the variation in the use of terminology present in the optics and computer graphics literatures, it is important to clarify the meaning of the terminology used in this thesis. We shall use terminology drawn from the works of Nicodemus *et al.* [95], Muller [91], and Bohren and Huffman [15].

4.1.1 Complex Refractive Index

The nomenclature associated with the complex refractive indices of media is inconsistent throughout the optics literature. Muller [91] provides an excellent account of the different conventions and nomenclature used in optics.

There are four definitions used for the complex refractive index:

$$\eta = n(1 \pm i\kappa) = n \pm ik. \tag{4.1}$$

Some authors may use k in place of κ, or *vice versa*, in the above. Whether one uses plus or minus depends on the convention used when defining the time dependent factor, $\exp(\mp i\omega t)$, of the electromagnetic wave [91]. The two forms $n(1+i\kappa)$ and $n+ik$ are equivalent, as are $n(1-i\kappa)$ and $n-ik$, and are related by

$$k = n\kappa. \tag{4.2}$$

The real part, n, of the complex refractive index has been consistently referred to in the literature as the *refractive index* or the *real part* of the refractive index [91]. However, many terms are used to describe k and κ, such as *extinction coefficient* or *index*, *absorption coefficient* or *index*, and *attenuation coefficient* or *index*. To make matters worse, almost every term that has been used for k has been used for κ, and *vice versa* [91]. The term absorption coefficient is particularly misleading since the factor describing the absorption of light within a medium,

$$\alpha = \frac{4\pi k}{\lambda}, \tag{4.3}$$

has this name. The terms *extinction coefficient* and *attenuation coefficient* also have other meanings [15, 61].

In this thesis, we shall use the preferred terminology proposed by Muller [91]:

η = (complex) refractive index,

n = (real part of the) refractive index,

k = extinction index *or* imaginary part of the refractive index,

κ = absorption index,

α = absorption coefficient.

We shall use the forms of the complex refractive index with a positive imaginary part, preferring

the form $n + ik$ over $n(1 + i\kappa)$. However, the latter may be used when referring to works by other authors using that form, as in Section 4.4.

4.2 Birefringence

Birefringence, also known as *double refraction*, occurs when light entering a material splits into two beams, called the *ordinary* and *extraordinary* rays (*o-ray* and *e-ray* for short), that travel at different speeds [90]. There are, therefore, two indices of refraction, η_o and η_e. This effect is particularly evident in calcite, for example [90]. For simplicity, however, we may ignore the extraordinary ray for materials with low birefringence. We may also combine the two indices of refraction using a weighted mean, given by

$$\eta = \frac{2\eta_o + \eta_e}{3}, \tag{4.4}$$

as has been done by Kerker *et al.* [68].

4.3 Mixed Materials

There are several methods for computing the complex refractive index of a mixture of two or more materials. These methods involve computing the dielectric constant* of the mixture, ε_{avg}, as a function of the dielectric constants and volume fractions of each of the constituents. A result from Maxwell Garnett theory [15] gives ε_{avg} for a mixture consisting of inclusions, with dielectric constant ε_i, dispersed within a matrix having dielectric constant ε_m. If the volume fraction of the inclusions is v_i, then

$$\varepsilon_{avg} = \varepsilon_m \left(1 + \frac{3v_i \left(\frac{\varepsilon_i - \varepsilon_m}{\varepsilon_i + 2\varepsilon_m} \right)}{1 - v_i \left(\frac{\varepsilon_i - \varepsilon_m}{\varepsilon_i + 2\varepsilon_m} \right)} \right). \tag{4.5}$$

*The dielectric constant is the square of the complex refractive index [106].

This method has been used previously by Okin and Painter [100], and will be used in the SPLITS model (Section 6.2.4). Equation (4.5) may be approximated using the Bruggeman equation [15],

$$v_i \frac{\varepsilon_i - \varepsilon_{avg}}{\varepsilon_i + 2\varepsilon_{avg}} + (1 - v_i) \frac{\varepsilon_m - \varepsilon_{avg}}{\varepsilon_m + 2\varepsilon_{avg}} = 0, \tag{4.6}$$

as has been done by Sokolik and Toon [130]. Due to the symmetry of the above equation (*i.e.*, the matrix and the inclusions are interchangable), one can simulate mixtures of more than two minerals simply by adding additional terms [130], yielding the affine combination

$$\sum_j v_j \frac{\varepsilon_j - \varepsilon_{avg}}{\varepsilon_j + 2\varepsilon_{avg}} = 0, \tag{4.7}$$

with $\sum_j v_j = 1$. One must, of course, first solve for ε_{avg}. A simple volumetric mean may also be used to approximate ε_{avg}, as has also been done by Sokolik and Toon [130].

4.4 Generalization of Snell's Law for an Absorbing Medium

Refraction at an interface between two dielectric media is given by Snell's Law [16, 106]:

$$n_t \sin\theta_t = n_i \sin\theta_i, \tag{4.8}$$

where n_i and n_t are the refractive indices of the two media, θ_i is the angle of incidence, and θ_t is the angle of refraction, as depicted in Figure 4.1. However, if one or both of the media are absorbing, then the corresponding refractive index, $\eta = n(1 + i\kappa)$, is complex, as is θ_t. Thus, θ_t no longer has its intuitive interpretation as an angle of refraction [16].

To obtain the direction of propagation, that is, a *real* angle of refraction, θ_t', one must work from the wave equations describing the propagation of light in an absorbing medium. This yields [16]

$$\cos\theta_t' = \frac{nq(\cos\psi - \kappa\sin\psi)}{\sin^2\theta_i + n^2q^2(\cos\psi - \kappa\sin\psi)^2}, \tag{4.9}$$

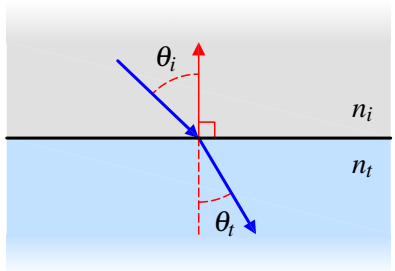

Figure 4.1: Refraction at the interface between two media.

$$\sin\theta_t' = \frac{\sin\theta_i}{\sqrt{\sin^2\theta_i + n^2 q^2 (\cos\psi - \kappa\sin\psi)^2}}, \tag{4.10}$$

where $\eta = n(1+i\kappa)$ is the relative complex refractive index and

$$q = \left(\left(1 - \frac{1-\kappa^2}{n^2(1+\kappa^2)^2}\sin^2\theta_i\right)^2 + \left(\frac{2\kappa}{n^2(1+\kappa^2)^2}\sin^2\theta_i\right)^2\right)^{\frac{1}{4}},$$
$$\psi = \frac{1}{2}\tan^{-1}\left(\frac{2\kappa\sin^2\theta_i}{n^2(1+\kappa^2)^2 - (1-\kappa^2)\sin^2\theta_i}\right).$$

Note that Equation (4.10) can be rewritten as $n'\sin\theta_t' = \sin\theta_i$, with $n' \in \mathbb{R}$, and thus has the form of Snell's Law. However, n' now depends on the incident angle in addition to the properties of the media [16].

4.5 Reflectance at a Plane Surface

The reflectance at a plane interface between two media with complex refractive indices η_1 and η_2 is described by the Fresnel equations [106]. Defining the relative refractive index $\eta = \eta_2/\eta_1$, the *reflection coefficients* are given by

$$r_{TE} = \frac{\cos\theta_i - \sqrt{\eta^2 - \sin^2\theta_i}}{\cos\theta_i + \sqrt{\eta^2 - \sin^2\theta_i}},$$
$$r_{TM} = \frac{\eta^2\cos\theta_i - \sqrt{\eta^2 - \sin^2\theta_i}}{\eta^2\cos\theta_i + \sqrt{\eta^2 - \sin^2\theta_i}},$$

for the *transverse electric* (TE) and *transverse magnetic* (TM) modes, respectively [106]. The reflectances for the TE and TM modes are then given, respectively, by $R_{TE} = |r_{TE}|^2$ and $R_{TM} = |r_{TM}|^2$ [106]. For natural (unpolarized) light, the reflectance is the average of the reflectances for the two modes [16],

$$R = \frac{R_{TE} + R_{TM}}{2}. \tag{4.11}$$

Chapter 5

Data

In this chapter, the data required to implement the SPLITS model is provided, along with details on how the data was arrived at in cases where we have used data which was derived from raw data provided. We also discuss various issues concerning the acquisition of the data.

5.1 Mineral Properties

The following outlines the properties of the various mineral constituents in sands.

5.1.1 Occurrence of Iron Oxides

As previously mentioned (Section 2.2.1), iron oxides are the most important factor influencing the colour of sands. Iron oxide concentration within soils varies from less than 0.1% to several multiples of 10% [24]. Hematite and goethite are the most common iron oxides in soils, with goethite being the most common and hematite being the second most common [24]. Goethite dominates in cooler, temperate regions where hematite occurrence is negligible [24]. In warmer climates, goethite and hematite occur together. The ratio

$$\frac{\text{mass (hematite)}}{\text{mass (hematite)} + \text{mass (goethite)}},$$

Material	Chemical Formula	Density ($\mathrm{kg\,m^{-3}}$)	Refractive Index
Water	H_2O	1.0×10^3	Figure 5.1
Quartz	α-SiO_2	2.65×10^3	Figure 5.2
Hematite	Fe_2O_3	5.2–5.3×10^3	Figure 5.3
Goethite	α-$FeO(OH)$	4.3×10^3	Figure 5.4
Magnetite	Fe_3O_4	5.2×10^3	Figure 5.5
Kaolinite	$Al_2Si_2O_5(OH)_4$	2.58–2.60×10^3	Figure 5.6

Table 5.1: Summary of physical and optical properties of minerals found in sands. All densities and chemical formulae are provided by Mottana *et al.* [90].

describing the relative proportions (by mass) of hematite and goethite, may vary anywhere from zero to about 0.90-0.95 [24].

5.1.2 Refractive Indices

Plots for the complex refractive index of the minerals used in SPLITS are provided at the end of this chapter in Figures 5.1 through 5.6, outlined in Table 5.1 and beginning on page 32. The complex refractive indices of goethite, kaolinite, and illite, are provided in tabular form by Egan and Hilgeman [32]. The ordinary ray and extraordinary ray complex indices of refraction for hematite were acquired from plots provided by Sokolik and Toon [130]. This data was averaged to yield a combined refractive index as described in Section 4.2. The data for magnetite was extracted from plots are provided by Schlegel *et al.* [119]. A table of complex refractive index data for water is provided by Hale and Querry [45] covering the range from 0.2 to 200 μm. For the visible region, the real part of the refractive index of water may be approximated by the expression

$$n_w(\lambda) = 1.324 + \frac{3.046 \times 10^3}{\lambda^2},$$

where λ is the wavelength in nanometers, which was derived by Kerker [67] to fit measured data. The refractive index of quartz between 0.18 and 0.71 μm is given by

$$n_q(\lambda) = \sqrt{1 + \sum_k \frac{\beta_k \lambda^2}{\lambda^2 - \lambda_k^2}}, \tag{5.1}$$

	Ordinary Ray		Extraordinary Ray	
k	β_k	λ_k (μm)	β_k	λ_k (μm)
1	0.663044	6.00×10^{-2}	0.665721	6.00×10^{-2}
2	0.517852	1.060×10^{-1}	0.503511	1.060×10^{-1}
3	0.175912	1.190×10^{-1}	0.214792	1.190×10^{-1}
4	0.565380	8.844×10^{0}	0.539173	8.792×10^{0}
5	1.675299	2.0742×10^{1}	1.807613	1.970×10^{1}

Table 5.2: Constants used in Equation (5.1) to compute the ordinary and extraordinary ray refractive indices of quartz [113, 139].

where λ is the wavelength in micrometers and β_k and λ_k are constants [113, 139], provided in Table 5.2. Birefringence in quartz is low [43], and therefore only the ordinary ray refractive index was used in the SPLITS model.

Data Availability for Hematite

There are many conflicting sources of refractive index data for hematite. These data cover various ranges throughout the electromagnetic spectrum and vary over several orders of magnitude for a given wavelength. This may be due to the difficulties involved in measuring the refractive index for a material that is opaque except when in very thin sections. Popova *et al.* [109] provide complex refractive index data for hematite in the infrared region of the electromagnetic spectrum. Several authors [5, 53, 68, 144] provide data for hematite that partially covers the visible region. The available data also comes in many forms. Marusak *et al.* [83] and Bailey [5] provide absorption coefficient data in cm^{-1}, from which one can calculate the imaginary part of the refractive index [106]. They do not, however, provide data for the real part of the refractive index. Some authors [92, 121] only provide *absorbance* data based on reflection measurements. Absorbance relates the reflected radiance, I, to the incident radiance, I_0, and is

$$\mathcal{A} = \log\left(\frac{I_0}{I}\right).$$

Galuza *et al.* [39] provide plots of the complex dielectric constant, the square of the refractive index, computed using Kramers-Kronig analysis [70, 73]. Several authors [53, 68, 112] provide complex refractive index data for hematite hydrosols,* from which Baikov *et al.* [4] calculated the complex refractive index for hematite in air. Bedidi and Cervelle [12] calculated the complex refractive index for hematite and goethite from reflectance measurements of hematite (respectively goethite) immersed in water and in oil using the Königsberger equations [27, 69]. This method, however, is known to be problematic for highly opaque materials [34]. Sokolik and Toon [130] provide plots for complex refractive index of hematite for the ordinary and for the extraordinary ray. Their plots cover the ranges from 0.2 to 30 μm, with separate plots for the region from 0.2 to 2.5 μm. In the SPLITS model, we use data extracted from the plots by Sokolik and Toon [130] because it was the only source of data we found which:

- covered the entire visible range,
- provided complex refractive index data directly (*i.e.*, we did not have to compute the refractive index from the provided data),
- provided both the real and imaginary parts of the complex refractive index, and
- was not acquired using a method known to have problems.

5.1.3 Density

The densities for the various mineral constituents in the SPLITS model were provided by Mottana *et al.* [90] and are shown in Table 5.1. The midpoint was used for minerals in which a range was given.

5.2 Grain Properties

The following properties describe the sand particles within the medium.

*A hydrosol is a solution of small particles immersed in water [120].

Soil Texture			Entire Soil		Sand		Silt		Clay	
Sand	**Silt**	**Clay**	d_g (mm)	σ_g	d_g (mm)	σ_g	d_g (mm)	σ_g	d_g (mm)	σ_g
100	0	0	0.316	1.64	0.316	1.64	-		-	
90	10	0	0.125	2.23	0.129	2.09	0.272	3.75	-	
85	15	0	0.108	2.32	0.112	2.17	0.173	3.32	-	
90	0	10	0.0899	5.10	0.129	2.09	-		0.0139	4.45

Table 5.3: Geometric mean particle diameter (d_g) and standard deviation (σ_g) for sands with various mixtures of clay, silt and sand-sized particles. The parameters d_g and σ_g are listed for the entire soil and for each of the soil separates individually. The data is provided by Shirazi *et al.* [123].

5.2.1 Particle Size Distribution

The USDA [129] defines sand grains as having particle diameters ranging from 0.05 to 2 mm (Section 2.1). Sand is defined as consisting of at least 85% by weight, and the percentage of silt plus 1.5 times the percentage the clay (by weight) must be less than 15 [129].

Wopfner and Twindale [149] reported median grain sizes of 0.2 to 0.3 mm for dune sands. Leu [77] found sand grains at a beach ranging between 0.32 and 0.95 mm, with a mean of 0.55 mm.

Shirazi and Boersma [122] developed a model using piecewise logarithmic function to represent the particle size distribution of soils. This model was subsequently refined by Shirazi *et al.* [123] by using a piecewise log-normal distribution, parameterized by the geometric mean particle diameter, d_g, and its standard deviation, σ_g. The model was further extended [124] to account for rock fragments (particles larger than 2 mm). In the SPLITS model, as we will not be considering rock fragments, the former refinement [123] shall be used. Data for d_g and σ_g for sands is provided in Table 5.3.

5.2.2 Roundness and Sphericity

The roundness and sphericity used in SPLITS was obtained from data provided by Vepraskas and Cassel [143]. Vepraskas and Cassel evaluated the mean roundness, mean sphericity, and the corresponding standard deviations of sand-sized grains from several coastal soil samples. Five of these soil samples were sands (*i.e.*, the textural class was sand), the data for which are shown in Table 5.4. Roundness and sphericity in the SPLITS model will be given by normally distributed random vari-

	Roundness				Sphericity			
Site	**mean**	**SD**	**min**	**max**	**mean**	**SD**	**min**	**max**
1	0.45	0.07	0.3	0.6	0.78	0.06	0.63	0.91
3	0.47	0.07	0.3	0.6	0.79	0.06	0.61	0.91
4	0.52	0.07	0.4	0.7	0.81	0.07	0.60	0.95
22	0.49	0.08	0.2	0.6	0.81	0.07	0.61	0.94
27	0.48	0.07	0.3	0.6	0.80	0.06	0.67	0.91
mean	0.482	0.072			0.798	0.064		
minimum			0.2				0.60	
maximum				0.7				0.95

Table 5.4: Roundness and sphericity statistics for sand-sized grains from sand samples collected from various sites by Vepraskas and Cassel [143]. The average mean and standard deviation across all five sites, and the union of the ranges, are used in the SPLITS model.

ables, with mean and standard deviation derived by taking the average of the statistics across all of the sites. We shall further constrain the roundness and sphericity to lie within the union of the ranges for each of the five sites.

5.2.3 Coating Thickness

Wopfner and Twindale [149] reported that sand grains between 0.05 mm and 1.2 mm from red dune sands were coated by a crust 1-5 μm thick. The crust was composed of hematite within a matrix of kaolinite and illite.

5.3 Properties of a Sand Medium

The following properties relate to the sand medium as a whole.

5.3.1 Depth

Sand is, for practical purposes, a semi-infinite medium. However, light rarely penetrates beyond several millimeters through sand [93, 101]. For our model, we use a depth of one meter.

5.3.2 Porosity

The *porosity* of a soil is the volume of the pore space a fraction of the total volume. For soils in general, the porosity may vary from as low as 25% to upwards of 60% [18]. A soil that is suitable for plant growth will generally be evenly split between the pore space and the solid portion. However, the porosity varies with soil texture, with coarse soils being less porous than finer soils. For sands, the porosity typically varies between 35% and 50% [17]. For the SPLITS model, we take the midpoint of this range: 42.5%.

5.3.3 Water Content

The water content in the SPLITS model is expressed as the *degree of saturation*, $\mathcal{S}$, which is the fraction of the pore space occupied by water [81]. As such, it varies from zero to one by definition. Sands with varying degrees of saturation will be accounted for by the SPLITS model. Where the degree of saturation is not stated explicitly, however, dry sand ($\mathcal{S} = 0$) shall be the default.

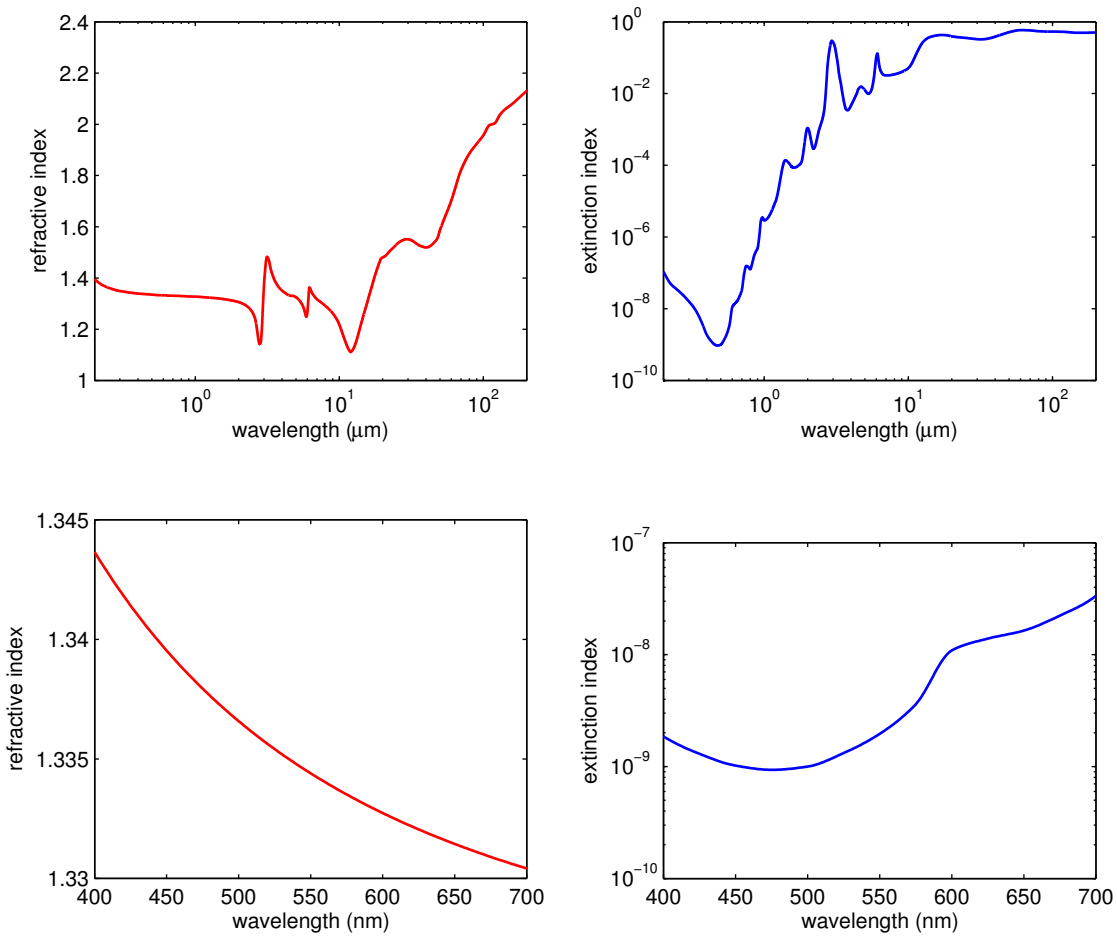

Figure 5.1: Complex refractive index of water. *Top Left*: Real part from 0.2 to 200 μm [45], *Top Right*: Imaginary part from 0.2 to 200 μm [45], *Bottom Left*: Real part in the visible region [67], *Bottom Right*: Imaginary part in the visible region [45].

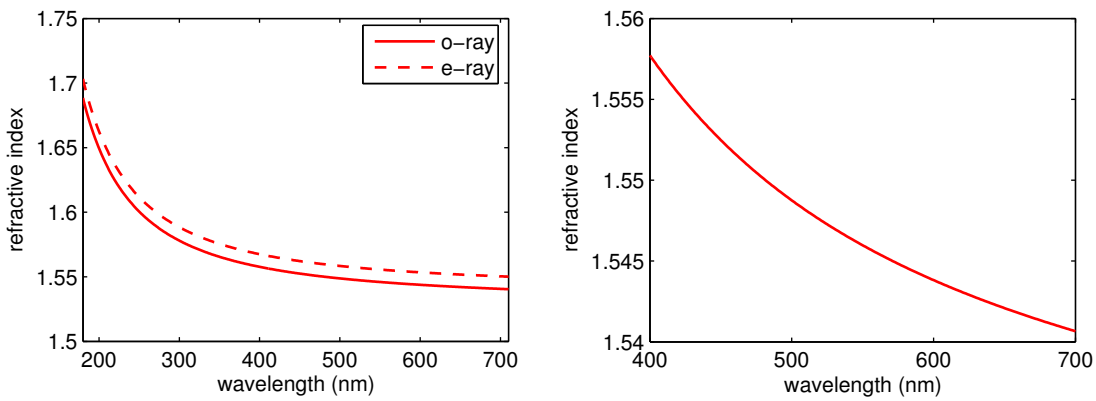

Figure 5.2: Refractive index of quartz [113, 139]. The extinction index of quartz is negligible in the visible region [108]. *Left*: Separate ordinary and extraordinary ray refractive indices over entire domain in which Equation (5.1) is valid. *Right*: Ordinary ray refractive index restricted to the visible range.

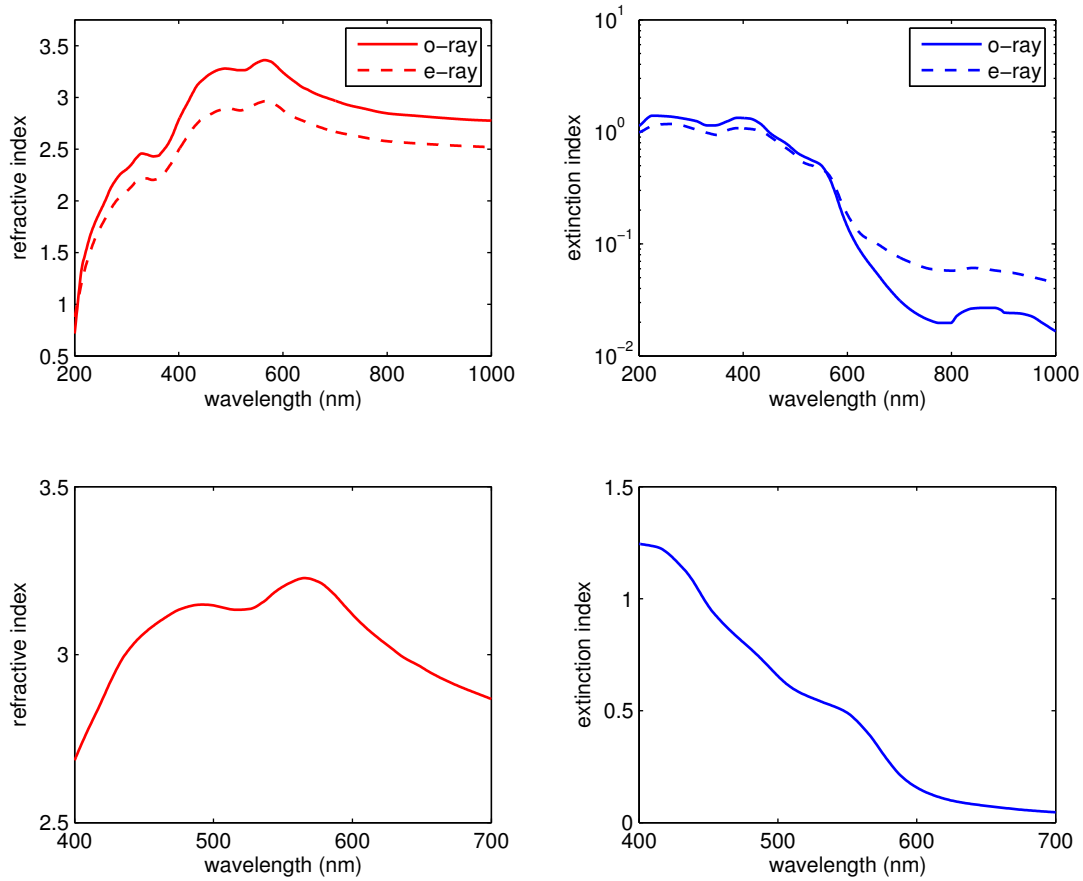

Figure 5.3: Complex refractive index of hematite [130]. *Top Left*: Real part, *Top Right*: Imaginary part, *Bottom Left*: Real part restricted to the visible range (weighted average (Section 4.2) of the ordinary and extraordinary rays), *Bottom Right*: Imaginary part restricted to the visible range (weighted average (Section 4.2) of the ordinary and extraordinary rays).

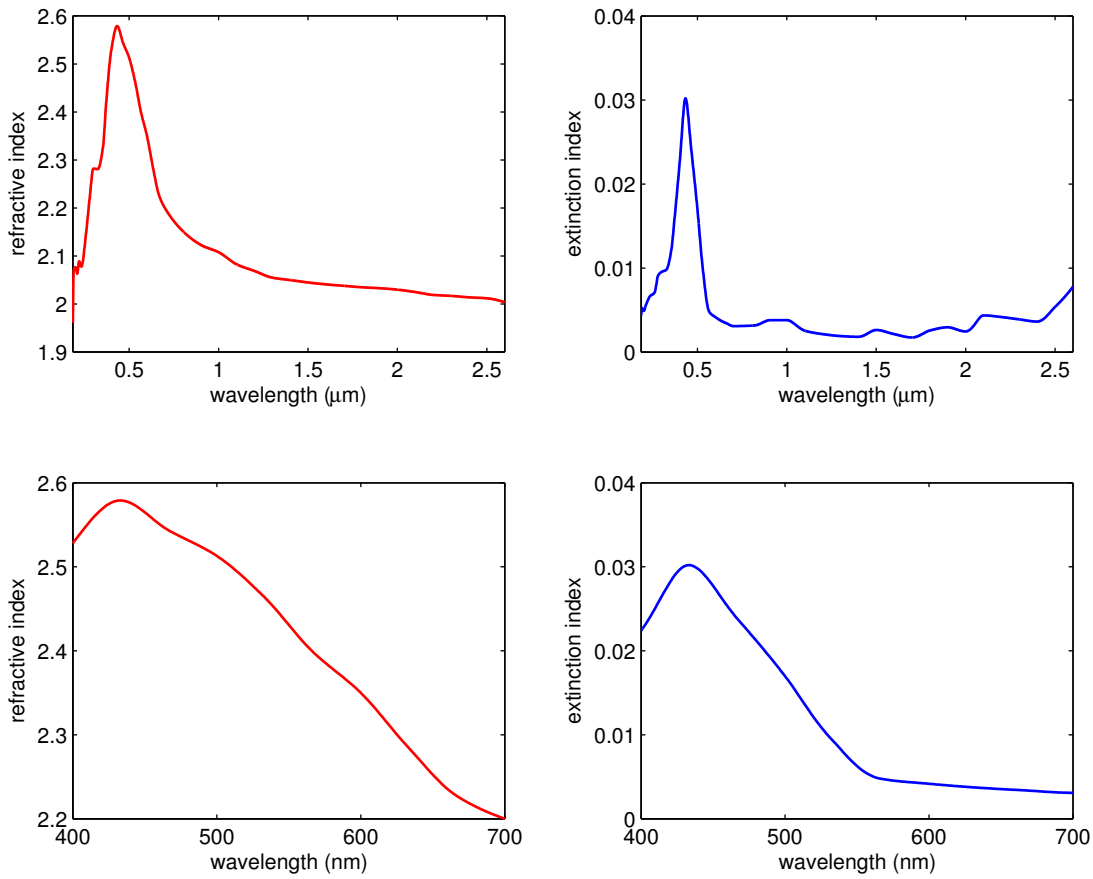

Figure 5.4: Complex refractive index of limonite (goethite) [32]. Only the ordinary ray refractive index was provided. *Top Left*: Real part, *Top Right*: Imaginary part, *Bottom Left*: Real part restricted to the visible range, *Bottom Right*: Imaginary part restricted to the visible range.

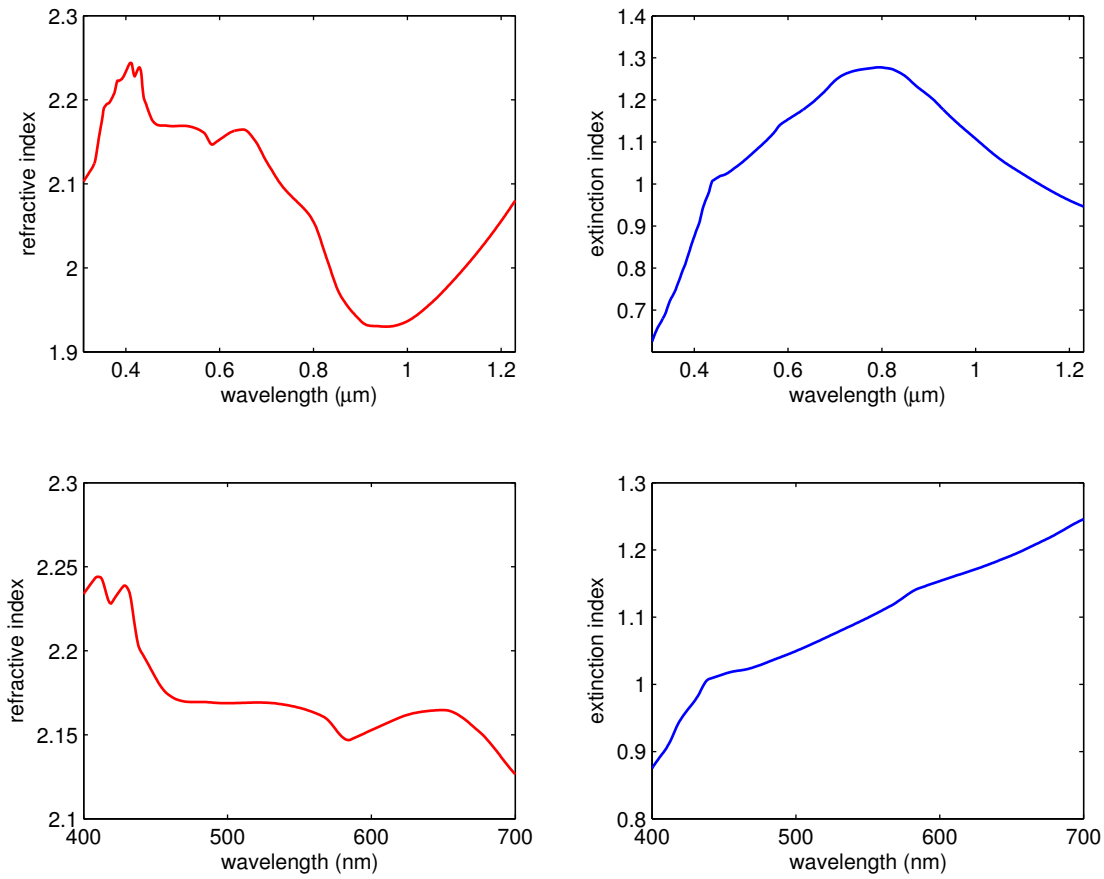

Figure 5.5: Complex refractive index of magnetite [119]. Only the ordinary ray refractive index was provided. *Top Left*: Real part, *Top Right*: Imaginary part, *Bottom Left*: Real part restricted to the visible range, *Bottom Right*: Imaginary part restricted to the visible range.

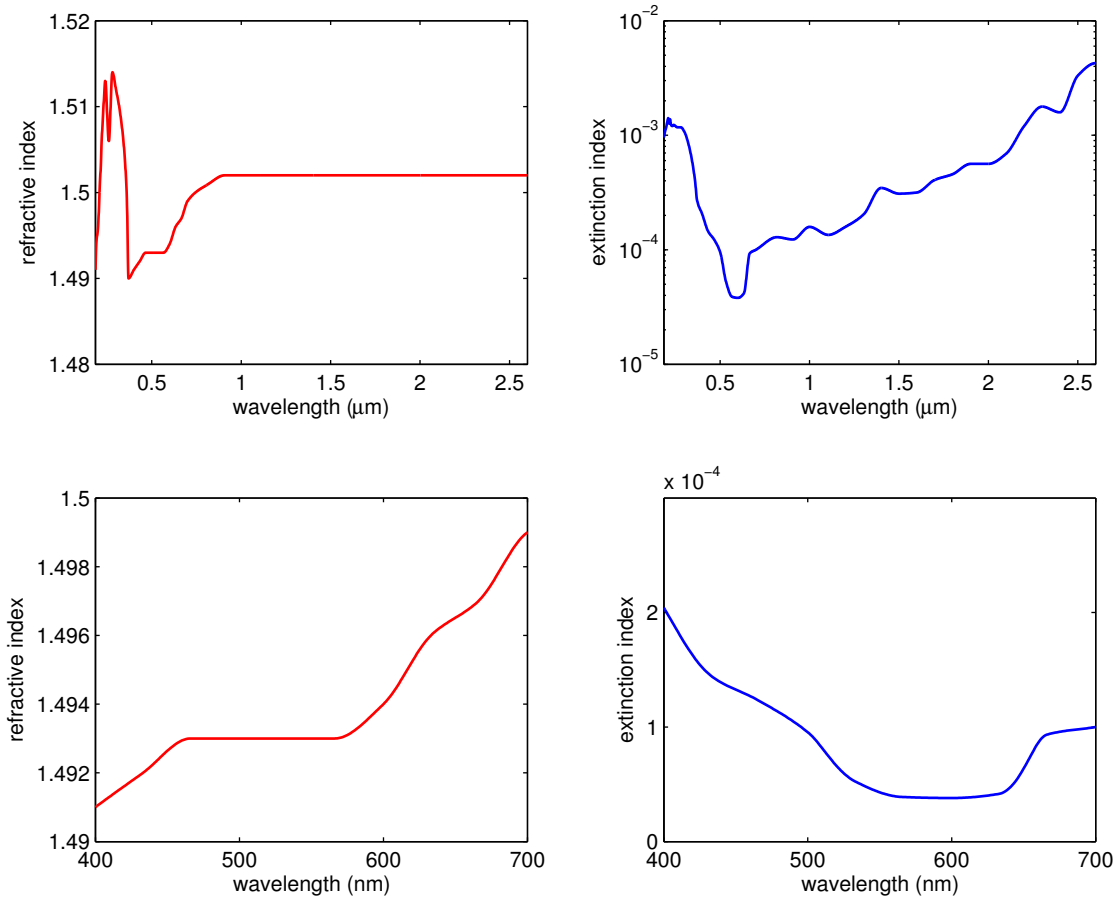

Figure 5.6: Complex refractive index of kaolinite [32]. Only the ordinary ray refractive index was provided. *Top Left*: Real part, *Top Right*: Imaginary part, *Bottom Left*: Real part restricted to the visible range, *Bottom Right*: Imaginary part restricted to the visible range.

Chapter 6

The SPLITS Model

The SPLITS model is a comprehensive light transport model for sand. That is, both the spectral (colour) and spatial (BRDF) responses are simulated. These two components together constitute the *measurement of appearance* [57]. Furthermore, the SPLITS model is dependent on the physical and mineralogical characterization data for sand.

The remainder of this chapter is organized as follows. We begin with a general overview of the model in Section 6.1. The construction of the model is described in Section 6.2. In Section 6.3, the light transport simulation is described. We conclude with an outline of possible extensions supported by the model in Section 6.4.

6.1 Concept

The SPLITS model consists of sand particles that are randomly distributed within the half space below a horizontal plane representing the sand surface. The pore space, defined in Section 2.1, consists of a mixture of air and water. This is depicted in Figure 6.1. The particles are composed of the most important mineral constituents of sands: quartz, hematite, goethite and magnetite. In addition, quartz particles may be contaminated by hematite or goethite, or coated by hematite or goethite in a kaolinite matrix (Section 2.2.1).

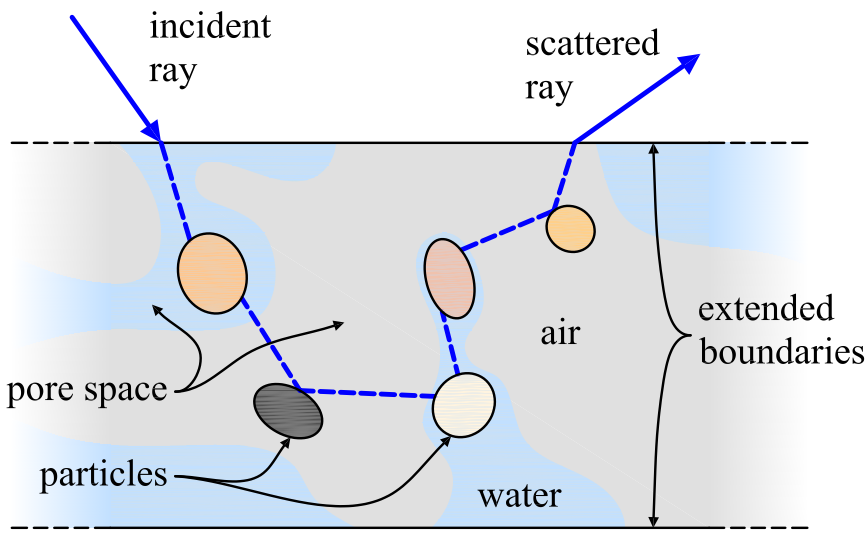

Figure 6.1: Modeled sand medium.

Light propagation in the model is described in terms of geometrical ray optics. Thus, it is assumed that the relevant distances are much larger than the wavelength of the light. This assumption holds over the visible region of the spectrum for sand particles, as they are larger than 0.05 mm in diameter (Section 2.1). It could be argued that an approach based on Mie theory may yield better results. However, simulating Mie theory may add undue complexity and, due to the large size and irregular shape of sand particles, may not result in an improvement over a ray optics approximation [99].

6.2 Construction

We begin by describing the representation of the medium in which the particles are immersed. Next, details are provided for the geometry and composition of individual particles. We then describe how those particles are distributed by size, shape, and composition. Table 6.1 lists the parameters describing the model.

Parameter	Description	Range	Value	Source
$n_w(\lambda)$	refractive index of water	*fixed*	*curve* (see Figure 5.1)	[45]
$n_q(\lambda)$	refractive index of quartz	*fixed*	*curve* (see Figure 5.2)	[139]
$\eta_h(\lambda)$	complex refractive index of hematite	*fixed*	*curve* (see Figure 5.3)	[130]
$\eta_g(\lambda)$	complex refractive index of goethite	*fixed*	*curve* (see Figure 5.4)	[32]
$\eta_m(\lambda)$	complex refractive index of magnetite	*fixed*	*curve* (see Figure 5.5)	[119]
$\eta_k(\lambda)$	complex refractive index of kaolinite	*fixed*	*curve* (see Figure 5.6)	[32]
γ_q	density of quartz	*fixed*	$2.65\,\mathrm{g}\cdot\mathrm{cm}^{-3}$	[139]
γ_h	density of hematite	*fixed*	$5.25\,\mathrm{g}\cdot\mathrm{cm}^{-3}$	[90]
γ_g	density of goethite	*fixed*	$4.30\,\mathrm{g}\cdot\mathrm{cm}^{-3}$	[90]
γ_m	density of magnetite	*fixed*	$5.20\,\mathrm{g}\cdot\mathrm{cm}^{-3}$	[90]
γ_k	density of kaolinite	*fixed*	$2.59\,\mathrm{g}\cdot\mathrm{cm}^{-3}$	[90]
$\mathcal{D}$	depth of the medium	$> 9\,\mathrm{mm}^*$	$1\,\mathrm{m}$	[93]
$\mathcal{P}$	porosity	0.35–0.50	0.425	[17]
$\mathcal{S}$	degree of saturation	0–1	*user specified*	[81]
Ψ	sphericity (random variable)	0.60–0.95	$\overline{\Psi} = 0.798$, $\sigma_\Psi = 0.064$	[143]
$\mathcal{R}$	roundness (random variable)	0.3–0.6	$\overline{\mathcal{R}} = 0.482$, $\sigma_\mathcal{R} = 0.072$	[143]
h'	relative coating thickness	$h = 1$–$5\,\mu\mathrm{m}$	$h' = 5\,\mu\mathrm{m}/1.2\,\mathrm{mm}$	[149]
ζ_1,ζ_2,ζ_3	soil texture (clay, silt, sand)	see Figure 2.3	*user specified*	[129]
μ'_p,μ'_m,μ'_c	partition (pure, mixed, coated)	$\sum \mu' = 1$	*user specified*	Section 6.2.5
ϑ_h	mass concentration of hematite	*see note*†	*user specified*	[24]
ϑ_g	mass concentration of goethite	*see note*†	*user specified*	[24]
ϑ_m	mass concentration of magnetite	*see note*†	*user specified*	[24]

* conservative upper bound on light penetration through sand [93]

† ϑ_{Fe} may be several hundred $\mathrm{g}\cdot\mathrm{kg}^{-1}$ [24]; ϑ_{Fe} defined by Equation (6.3)

Table 6.1: A summary of the model parameters, along with typical ranges and values used.

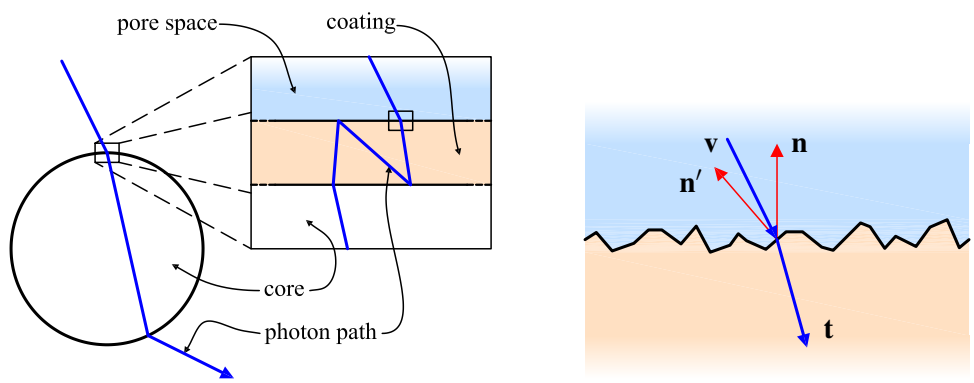

Figure 6.2: An example of the light propagation through a modeled sand particle. *Left*: The particle consists of a core and an optional coating. The small box around the photon path at the coating interface corresponds to the layer interface diagram to the right. *Right*: A closer look at the modeled interface between the core, coating, and/or the surrounding medium.

6.2.1 Extended Boundaries

As previously mentioned, the sand medium is bounded above by a horizontal plane representing the surface. The medium is additionally bounded below by another horizontal plane to prevent runaway photons from occurring during the light transport simulation. These two planes are called the *extended boundaries* (Figure 6.1). The distance, $\mathcal{D}$, between them is set high enough so that light penetration to that depth is negligible (Section 5.3.1).

6.2.2 Pore Space

The pore space, as previously stated, consists of the air and water between the sand particles. The *porosity*, $\mathcal{P}$, defines the volume of pore space as a fraction of sand volume. The volume of water in the sand is expressed using the degree of saturation, $\mathcal{S}$, as defined in Section 5.3.3. The amount of water in the sand may also be expressed as a *volumetric water content*, w, which is the fraction of the *total* volume occupied by water [81]. This may be related to the degree of saturation by $\mathcal{S} = w/\mathcal{P}$.

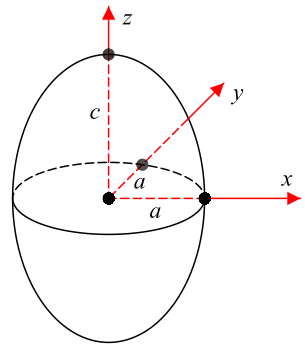

Figure 6.3: Prolate spheroid.

6.2.3 Particle Geometry

Individual particles consist of a core and an optional coating, as depicted in Figure 6.2 (*Left*).

The core is modeled as a prolate spheroid with the semiminor axis of length a and the semimajor axis of length c, with $0 < a \leq c$, as depicted in Figure 6.3. The particle diameter is thus given by $s = 2c$. When placed on a horizontal plane, a prolate spheroid will naturally lay so that the major axis is parallel to the plane. The projection of the prolate spheroid onto a horizontal plane is therefore an ellipse with semiminor and semimajor axes of a and c respectively. Thus, from Equation (2.1), a and c are related to the Riley sphericity, Ψ, by the expression

$$\Psi = \sqrt{\frac{a}{c}}. \tag{6.1}$$

Optionally, the core may be coated by a layer of uniform thickness, h, that is proportional to the particle size, with $h' = h/2c$. The coating thickness is assumed to be small relative to the size of the particle, so that light travelling within the coating does not stray far from the point of entry. Hence, the coating may be approximated locally as a flat slab.

The interfaces between the core, coating, and surrounding medium are modeled using randomly oriented microfacets of equal area to simulate a rough surface, as shown in Figure 6.2 (*Right*). The orientations of the facets are distributed such that the dot product between the microfacet normal,

$\mathbf{n}'$, and the interface normal, $\mathbf{n}$, is given by

$$\mathbf{n}' \cdot \mathbf{n} = 1 - |\mathbf{X}|, \tag{6.2}$$

where $\mathbf{X}$ is normally distributed with zero mean and standard deviation

$$\sigma = \frac{1-\mathcal{R}}{2}.$$

This standard deviation was chosen so that $\mathcal{R} < \mathbf{n}' \cdot \mathbf{n} \leq 1$ for 95% of the facets [116]. Additionally, the microfacet normals are constrained so that $\mathbf{n}' \cdot \mathbf{n} > 0$. The particle roundness, $\mathcal{R}$, is therefore used to control roughness. When $\mathcal{R} = 1$, the interface reduces to a smooth surface, as one would expect based on the concept of roundness [146].

6.2.4 Particle Composition

The minerals used in the model are quartz, hematite, goethite, and magnetite. Additionally, kaolinite is used as the coating matrix (Section 2.2.1). These minerals may occur in pure form or as a mixture. The complex refractive indices of the constituent materials are provided in Chapter 5. These data may also be obtained from the various works cited in Table 6.1. To represent a mixed material, we use the equation from Maxwell Garnett theory (Equation (4.5) in Section 4.3) previously used by Okin and Painter [100].

6.2.5 Particle Types

The particles are divided among the following eight types: *pure* (quartz (`pq`), hematite (`ph`), goethite (`pg`), and magnetite (`pm`)), *mixed* (hematite with quartz (`mh`) and goethite with quartz (`mg`)), and *coated* (hematite coated quartz (`ch`) and goethite coated quartz (`cg`)). The hematite and goethite in the coatings are present in the form of inclusions in a kaolinite matrix (Section 2.2.1).

Ultimately, we must determine the fraction of volume, $v_j(1-\mathcal{P})$, occupied by particles of type j, as j varies over each of the eight particle types (`pq`, `ph`, `pg`, `pm`, `mh`, `mg`, `ch`, `cg`). For the mixed

Particle Type	Mineral				*Total*
	Quartz	**Hematite**	**Goethite**	**Magnetite**	
Pure	β_q	$r_{hg}\beta_{hg}$	$(1-r_{hg})\beta_{hg}$	ϑ_m	μ'_p
Mixed	-	$r_{hg}\mu'_m$	$(1-r_{hg})\mu'_m$	-	μ'_m
Coated	-	$r_{hg}\mu'_c$	$(1-r_{hg})\mu'_c$	-	μ'_c
Total	β_q	$r_{hg}(\beta_{hg}+\mu'_m+\mu'_c)$	$(1-r_{hg})(\beta_{hg}+\mu'_m+\mu'_c)$	ϑ_m	1

Table 6.2: Mass fractions, μ_j, of each of the different classes, j, of particles. The quantities β_q and β_{hg} are unknowns, given by Equations (6.7) and (6.6) respectively.

Particle Type		Mineral				
		Quartz	**Hematite**	**Goethite**	**Magnetite**	**Kaolinite**
Pure	**Quartz**	1	0	0	0	0
	Hematite	0	1	0	0	0
	Goethite	0	0	1	0	0
	Magnetite	0	0	0	1	0
Mixed	**Hematite**	$1-\vartheta_{hg}$	ϑ_{hg}	0	0	0
	Goethite	$1-\vartheta_{hg}$	0	ϑ_{hg}	0	0
Coated	**Hematite**	$1-\vartheta_{hg}-\vartheta'_k$	ϑ_{hg}	0	0	ϑ'_k
	Goethite	$1-\vartheta_{hg}-\vartheta''_k$	0	ϑ_{hg}	0	ϑ''_k

Table 6.3: Mass concentration, $\vartheta_{j,\ell}$, of the constituent minerals, ℓ, in each of the different classes j of particles. The quantities ϑ'_k and ϑ''_k are unknowns given by Equations (6.8) and (6.9) respectively.

particles, we must also determine the volume concentration, $\nu_{j,\ell}$, of each of the constituent minerals ℓ within the particle, required to apply Equation (4.5). For the coated particles, we must determine the volume concentration of the inclusions within the coating, which may be computed from the overall volume concentrations, $\nu_{j,\ell}$, of each of the mineral constituents of the particle. We begin by determining the mass fraction, μ_j, of each of the various types of particles (Table 6.2), and the mass concentration, $\vartheta_{j,\ell}$, of each mineral, ℓ, within particles of each type, j (Table 6.3).

The overall mass concentrations of hematite, goethite, and magnetite in the simulated sand is controlled, respectively, by ϑ_h, ϑ_g, and ϑ_m. In addition, we define some additional quantities. We define the iron oxide concentration as

$$\vartheta_{Fe} = \vartheta_h + \vartheta_g + \vartheta_m. \tag{6.3}$$

Because of the particular importance of hematite and goethite (as noted in Section 2.2.1), we also

define the concentration of these two minerals,

$$\vartheta_{hg} = \vartheta_h + \vartheta_g, \tag{6.4}$$

and a ratio describing the relative proportions of hematite and goethite,

$$r_{hg} = \frac{\vartheta_h}{\vartheta_h + \vartheta_g}. \tag{6.5}$$

The concentrations of hematite and goethite may be given equivalently by the above two quantities. For simplicity, the concentration of hematite (respectively goethite) in the mixed and coated particles containing hematite (respectively goethite) is fixed at ϑ_{hg}. The remainder of the mineral matter is quartz (within particle cores) and kaolinite (within coatings).

Three parameters, μ'_p, μ'_m, and μ'_c, partition the particles by mass into the pure, mixed, and coated particles respectively, with $\mu'_p + \mu'_m + \mu'_c = 1$. These parameters are further constrained by the concentrations of the various mineral constituents, since, for example, a particle consisting of a quartz core coated by a mixture of hematite and kaolinite has an upper bound on hematite concentration within that particle.

From the above parameters, we may now derive the mass fraction, μ_j, of each of the various categories, j, of particles. These are indicated in Table 6.2, with two unknowns, β_q and β_{hg}. Since we are given the total mass concentration of hematite, ϑ_h, and the mass concentration of hematite in each of the particle types (provided in Table 6.3), we have the relationship

$$r_{hg}\beta_{hg} + \vartheta_{hg} r_{hg} \mu'_m + \vartheta_{hg} r_{hg} \mu'_c = \vartheta_h.$$

From Equations (6.4) and (6.5), we see that $\vartheta_{hg} r_{hg} = \vartheta_h$. Substituting and solving for β_{hg} yields

$$\beta_{hg} = \frac{\vartheta_h (1 - \mu'_m - \mu'_c)}{r_{hg}}.$$

Noting that $\mu'_p = 1 - \mu'_m - \mu'_c$, we get

$$\beta_{hg} = \frac{\vartheta_h \mu'_p}{r_{hg}} = \vartheta_{hg} \mu'_p. \tag{6.6}$$

The reader may wish to verify that we arrive at the same result if we relate the concentration of goethite in each particle types to the total goethite concentration. Now we may solve for β_q. Since top row in Table 6.2 must sum to μ'_p, we have

$$\beta_q = \mu'_p - \vartheta_m - \beta_{hg}. \tag{6.7}$$

Next, we must determine the two unknowns, ϑ'_k and ϑ''_k, in Table 6.3. These quantities correspond to mass concentrations of kaolinite in the hematite coated quartz and the goethite coated quartz particles, respectively. Recall that the hematite coated quartz particles consist of a pure quartz core coated in a mixture of hematite and kaolinite. Hence, to determine ϑ'_k, corresponding to the mass concentration of kaolinite within the particle (Table 6.3), we need to know the volume of the coating as a fraction of the total volume of the particle, ν_{coat}. Solving for ϑ'_k (see Section B.3 for details) then yields

$$\vartheta'_k = \frac{\gamma_k}{\gamma_h} \left(\frac{\gamma_h \nu_{coat}(1-\vartheta_{hg}) - \gamma_q(1-\nu_{coat})\vartheta_{hg}}{\gamma_q(1-\nu_{coat}) + \gamma_k \nu_{coat}} \right). \tag{6.8}$$

Similarly,

$$\vartheta''_k = \frac{\gamma_k}{\gamma_g} \left(\frac{\gamma_g \nu_{coat}(1-\vartheta_{hg}) - \gamma_q(1-\nu_{coat})\vartheta_{hg}}{\gamma_q(1-\nu_{coat}) + \gamma_k \nu_{coat}} \right). \tag{6.9}$$

The volume of the coating may be estimated as $A_S h$, where A_S is the surface area of the particle, since we are assuming that the $h \ll s$. Therefore,

$$\nu_{coat} \approx \frac{A_S(s,\Psi)h}{V(s,\Psi) + A_S(s,\Psi)h},$$

where V is the volume of the particle. Dividing the numerator and denominator by V yields

$$\nu_{coat} \approx \frac{A_V(s,\Psi)h}{1+A_V(s,\Psi)h}, \tag{6.10}$$

where $A_V(s,\Psi) = A_S(s,\Psi)/V(s,\Psi)$ is the *surface area to volume ratio* of the particle. Noting that

$$A_V(s,\Psi) = \frac{A_S(s,\Psi)}{V(s,\Psi)} = \frac{s^2 A_S(1,\Psi)}{s^3 V(1,\Psi)} = s^{-1} A_V(1,\Psi),$$

and that, by definition, $h = h's$, the particle size, s, may be eliminated from Equation (6.10), yielding

$$\nu_{coat} \approx \frac{A_V(1,\Psi)h'}{1+A_V(1,\Psi)h'}. \tag{6.11}$$

The surface area to volume ratio of a prolate spheroid with $s = 2c = 1$ (see Section 7.4.1) is given by

$$A_V(1,\Psi) = 3\left(1 + \frac{\sin^{-1}\sqrt{1-\Psi^4}}{\Psi^2\sqrt{1-\Psi^4}}\right). \tag{6.12}$$

For simplicity, we use the mean sphericity, $\overline{\Psi}$, in the above (*i.e.*, $A_V(1,\overline{\Psi})$) rather than having ν_{coat}, and thus ϑ_k' and ϑ_k'', vary with sphericity.

Now that we know, for each particle type j, the mass concentration $\vartheta_{j,\ell}$ of each mineral ℓ (Table 6.3), we may compute the density of a particle of type j (see Section B.1),

$$\gamma_j = \left(\sum_\ell \frac{\vartheta_{j,\ell}}{\gamma_\ell}\right)^{-1}. \tag{6.13}$$

Similarly (Section B.1), we may compute the particle density,* γ, knowing the mass fractions μ_j of each particle type j (Table 6.2). This is given by

$$\gamma = \left(\sum_j \frac{\mu_j}{\gamma_j}\right)^{-1}. \tag{6.14}$$

*The particle density is the density of the solid particles comprising the sand [17], corresponding to the mean density of the individual particles.

Knowing the mass fractions and densities of the components of a mixture allows us to compute the volume fractions (Section B.2). Thus, we may now compute the volume concentrations of all the minerals within a particle, as well as the volume fractions of each particle type. The former is given by

$$\nu_{j,\ell} = \frac{\gamma_j}{\gamma_\ell}\vartheta_{j,\ell}, \tag{6.15}$$

and the latter by

$$\nu_j = \frac{\gamma}{\gamma_j}\mu_j. \tag{6.16}$$

For hematite coated particles, the volume fraction of hematite within the coating, required to compute the complex refractive index of the mixture of hematite and kaolinite, is $\nu_{\mathtt{ch},h}/(\nu_{\mathtt{ch},k}+\nu_{\mathtt{ch},h})$. The volume fraction of goethite within the coating of the goethite coated particles is determined similarly.

6.2.6 Shape and Size Distribution

The size and shape of the particles are randomly distributed and are independent of one another. That is, the conditional size distribution for any two shapes is the same.

The sphericity is normally distributed, with the mean and the standard deviation derived (in Section 5.2.2) from data provided by Vepraskas and Cassel [143], and presented in Table 6.1. The sphericity is also constrained to fall within a range derived from the same data.

The particle size is distributed according to a piecewise* log-normal distribution as suggested by Shirazi *et al.* [123]. That is, $\log s$ is normally distributed. This distribution is characterized by two parameters: the geometric mean particle diameter, d_g, and its standard deviation σ_g, which are functions of soil texture (as defined in Section 2.1). It is important to note that, since the distribution is specified in a *piecewise* manner, there will be a different d_g and σ_g for each soil separate. Defining

$$\mathfrak{f}_g(s) = \frac{1}{b_g\sqrt{2\pi}}\exp\left(\frac{-(\log s - a_g)^2}{2b_g^2}\right), \tag{6.17}$$

*There is one piece for each soil separate.

where $a_g = \log d_g$ and $b_g = \log \sigma_g$, the mass fraction of the particles with sizes ranging from s_1 to s_2 is then given by

$$\mathfrak{F}_m(s_1, s_2) = \int_{s_1}^{s_2} s^{-1} \mathfrak{f}_g(s)\, ds. \tag{6.18}$$

Assuming that particle density does not vary significantly with size, $\mathfrak{F}_m(s_1, s_2)$ may also be interpreted as a volume fraction. This approximation is justified by the fact that the silt and sand-sized particles are dominated by quartz [17]. Shirazi *et al.* [123] provide a table for determining d_g and σ_g from texture. An abridged version of this table, restricted to sandy soils, is provided in Section 5.2.1. For sands with textures not listed in the table, d_g and σ_g may be computed using the following procedure, as explained by Shirazi *et al.* [123]. First, we fix $Z_{min} = 0.0001$ and $Z_{max} = 0.9999$. Defining $\Delta Z = Z_{max} - Z_{min}$, we then scale the mass fractions of the soil separates, ζ_j, yielding $\zeta'_j = \zeta_j \Delta Z$ for $1 \leq j \leq 3$. Next, we define the cumulative mass fractions of the (scaled) soil separates, $Z_0 = Z_{min}$ and

$$Z_j = Z_{j-1} + \zeta'_j,$$

for $1 \leq j \leq 3$. We then let $Y_j = \Phi^{-1}(Z_j)$ for each j, where Φ is the cumulative density function for a unit normal random variable. Next, we set

$$s_0 = 0.00005\,\text{mm},$$

$$s_1 = 0.002\,\text{mm},$$

$$s_2 = 0.05\,\text{mm},$$

$$s_3 = 2.0\,\text{mm}.$$

These are, except for s_0, the limits for the three soil separates (Table 2.1). The additional value s_0 is required for this procedure not to yield infinite results. Next, we define $x_j = \log s_j$ for each $0 \leq j \leq 3$ and

$$m_j = \frac{Y_j - Y_{j-1}}{x_j - x_{j-1}},$$

for $1 \leq j \leq 3$. Finally, for clay ($j = 1$), silt ($j = 2$), and sand ($j = 3$), we have $a_g = x_j - Y_j/m_j$ and $b_g = 1/m_j$, from which we may derive $d_g = 10^{a_g}$ and $\sigma_g = 10^{b_g}$ respectively.

6.3 Light Transport Simulation

When a ray is incident at the outer extended boundary of the sand medium, it is either reflected or refracted, with the probability of reflection given by the Fresnel equations (Section 4.5). Once a photon penetrates the outer boundary, it has entered the medium. The photon is then repeatedly scattered by the sand particles until it escapes the medium or is absorbed. Rather than explicitly represent and store each particle, however, they are generated stochastically as needed and subsequently discarded. Thus, each ray in essence *sees* a different instantiation of the sand medium. For rendering applications in which we are concerned about the appearance of the sample from afar, this acceptable since the response would be averaged over the area of a pixel, which would correspond to a large area of sand. Thus, each ray cast randomly through a point within the pixel would likely intercept a different region of the sand surface anyway. The simulation of the fine variation in the appearance of sand as seen from close up is beyond the scope of this work. Possible methods for handling this would be to use a texture map to vary the parameters to the model, or to store the stochastically generated particles as they are generated and reuse them when subsequent rays are cast at the simulated sand medium. The light transport simulation process is depicted in Figure 6.4.

6.3.1 Extended Boundaries

A photon reaching the surface extended boundary from the inside, as from the outside, is reflected with a probability given by the Fresnel equations (Section 4.5). If internally reflected, the photon continues traversing the medium. Otherwise, the photon escapes the medium and the scattered ray is returned. When a photon reaches the lower extended boundary, it is absorbed.

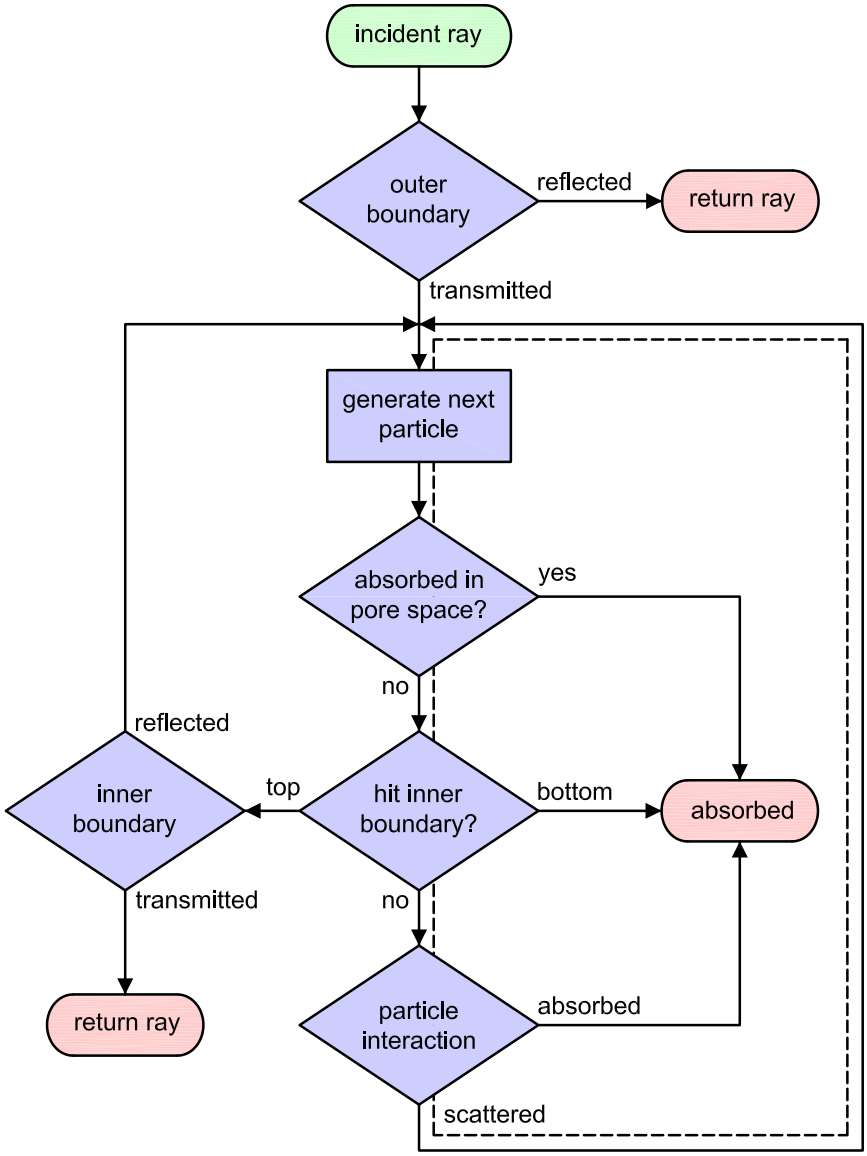

Figure 6.4: Flowchart outlining the light transport algorithm used by the SPLITS model. The dashed line indicates the main loop. The term *inner* boundary refers to the inside of either extended boundary, whereas the *outer* boundary is the outside of the surface extended boundary.

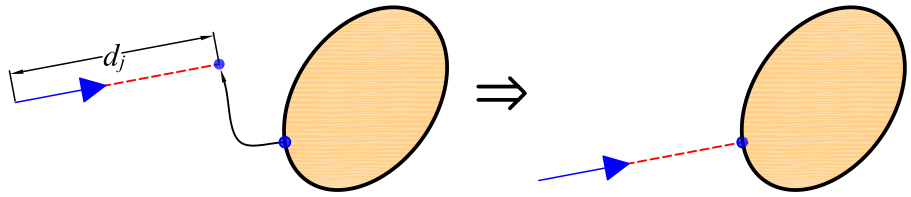

Figure 6.5: Generating the next particle for the photon to interact with. *Left*: The distance to the next particle, the sphericity, roundness, particle size, orientation, and the point on the surface of the particle to be intercepted is generated randomly. *Right*: The particle is positioned so that the ray intercepts the particle at the selected point.

6.3.2 Pore Space

Each time the photon path reaches an interface to the pore space, the medium representing the pore space is selected randomly. The degree of saturation, $\mathcal{S}$, defined in Section 5.3.3, is used to partition the pore space into air and water. Water is selected with probability $\mathcal{S}$ to represent the pore space. Air is selected with probability $1-\mathcal{S}$. This selection is made when an incident ray approaches, as well as when the photon reaches the outer interface of a particle from the inside.

6.3.3 Generating a Sand Particle

As previously stated (Section 6.1), we do not explicitly store each sand particle. Rather, they are generated *on the fly*. The light interaction with this particle is then simulated, and the particle is then discarded. In a conventional ray tracing approach, particles would be stored explicitly. Random variables such as the distance to the next particle, the shape, size, and composition of the particle that is intercepted, and the point on the surface of the particle that is intercepted, arise implicitly as a consequence of the ray tracing simulation. Conversely, in the SPLITS model, we compute the probability distribution functions for these random variables and sample them explicitly (Figure 6.5). In addition, we ensure that the particle lies completely between the extended boundaries and that the particle does not intersect with the previous ray.

The physical distance to the next particle is determined by randomly choosing a distance for each category j of particles and then selecting the category for which that distance is minimal. The

distance, d_j, to the next particle of type j is an exponential random variable with a mean of $1/K_j$, where K_j is the *geometric attenuation coefficient*[*] for particles of type j. This distance is given by

$$d_j = -\frac{1}{K_j}\log\xi, \tag{6.19}$$

where ξ is uniformly distributed on $(0,1)$ [116].

For prolate spheroids with normally distributed sphericity and log-normally distributed size, K_j reduces (Section 7.4.1) to

$$K_j = K_1 K_2, \tag{6.20}$$

where

$$K_1 = \nu_j \frac{\int_{s_{min}}^{s_{max}} s^{-2}\mathfrak{f}_g(s)\,ds}{\int_{s_{min}}^{s_{max}} s^{-1}\mathfrak{f}_g(s)\,ds}, \tag{6.21}$$

and

$$K_2 = \frac{\int_{\Psi_{min}}^{\Psi_{max}} A_V(1,\Psi)\Phi'(\overline{\Psi},\sigma_\Psi^2)(\Psi)\,d\Psi}{4\int_{\Psi_{min}}^{\Psi_{max}} \Phi'(\overline{\Psi},\sigma_\Psi^2)(\Psi)\,d\Psi}. \tag{6.22}$$

The particle size distribution, $\mathfrak{f}_g(s)$, is given by Equation (6.17), $A_V(1,\Psi)$ by Equation (6.12), and $\Phi'(\overline{x},\sigma^2)(x)$ is the probability density function for the normal distribution with mean $\overline{x}$ and variance σ^2 [116].

The particle size, s, is then chosen according to the probability density function

$$f_s(s') = \frac{1}{C_1}\mathfrak{f}_g(s')s'^{-2}, \tag{6.23}$$

and the sphericity, Ψ, is chosen according to

$$f_\Psi(\Psi') = \frac{1}{C_2}A_V(\Psi')\Phi'(\overline{\Psi},\sigma_\Psi^2)(\Psi'), \tag{6.24}$$

[*]We use the term *geometric attenuation coefficient* to mean the geometric cross sectional area per unit volume (in m^{-1}). The qualification *geometric* is used to avoid confusion with the term *attenuation coefficient* and its various applications [15, 110].

where C_1 and C_2 are the constants that ensure that f_s and f_Ψ (respectively) integrate to one over their domain (Section 7.4.1). Note that Equation (6.23) does not match the distribution provided by Shirazi *et al.* [123] shown in the integrand of Equation (6.18). This follows from the distinction between the particle size distribution by *mass*, provided by Shirazi *et al.* [123] (or by *volume* as we are interpreting it), and the distribution of particle sizes struck by rays travelling randomly through the medium (Chapter 7).

Now that we have the particle size, s, the coating thickness is then given by $h = h's$, where h' is the relative coating thickness specified in Table 6.1. Additionally, the particle roundness, $\mathcal{R}$ is given by a normal random variable with mean $\overline{\mathcal{R}}$ and standard deviation $\sigma_{\mathcal{R}}$ given in Table 6.1.

The point on the surface of the particle which is struck is chosen uniformly on the side of the particle surface facing the ray origin. To select a point uniformly on a prolate spheroid (Figure 6.3), we set $z = cF^{-1}(2\xi_1 - 1)$, where ξ_1 is a uniform random number on $(0,1)$, $F(u)$ is the fraction of the surface area of the spheroid above the plane $z = u$, given by

$$F(u) = \frac{1}{2}\left(1 + \frac{eu\sqrt{1-e^2u^2} + \sin^{-1} eu}{e\sqrt{1-e^2} + \sin^{-1} e}\right), \tag{6.25}$$

and $e = \sqrt{1-\Psi^4}$ (see Appendix A). Since F^{-1} is difficult to compute analytically, F may be inverted using numerical techniques. The other two coordinates are then given by $x = ar\cos\theta$ and $y = ar\sin\theta$, with $\theta = 2\pi\xi_2$ (ξ_2 being another canonical random variable) and $r = \sqrt{1-z^2/c^2}$. To restrict the generated point to the side of the particle facing the ray origin, we transform the ray direction $\mathbf{v}$ into the particle's local coordinate space to get $\mathbf{v}'$, and compute the normal $\mathbf{n}$ at the chosen point. We then use the point (x,y,z) if $\mathbf{n}\cdot\mathbf{v}' < 0$ and $(-x,-y,-z)$ otherwise.

Before we simulate light interaction with this particle, we first check the validity of the particle as depicted in Figure 6.6. If the point, $\mathbf{q}$, that is d units along the ray lies outside the extended boundaries, the photon will instead interact with the boundary as described in Section 6.3.1. If the randomly generated particle intersects with either boundary, the particle is rejected. To account for

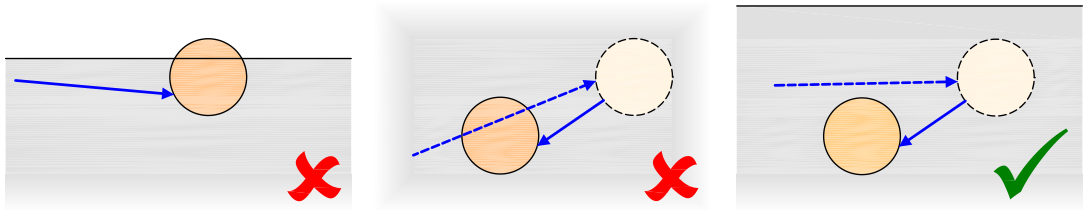

Figure 6.6: Tests performed before accepting the generated sand particle. *Left*: A particle that intersects an extended boundary is rejected. *Middle*: A particle that intersects the previous leg of the path is rejected. *Right*: Otherwise, the particle is accepted.

the opposition effect* [49], the particle is also rejected if it intersects with the last leg of the path. If the particle is rejected, the above process of generating a distance and particle intersection point is repeated.

6.3.4 Light Propagation Within a Sand Particle

Light propagation within a sand particle is simulated using a random walk process as exemplified in Figure 6.2. A photon incident upon the particle first interacts with the outer interface: either between the pore space and the coating or between the pore space and the core if no coating is present. The photon may be reflected or transmitted at each interface. When the photon is transmitted into the core (or internally reflected back into the core) a ray-particle intersection is computed to determine the next point at which the photon may exit the core. Absorption is simulated within the coating and within the core. This process is repeated until the photon escapes the particle or is absorbed.

At each interface, the microfacet normal is selected according to Equation (6.2). As mentioned in Section 6.2.3, the microfacets are of equal area, A. The *projected* area with respect to the incident ray, $\mathbf{v}$, is therefore $A|\mathbf{n}' \cdot \mathbf{v}|$. Hence, the probability that an incident ray $\mathbf{v}$ strikes a microfacet with normal $\mathbf{n}'$ should be scaled by $|\mathbf{n}' \cdot \mathbf{v}|$. This is accomplished using the rejection method [116]. The photon is then reflected in $\mathbf{n}'$ with a probability once again determined using the Fresnel equations (Section 4.5), considering the media on either side of the interface. Otherwise, the photon is re-

*The opposition effect refers to the increase in reflectance toward the source of illumination due to shadow hiding [49].

fracted according to Snell's Law for absorbing media [16], described in Section 4.4. If the ray was to be reflected and $\mathbf{n} \cdot \mathbf{r} < 0$ (where $\mathbf{r}$ is the reflected vector), or if the ray was to be refracted and $\mathbf{n} \cdot \mathbf{t} > 0$, then multiple scattering is approximated using a cosine lobe centered around $\mathbf{n}$ (respectively $-\mathbf{n}$) [148].

Given the extinction index, k, of the coating or of the core, absorption within the coating or within the core is then simulated according to Lambert's Law [125]. The light is transmitted a distance d with probability $T = \exp(-\alpha d)$, where α is the absorption coefficient, given by

$$\alpha = \frac{4\pi k}{\lambda}$$

[106]. For the coating, $d = h/|\mathbf{n} \cdot \mathbf{t}|$, where $\mathbf{t}$ is the ray transmitted through the coating. For the core, d is determined from the ray-particle intersection.

6.4 Extensibility

The framework for SPLITS supports several possible extensions. The model may be extended to include other minerals, given their densities and spectral complex refractive indices. The model can also be extended to include other particle shape and size distributions (Chapter 7). Additionally, multiple coatings may be applied to the particles.

Chapter 7

Formal Sand Particle Distributions

7.1 Motivation

The sand particles used in the model may be of arbitrary shapes and sizes (Section 6.4). Even arbitrary *distributions* of particle shapes and sizes may be used, provided that the following criteria are met. First, the following operations must be supported by the individual particles:

- translation,
- ray-particle intersection (nearest intersection only),
- generation of a random point uniformly over the surface,
- computation of the extent along the z-axis.

Translation is required so that particles may be placed at any location within the sand medium. The computation of the extents of the particle is needed to determine if it lies completely within the extended boundaries of the medium. To select the point at which a ray travelling through the medium intercepts the particle, we need to generate a random point uniformly over its surface. Finally, ray-particle intersection is required for two reasons: to simulate scattering within the particle's core and, in the case of a non-convex particle, to determine if the randomly generated point is obscured by another part of the particle.

In addition, we must be able to compute a path length, d, to the nearest particle within the medium, and determine the geometry of the intercepted particle. To accomplish this, we formalize the concept of a particle's geometry and of a distribution of particle geometries, and develop a framework around these concepts. This framework is then applied to specific cases, including the particle distribution used in the SPLITS model.

For the remainder of this chapter, it is assumed that the reader has the relevant background in probability and in analysis. The reader is referred to the work of Ross [116] for an introduction to probability and to the excellent works by Marsden and Hoffman [82] and by Royden [118] for the background in analysis.

7.2 Prerequisites

We first define what is meant by an exponential random variable.

Definition 7.2.1. A random variable X is said to be *exponentially distributed* [116] with *parameter* K if its probability density function is given by

$$f_X(x) = K \exp(-Kx). \tag{7.1}$$

The cumulative density function for an exponentially distributed random variable, X, with parameter K is given by

$$F_X(x) = 1 - \exp(-Kx). \tag{7.2}$$

We will also require the following result, which will be used (Section 7.3.3) to show that we may compute the path length and the particle geometry independently.

Theorem 7.2.2. *Let $X_1, \ldots, X_m$ be independent, exponentially distributed random variables with parameters $K_1, \ldots, K_m$ respectively, and define $N = j$ such that $X_j < X_k$ for all $k \neq j$. Also, define*

$Y = X_N$. Then Y and N are independent, Y is exponentially distributed with parameter

$$K = \sum_j K_j, \tag{7.3}$$

and N is distributed according to

$$\Pr(N = j) = \frac{K_j}{K}. \tag{7.4}$$

Proof. First, we require the joint probability density function, $f_{Y,N}$, for Y and N; *i.e.*, intuitively, $f_{Y,N}(x, j)\,dx$ is the infinitesimal probability that $Y \approx x$ and $N = j$. However, $Y = x$ and $N = j$ if and only if $X_j = x$ and $X_k > X_j$ for each $k \neq j$. Thus,

$$\begin{aligned}
f_{Y,N}(x, j) &= f_{X_j}(x) \prod_{k \neq j} \Pr(X_k > x) \\
&= f_{X_j}(x) \prod_{k \neq j} (1 - F_{X_k}(x)) \\
&= K_j \exp(-K_j x) \prod_{k \neq j} \exp(-K_k x) \\
&= K_j \prod_k \exp(-K_k x) \\
&= K_j \exp\left(-\left(\sum_k K_k\right) x\right).
\end{aligned}$$

Substituting Equation (7.3) into the above yields

$$f_{Y,N}(x, j) = K_j \exp(-Kx). \tag{7.5}$$

We first demonstrate that Y is exponentially distributed with its parameter given by Equation (7.3). We evaluate f_Y by conditioning on the event that $X_k > X_j$ for all $k \neq j$ and then summing over j, yielding

$$f_Y(x) = \sum_j f_{Y,N}(x, j) = \sum_j K_j \exp(-Kx) = K \exp(-Kx).$$

Hence, Y is exponentially distributed with its parameter given by Equation (7.3), as claimed.

Next, we prove that N is distributed according to Equation (7.4). $N = j$ if and only if $X_k > X_j$ for all $k \neq j$. We may compute $\Pr(N = j)$ by conditioning on the event that $X_j = x$. Integrating over $x \in (0, \infty)$ yields

$$\Pr(N = j) = \int_0^\infty f_{Y,N}(x, j)\, dx = K_j \int_0^\infty \exp(-Kx)\, dx.$$

As $\int \exp(-Kx)\, dt = \exp(-Kx)/(-K)$, we have

$$\Pr(N = j) = K_j \left(0 - \frac{1}{-K}\right) = \frac{K_j}{K}.$$

Finally, we must demonstrate that Y and N are indeed independent.

$$f_{Y,N}(x, j) = K_j \exp(-Kx) = \left(\frac{K_j}{K}\right) K \exp(-Kx) = \Pr(N = j) f_Y(x). \qquad \square$$

7.3 Abstract Particle Distributions

7.3.1 Definitions

We begin with a formal definition for a particle geometry, which is, intuitively, a translation invariant shape.

Definition 7.3.1. A particle *geometry*, $\mathbf{x}$, is a closed, bounded, path connected subset of $\mathbb{R}^3$ with its centroid at the origin. That is, integrating over all points $\mathbf{p} \in \mathbf{x}$ yields

$$\int_{\mathbf{x}} \mathbf{p}\, d\mathbf{p} = \begin{pmatrix} 0 \\ 0 \\ 0 \end{pmatrix}$$

The preceding definition is not used directly. Rather, it is provided to disambiguate our understanding of what we mean by a particle geometry. Given the above, we now define the following.

Definition 7.3.2. A *particle* is a set $(\mathbf{x},\mathbf{c}) = \{\mathbf{q}+\mathbf{c} : \mathbf{q} \in \mathbf{x}\}$. This corresponds to the geometry $\mathbf{x}$ translated by the vector $\mathbf{c}$.

Next, we formalize the concept of a distribution of particles.

Definition 7.3.3. A *particle distribution* is a pair $(\mathsf{X},\mathfrak{N})$, where X is a set of particle geometries and $\mathfrak{N} : 2^{\mathsf{X}} \to [0,\infty)$, satisfying

- $\mathfrak{N}(\varnothing) = 0$,
- $\mathfrak{N}(\mathsf{A}\cup\mathsf{B}) = \mathfrak{N}(\mathsf{A}) + \mathfrak{N}(\mathsf{B}) - \mathfrak{N}(\mathsf{A}\cap\mathsf{B})$ for all $\mathsf{A},\mathsf{B} \subseteq \mathsf{X}$, and
- $\mathfrak{N}(\mathsf{X})$ is finite.

$\mathfrak{N}(\mathsf{S})$ represents the number of particles per unit volume with geometry $\mathbf{x} \in \mathsf{S} \subseteq \mathsf{X}$.

A medium then consists of particles $(\mathbf{x},\mathbf{c})$ with $\mathbf{x}$ from the distribution $(\mathsf{X},\mathfrak{N})$ and $\mathbf{c}$ distributed uniformly throughout $\mathbb{R}^3$. For a continuous distribution, we then define $\mathfrak{n}(\mathbf{x})\,d\mathbf{x}$ to be the infinitesimal number of particles per unit volume with geometry about $\mathbf{x}$. That is,

$$\mathfrak{N}(\mathsf{S}) = \int_{\mathsf{S}} \mathfrak{n}(\mathbf{x})\,d\mathbf{x}. \tag{7.6}$$

We aim to determine two properties of such a distribution. As we will see, the distance, d, travelled by a ray in the direction $\mathbf{v}$ through a volume of particles from $(\mathsf{X},\mathfrak{N})$, before intercepting a particle, is an exponential random variable with parameter K. We must determine K. Second, the geometry, $\mathbf{x}$, of the particle struck by this ray is also a random variable, the distribution of which must also be determined. It is important to note the distinction between this distribution and other distributions describing the medium, such as the number density, $\mathfrak{n}$, of particles per unit volume. We begin by considering the case where X is a singleton. This is then extended to include discrete particle distributions in which X is finite. Finally, we extend to the continuous case via approximation by discrete particle distributions.

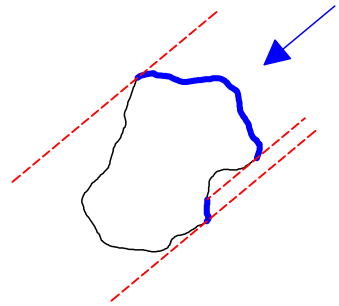

Figure 7.1: The bold blue line indicates the set of points that are exposed by the particle geometry to the indicated vector.

7.3.2 Fixed Particle Distributions

First, however, let us consider a fixed particle distribution. That is, one where $\mathsf{X} = \{\mathbf{x}\}$. In this case, the set function $\mathfrak{N}$ is completely specified by $\mathfrak{N}_0 = \mathfrak{N}(\mathsf{X})$, the total number of particles per unit volume. We require the aid of the following definition.

Definition 7.3.4. Given a particle geometry $\mathbf{x}$, we say that the point $\mathbf{p} \in \mathbf{x}$ is *exposed* to the vector $\mathbf{v}$ if $\mathbf{p}' = \mathbf{p} - t\mathbf{v} \notin \mathbf{x}$ for all $t > 0$.

Consider a ray $r(t) = \mathbf{p} + t\mathbf{v}$ travelling through a medium of particles from $(\mathsf{X}, \mathfrak{N})$. While it is possible, if $\mathbf{x}$ is non-convex and for small t, to have ray-particle intersections involving points on the particle not exposed to $\mathbf{v}$, we neglect this case for the sake of simplicity. In any case, this is not an issue for the SPLITS model as prolate spheroids are convex.

Let $\mathsf{E}_{\mathbf{x},\mathbf{v}}$ be the set of exposed points $\mathbf{q} \in \mathbf{x}$ (Figure 7.1), and consider the region C_t in which a particle $(\mathbf{x}, \mathbf{c})$ satisfying $\mathbf{c} \in \mathsf{C}_t$ would intersect the ray r at $r(t)$. That is,

$$\mathsf{C}_t = \{\mathbf{c} : \mathbf{c} = r(t) - \mathbf{q},\, \mathbf{q} \in \mathsf{E}_{\mathbf{x},\mathbf{v}}\}.$$

Clearly $\mathsf{E}_{\mathbf{x},\mathbf{v}}$ has a projected area (projected onto a plane perpendicular to $\mathbf{v}$) of $G_{\mathbf{v}}$. Since C_t is merely $\mathsf{E}_{\mathbf{x},\mathbf{v}}$ mirrored in the origin (scaled by -1) and translated, it also has a projected area of $G_{\mathbf{v}}$.

Now consider

$$\mathsf{C}_{(0,t_0)} = \bigcup_{0<t<t_0} \mathsf{C}_t$$

corresponding to C_0 swept in the direction of $r(t)$ a distance of t_0. We claim that the volume of $\mathsf{C}_{(0,t_0)}$ is $G_{\mathbf{v}}t_0$. To demonstrate this, we must show that no two vectors $\mathbf{c}_1, \mathbf{c}_2 \in \mathsf{C}_0$ project to the same point on a plane perpendicular to $\mathbf{v}$. That is, we must show that no two vectors $\mathbf{c}_1, \mathbf{c}_2 \in \mathsf{C}_0$ satisfy $\mathbf{c}_2 = \mathbf{c}_1 + t'\mathbf{v}$ for some $t' > 0$. Suppose, on the contrary, that this were the case. Then

$$r(0) - \mathbf{q}_2 = \mathbf{c}_2 = \mathbf{c}_1 + t'\mathbf{v} = r(0) - \mathbf{q}_1 + t'\mathbf{v}.$$

Thus, we would have $\mathbf{q}_2 = \mathbf{q}_1 - t'\mathbf{v}$ with $\mathbf{q}_1, \mathbf{q}_2 \in \mathsf{E}_{\mathbf{x},\mathbf{v}}$. This contradicts Definition 7.3.4. Therefore, the volume of $\mathsf{C}_{(0,t_0)}$ is $G_{\mathbf{v}}t_0$, as claimed.

Given a subset $\mathsf{M} \subset \mathbb{R}^3$ of the medium having volume V, the probability that a given particle $(\mathbf{x}, \mathbf{c})$ satisfies $\mathbf{c} \in \mathsf{C}_{(0,t_0)}$, and thus intersects the $r(t)$ between 0 and t_0, is then $G_{\mathbf{v}}t_0/V$. Since there are $\mathfrak{N}_0$ particles per unit volume, the probability that no particles intersect the ray on the interval $(0, t_0)$, and hence the path length d satisfies $d > t_0$, is then

$$\left(1 - \frac{G_{\mathbf{v}}t_0}{V}\right)^{\mathfrak{N}_0 V}.$$

Allowing M to grow without bound, we see that

$$1 - F_d(t_0) = \Pr(d > t_0) = \lim_{V \to \infty} \left(1 - \frac{G_{\mathbf{v}}t_0}{V}\right)^{\mathfrak{N}_0 V}.$$

Taking the limit [151] and solving for F_d yields

$$F_d(t_0) = 1 - \exp\left(-\mathfrak{N}_0 G_{\mathbf{v}} t_0\right).$$

This has the form of Equation (7.2). Hence, d is an exponentially distributed with parameter $K = \mathfrak{N}_0 G_{\mathbf{v}}$, which we shall call the *geometric attenuation coefficient* of the distribution $(\mathsf{X}, \mathfrak{N})$.

7.3.3 Discrete Particle Distributions

Next, we extend the above to handle a medium consisting of particles having differing geometries.

Definition 7.3.5. A particle distribution $(\mathsf{X}, \mathfrak{N})$ is *discrete* if $|\mathsf{X}|$ is finite, say $\mathsf{X} = \{\mathbf{x}_1, \ldots, \mathbf{x}_m\}$.

Note that, for a discrete particle distribution, $\mathfrak{N}$ is completely specified by $\mathfrak{N}_j = \mathfrak{N}(\{\mathbf{x}_j\})$, the number of particles per unit volume with geometry $\mathbf{x}_j$, for $1 \leq j \leq m$. We may consider the particles of geometry $\mathbf{x}_j$ to form separate fixed distributions $(\{\mathbf{x}_j\}, \mathfrak{N}_j)$ as described in Section 7.3.2. A ray, $\mathbf{v}$, travelling through the medium would reach a particle with geometry $\mathbf{x}_j$ at distance d_j,* where d_j is an exponential random variable with parameter

$$K_j = \mathfrak{N}_j G_{\mathbf{v}}(\mathbf{x}_j). \tag{7.7}$$

This is the geometric attenuation coefficient for particles with geometry $\mathbf{x}_j$. A ray travelling through the combined medium of particles will then reach a particle at a distance $d = \min_j d_j$. The geometry, $\mathbf{x}$, of the intercepted particle would then be $\mathbf{x}_j$ satisfying $d_k > d_j$ for all $k \neq j$. Applying Theorem 7.2.2, it follows that we may equivalently select $\mathbf{x}$ and d independently, with d being exponentially distributed with parameter K and $\mathbf{x} = \mathbf{x}_j$ with probability K_j/K, where

$$K = \sum_j \mathfrak{N}_j G_{\mathbf{v}}(\mathbf{x}_j). \tag{7.8}$$

We call K the geometric extinction coefficient of the discrete particle distribution $(\mathsf{X}, \mathfrak{N})$.

7.3.4 Continuous Particle Distributions

A continuous particle distribution $(\mathsf{X}, \mathfrak{N})$ may be approximated using a discrete distribution, with $\mathfrak{N}_j \approx \mathfrak{n}(\mathbf{x}_j)\, d\mathbf{x}$. As we approximate $(\mathsf{X}, \mathfrak{N})$ using more particle geometries, allowing $d\mathbf{x} \to 0$, we get the following result.

*Note that, whereas in Equation (6.19) j varied over the different types (*i.e.*, mineral compositions) of particles, here j varies over a finite set of particle *geometries*.

Corollary 7.3.6. *Given a particle distribution* $(\mathsf{X}, \mathfrak{N})$*, let* $\mathfrak{n}(\mathbf{x})$ *be defined as in Equation (7.6). Given a ray,* $\mathbf{v}$*, travelling through a medium of particles from* $(\mathsf{X}, \mathfrak{N})$*, define* $G_{\mathbf{v}}(\mathbf{x})$ *as the cross sectional area of* $\mathbf{x}$ *projected onto a plane perpendicular to* $\mathbf{v}$*. Then the path length, d, travelled along* $\mathbf{v}$ *before reaching a particle is an exponential random variable with the parameter, K, given by*

$$K = \int_{\mathsf{X}} \mathfrak{n}(\mathbf{x}) G_{\mathbf{v}}(\mathbf{x})\, d\mathbf{x}. \tag{7.9}$$

Similarly to the discrete case, we call K the geometric attenuation coefficient of $(\mathsf{X}, \mathfrak{N})$*. Furthermore, the geometry* $\mathbf{x}$ *of the particle intercepted by* $\mathbf{v}$ *is independent of d and* $f_{\mathbf{x}}$ *is given by*

$$f_{\mathbf{x}}\left(\mathbf{x}'\right) = \frac{1}{K} \mathfrak{n}\left(\mathbf{x}'\right) G_{\mathbf{v}}\left(\mathbf{x}'\right). \tag{7.10}$$

7.3.5 Separability

A particle's geometry may depend on multiple variables, and a particle distribution may consist of particle geometries resulting from varying each of those variables. We would like to determine when and how we may handle each of these variables independently of one another. We begin by defining what we mean by a separable function and a separable distribution.

Definition 7.3.7. A function $f : \mathsf{A} \times \mathsf{B} \to \mathbb{R}$ is called *separable** [86] if there are two functions $f_1 : \mathsf{A} \to \mathbb{R}$ and $f_2 : \mathsf{B} \to \mathbb{R}$ such that $f(a,b) = f_1(a) f_2(b)$ for all $a \in \mathsf{A}$ and $b \in \mathsf{B}$.

Definition 7.3.8. We call a particle distribution $(\mathsf{X}, \mathfrak{N})$ *separable* if $\mathsf{X} = \mathsf{A} \times \mathsf{B}$ and if $\mathfrak{n}$ and $G_{\mathbf{v}}$ are both separable.

Suppose $(\mathsf{X} = \mathsf{A} \times \mathsf{B}, \mathfrak{N})$ is separable and let $\mathfrak{n}(\mathbf{a}, \mathbf{b}) = \mathfrak{n}_1(\mathbf{a}) \mathfrak{n}_2(\mathbf{b})$ and $G_{\mathbf{v}}(\mathbf{a}, \mathbf{b}) = G_1(\mathbf{a}) G_2(\mathbf{b})$

*Strictly speaking, such a function is called *product* separable [86]. A *sum* separable function is one that can be decomposed into a sum of univariate functions [86]. However, as we shall not require the latter, we shall use the term *separable* to mean product separable.

for each $\mathbf{x} = (\mathbf{a}, \mathbf{b}) \in \mathsf{X}$. Then

$$\begin{aligned} K &= \int_{\mathsf{X}} \mathfrak{n}(\mathbf{a}, \mathbf{b}) G_{\mathbf{v}}(\mathbf{a}, \mathbf{b})\, d\mathbf{x} \\ &= \int_{\mathsf{A}} \int_{\mathsf{B}} \mathfrak{n}_1(\mathbf{a}) \mathfrak{n}_2(\mathbf{b}) G_1(\mathbf{a}) G_2(\mathbf{b})\, d\mathbf{b}\, d\mathbf{a} \\ &= \int_{\mathsf{A}} \mathfrak{n}_1(\mathbf{a}) G_1(\mathbf{a})\, d\mathbf{a} \int_{\mathsf{B}} \mathfrak{n}_2(\mathbf{b}) G_2(\mathbf{b})\, d\mathbf{b}, \end{aligned} \tag{7.11}$$

which may now be expressed as $K = K_1 K_2$. Furthermore, the probability density, $f_{\mathbf{a}}$, for $\mathbf{a}$, is

$$\begin{aligned} f_{\mathbf{a}}\left(\mathbf{a}'\right) &= \int_{\mathsf{B}} f_x\left(\mathbf{a}', \mathbf{b}'\right)\, d\mathbf{b}' \\ &= \frac{1}{K} \int_{\mathsf{B}} \mathfrak{n}\left(\mathbf{a}', \mathbf{b}'\right) G_{\mathbf{v}}\left(\mathbf{a}', \mathbf{b}'\right)\, d\mathbf{b}' \\ &= \frac{1}{K} \mathfrak{n}_1\left(\mathbf{a}'\right) G_1\left(\mathbf{a}'\right) \int_{\mathsf{B}} \mathfrak{n}_2\left(\mathbf{b}'\right) G_2\left(\mathbf{b}'\right)\, d\mathbf{b}' \\ &= \frac{K_2}{K} \mathfrak{n}_1\left(\mathbf{a}'\right) G_1\left(\mathbf{a}'\right) \\ &= \frac{1}{K_1} \mathfrak{n}_1\left(\mathbf{a}'\right) G_1\left(\mathbf{a}'\right). \end{aligned} \tag{7.12}$$

The probability density function, $f_{\mathbf{b}}$, for $\mathbf{b}$ reduces similarly. In practical terms, this means that if the particle geometry depends on multiple variables, $\mathbf{x}$ may be selected by selecting each of those variables independently, provided that the distribution is separable. Also, the geometric attenuation coefficient may be computed as a product of terms each depending on only one variable.

7.3.6 Separating Size and Shape

Consider a particle geometry given by $\mathbf{x} = (s, \mathbf{y}) \in \mathsf{X} = \mathbb{R}^+ \times \mathsf{Y}$, where $s \in \mathbb{R}^+$ is a scaling factor representing the *size* of the particle and additional parameters $\mathbf{y} \in \mathsf{Y}$ describe the *shape* of the particle. The geometric cross section of $\mathbf{x}$ with respect to $\mathbf{v}$ is then

$$G_{\mathbf{v}}(s, \mathbf{y}) = s^2 G_{\mathbf{v}}(1, \mathbf{y}). \tag{7.13}$$

If $\mathfrak{n}$ is then defined using separate shape and size distributions, then the particle distribution is separable.

In particular, suppose the size distribution is expressed as the fraction, $\mathfrak{F}_{\mathfrak{v}}(s_1, s_2)$, of volume occupied by particles with sizes ranging from s_1 to s_2. Define $\mathfrak{f}_{\mathfrak{v}}(s)$ by

$$\mathfrak{F}_{\mathfrak{v}}(s_1, s_2) = \int_{s_1}^{s_2} \mathfrak{f}_{\mathfrak{v}}(s)\, ds, \tag{7.14}$$

with $\mathfrak{F}_{\mathfrak{v}}(s_{min}, s_{max}) = \nu \in [0,1]$ being the total fraction of volume occupied by all particles. In this case, $\mathfrak{f}_{\mathfrak{v}}(s)\, ds$ is the infinitesimal fraction of volume occupied by particles of size s. Additionally, let $\mathfrak{f}_{\mathfrak{n}}(\mathbf{y})\, d\mathbf{y}$ be the infinitesimal (number) fraction of particles with shape $\mathbf{y}$. We then have

$$\mathfrak{n}(s, \mathbf{y}) = \frac{\mathfrak{f}_{\mathfrak{v}}(s)\mathfrak{f}_{\mathfrak{n}}(\mathbf{y})}{V(s, \mathbf{y})},$$

where $V(s, \mathbf{y})$ is the volume of a particle with geometry $(s, \mathbf{y})$. Since $V(s, \mathbf{y}) = s^3 V(1, \mathbf{y})$, $\mathfrak{n}$ is separable and $\mathfrak{n}(s, \mathbf{y}) = \mathfrak{n}_1(s)\mathfrak{n}_2(\mathbf{y})$, with

$$\mathfrak{n}_1(s) = \mathfrak{f}_{\mathfrak{v}}(s) s^{-3}, \text{ and} \tag{7.15}$$

$$\mathfrak{n}_2(\mathbf{y}) = \frac{\mathfrak{f}_{\mathfrak{n}}(\mathbf{y})}{V(1, \mathbf{y})}. \tag{7.16}$$

Substituting Equation (7.13) and the preceding into Equations (7.11) and (7.12) yields

$$K_1 = \int_{s_{min}}^{s_{max}} \mathfrak{f}_{\mathfrak{v}}(s) s^{-1}\, ds, \tag{7.17}$$

$$K_2 = \int_{\mathsf{Y}} \mathfrak{f}_{\mathfrak{n}}(\mathbf{y}) \frac{G_{\mathbf{v}}(1, \mathbf{y})}{V(1, \mathbf{y})}\, d\mathbf{y}, \tag{7.18}$$

$$f_s\left(s'\right) = \frac{1}{K_1} \mathfrak{f}_{\mathfrak{v}}\left(s'\right) s'^{-1}, \text{ and} \tag{7.19}$$

$$f_{\mathbf{y}}\left(\mathbf{y}'\right) = \frac{1}{K_2} \mathfrak{f}_{\mathfrak{n}}\left(\mathbf{y}'\right) \frac{G_{\mathbf{v}}\left(1, \mathbf{y}'\right)}{V(1, \mathbf{y}')}. \tag{7.20}$$

7.3.7 Orientation

For non-spherical particles, orientation becomes important. From Definition 7.3.1, it follows that particles with the same "shape" but different orientations have differing geometry. We wish to consider particles with uniform random orientation. In this case, $\mathbf{x} = (s, \mathbf{z}, \boldsymbol{\omega}) \in \mathsf{X} = \mathbb{R}^+ \times \mathsf{Z} \times \mathfrak{S}$.* However, often this particle distribution is not separable, since $G_{\mathbf{v}}(1, \mathbf{z}, \boldsymbol{\omega})$ may not be separable. For instance, this is the case for prolate spheroids with sphericity $\Psi \in \mathsf{Z} = (0, 1)$, as used in the SPLITS model. For simplicity, instead of treating orientation and shape jointly, we approximate $G_{\mathbf{v}}(1, \mathbf{z}, \boldsymbol{\omega})$ with its mean over all orientations,

$$\overline{G}(1, \mathbf{z}) = \frac{1}{4\pi} \int_{\mathfrak{S}} G_{\mathbf{v}}(1, \mathbf{z}, \omega)\, d\omega. \tag{7.21}$$

Now we may consider the distribution separable, with

$$G_{\mathbf{v}}(s, \mathbf{z}, \boldsymbol{\omega}) \approx s^2 \overline{G}(1, \mathbf{z}),$$

and

$$\mathfrak{n}(s, \mathbf{z}, \boldsymbol{\omega}) = \frac{1}{4\pi} \mathfrak{n}_1(s) \mathfrak{n}_2(\mathbf{z}).$$

Then $K = K_1 K_2 K_3$ with K_1 given by Equation (7.17), K_2 given by

$$K_2 = \int_{\mathsf{Z}} \mathfrak{f}_{\mathfrak{n}}(\mathbf{z}) \frac{\overline{G}(1, \mathbf{z})}{V(1, \mathbf{z})}\, d\mathbf{z}, \tag{7.22}$$

and

$$K_3 = \int_{\mathfrak{S}} \frac{1}{4\pi}\, d\boldsymbol{\omega} = 1.$$

*Strictly, the domain for orientation should be $\mathfrak{S} \times \mathfrak{C}$, to include all three degrees of freedom: yaw, pitch, and *roll*. However, $G_{\mathbf{v}}$ does not vary with the latter, and may therefore be ignored.

The probability density function, f_s, for the particle size, is given by Equation (7.19), $f_{\mathbf{z}}$ is given by

$$f_{\mathbf{z}}\left(\mathbf{z}'\right) = \frac{1}{K_2}\mathfrak{f}_{\mathfrak{n}}\left(\mathbf{z}'\right)\frac{\overline{G}(1,\mathbf{z}')}{V(1,\mathbf{z}')}, \tag{7.23}$$

and $f_{\omega}(\omega') = 1/4\pi$.

7.3.8 Convex Particles

If the particles are convex, $\overline{G}(1,\mathbf{z})$ may be further reduced. We approximate the particle shape $\mathbf{z}$ using a convex polyhedron, with A_j being the area of the jth face and $\mathbf{n}_j$ the jth face normal. Recall that $\mathbf{v}$ is the ray travelling through the medium. Each face with $\mathbf{n}_j \cdot \mathbf{v} < 0$ contributes $A_j(\mathbf{n}_j \cdot \mathbf{v})$ to $G_{\mathbf{v}}$. However, since $G_{-\mathbf{v}} = G_{\mathbf{v}}$, we may halve the contributions from all faces, yielding

$$G_{\mathbf{v}} = \frac{1}{2}\sum_j A_j \left|\mathbf{n}_j \cdot \mathbf{v}\right|. \tag{7.24}$$

We may let $\mathbf{v} = \omega$ without loss of generality. Equation (7.21) then becomes

$$\begin{aligned}\overline{G} &= \frac{1}{8\pi}\int_{\mathfrak{S}}\sum_j A_j \left|\mathbf{n}_j \cdot \omega\right| d\omega \\ &= \frac{1}{8\pi}\sum_j A_j \int_{\mathfrak{S}} \left|\mathbf{n}_j \cdot \omega\right| d\omega.\end{aligned} \tag{7.25}$$

To evaluate $\int_{\mathfrak{S}} |\mathbf{n}_j \cdot \omega| d\omega$, we specify $\omega = (\theta_j, \phi_j)$ using spherical coordinates with respect to $\mathbf{n}_j$. This yields

$$\begin{aligned}&\int_0^{2\pi}\int_0^{\pi} \left|\cos\theta_j\right| \sin\theta_j \, d\theta_j \, d\phi_j \\ &= 2\pi\left(\int_0^{\frac{\pi}{2}} \cos\theta_j \sin\theta_j \, d\theta_j + \int_{\frac{\pi}{2}}^{\pi} -\cos\theta_j \sin\theta_j \, d\theta_j\right) \\ &= 4\pi\int_0^{\frac{\pi}{2}} \cos\theta_j \sin\theta_j \, d\theta_j \\ &= 2\pi\int_0^{\frac{\pi}{2}} \sin 2\theta_j \, d\theta_j\end{aligned}$$

$$= 2\pi\left(-\frac{1}{2}\cos\pi + \frac{1}{2}\cos 0\right)$$
$$= 2\pi.$$

Substituting back into (7.25) yields

$$\overline{G} = \frac{1}{4}\sum_j A_j = \frac{1}{4}A_S, \tag{7.26}$$

where A_S is the surface area. To verify, consider a simple distribution consisting entirely of spheres with radius r. In this case, $\overline{G} = \pi r^2$ and $A_S = 4\pi r^2$, satisfying Equation (7.26). Equations (7.22) and (7.23) are now reduced, respectively, to

$$K_2 = \frac{1}{4}\int_{\mathsf{Z}} \mathfrak{f}_{\mathfrak{n}}(\mathbf{z}) A_V(1,\mathbf{z})\, d\mathbf{z}, \tag{7.27}$$

and

$$f_{\mathbf{z}}\left(\mathbf{z}'\right) = \frac{1}{4K_2}\mathfrak{f}_{\mathfrak{n}}\left(\mathbf{z}'\right) A_V(1,\mathbf{z}), \tag{7.28}$$

where $A_V(1,\mathbf{z}) = A_S(1,\mathbf{z})/V(1,\mathbf{z})$ is the *surface area to volume ratio* of a particle of unit size and shape $\mathbf{z}$.

7.4 Concrete Particle Distributions

Now that we have a framework for particle distributions in the abstract sense, we are ready to tackle concrete distributions.

7.4.1 The Particle Distribution used in SPLITS

In the SPLITS model, particles are modeled as randomly oriented prolate spheroids with normally distributed sphericity and the major axis distributed according to a piecewise logarithmic normal

distribution function (Section 6.2.6). This distribution is separable* (Section 7.3.5), and therefore we may select the particle size and sphericity independently and the geometric attenuation coefficient may be decomposed into parts $K = K_1 K_2$.

The particle size distribution is expressed as the fraction,

$$\mathfrak{F}_m(s_1, s_2) = \int_{s_1}^{s_2} \mathfrak{f}_g(s) s^{-1}\, ds,$$

of the mass contained within particles with sizes between s_1 and s_2, where $\mathfrak{f}_g$ is a lognormal distribution function given by Equation (6.17). As stated in Section 6.2.6, we assume that density does not vary with particle size and thus $\mathfrak{F}_\mathfrak{v}/\nu = \mathfrak{F}_m$. From Equation (7.14), we see that

$$\mathfrak{f}_\mathfrak{v}(s) = \frac{\nu \mathfrak{f}_g(s) s^{-1}}{\int_{s_{min}}^{s_{max}} \mathfrak{f}_g(s) s^{-1}\, ds}. \tag{7.29}$$

Substituting into Equations (7.17) and (7.19) yields

$$K_1 = \nu \frac{\int_{s_{min}}^{s_{max}} \mathfrak{f}_g(s) s^{-2}\, ds}{\int_{s_{min}}^{s_{max}} \mathfrak{f}_g(s) s^{-1}\, ds}, \text{ and} \tag{7.30}$$

$$f_s\left(s'\right) = \frac{1}{K_1} \mathfrak{f}_g\left(s'\right) s'^{-2}. \tag{7.31}$$

The shape of the particle is described by a single parameter, Ψ, the sphericity (Equation (6.1)). The (infinitesimal) fraction of particles with sphericity Ψ is given by

$$\mathfrak{f}_\mathfrak{n}(\Psi) = \frac{\Phi'(\overline{\Psi}, \sigma_\Psi^2)(\Psi)}{\int_{\Psi_{min}}^{\Psi_{max}} \Phi'(\overline{\Psi}, \sigma_\Psi^2)(\Psi)\, d\Psi}, \tag{7.32}$$

where $\Phi'(\overline{x}, \sigma^2) : \mathbb{R} \to \mathbb{R}^+$ is the normal probability density function with mean $\overline{x}$ and variance σ^2 [116]. For a prolate spheroid with unit size,

$$A_V(1, \Psi) = 3\left(1 + \frac{\sin^{-1}\sqrt{1-\Psi^4}}{\Psi^2\sqrt{1-\Psi^4}}\right). \tag{7.33}$$

*This distribution is separable assuming we make some approximations. See Section 7.3.7 for details.

Substituting the preceding into Equations (7.27) and (7.28) yields

$$K_2 = \frac{\int_{\Psi_{min}}^{\Psi_{max}} \Phi'(\overline{\Psi}, \sigma_\Psi^2)(\Psi) A_V(1,\Psi)\, d\Psi}{4\int_{\Psi_{min}}^{\Psi_{max}} \Phi'(\overline{\Psi}, \sigma_\Psi^2)(\Psi)\, d\Psi}, \text{ and} \tag{7.34}$$

$$f_\Psi\left(\Psi'\right) = \frac{1}{4K_2}\Phi'(\overline{\Psi}, \sigma_\Psi^2)(\Psi') A_V(1,\Psi). \tag{7.35}$$

7.4.2 Other Particle Distributions

Other particle distributions may be used by substituting the appropriate formulae into the equations derived earlier in this chapter. For distributions consisting of particles with a fixed orientation, one must substitute, into Equations (7.17) through (7.20), the formulae for the geometric cross section, $G_{\mathbf{v}}$, and the volume, V, of a particle with unit size. These formulae are provided in Table 7.2 for selected shapes. For a distribution of particles with uniform random orientation, one may substitute Equations (7.22) and (7.23) for Equations (7.18) and (7.20) respectively. This requires the mean geometric cross section, $\overline{G}$. In particular, if the particles are convex, then $\overline{G} = A_S/4$, and Equations (7.22) and (7.23) reduce, respectively, to Equations (7.27) and (7.28), involving the surface area to volume ratio, A_V. These formulae are provided, for selected shapes, in Table 7.1.

Particle Shape	**Surface Area** (A_S)	**Volume** (V)	**Surface Area to Volume Ratio** ($A_V = A_S/V$)
spheres • radius r	$4\pi r^2$	$\frac{4}{3}\pi r^3$	$\frac{3}{r}$
oblate spheroids • major semiaxis of length a • minor semiaxis of length c • eccentricity e (Equation (A.7))	$2\pi a^2 + \pi\frac{c^2}{e}\log\left(\frac{1+e}{1-e}\right)$	$\frac{4}{3}\pi a^2 c$	$\frac{3}{2c} + \frac{3c}{4a^2 e}\log\left(\frac{1+e}{1-e}\right)$
prolate spheroids • minor semiaxis of length a • major semiaxis of length c • eccentricity e (Equation (A.5))	$2\pi a^2 + 2\pi\frac{ac}{e}\sin^{-1} e$	$\frac{4}{3}\pi a^2 c$	$\frac{3}{2a}\left(\frac{a}{c} + \frac{\sin^{-1} e}{e}\right)$
cubes • side length a	$6a^2$	a^3	$\frac{6}{a}$
boxes • side lengths a, b, and c	$2(ab + ac + bc)$	abc	$2\left(\frac{1}{a} + \frac{1}{b} + \frac{1}{c}\right)$

Table 7.1: Formulae used to compute geometric attenuation coefficients for particle distributions with fixed sized, randomly oriented shapes. Derivations for the surface areas of the prolate and oblate ellipsoids are given in Appendix A. All other formulae are provided by Zwillinger [151].

Particle Shape	**Geometric Cross Section** ($G_{\mathbf{v}}$)	**Volume** (V)	**Cross Sectional Area per unit Volume** ($G_{\mathbf{v}}/V$)
spheroids • semiaxes parallel to x and y axes of length a • semiaxis parallel to z axis of length c • eccentricity e (Equations (A.5) and (A.7))	$\pi a\sqrt{a^2\cos^2\theta + c^2\sin^2\theta}$	$\frac{4}{3}\pi a^2 c$	$\frac{3}{4ac}\sqrt{a^2\cos^2\theta + c^2\sin^2\theta}$
cubes • side length a	$a^2(\lvert\alpha'\rvert + \lvert\beta'\rvert + \lvert\gamma'\rvert)$	a^3	$\frac{1}{a}(\lvert\alpha'\rvert + \lvert\beta'\rvert + \lvert\gamma'\rvert)$
boxes • side lengths a, b, and c along the x, y, and z axes respectively	$ab\lvert\gamma'\rvert + ac\lvert\beta'\rvert + bc\lvert\alpha'\rvert$	abc	$\frac{\lvert\alpha'\rvert}{a} + \frac{\lvert\beta'\rvert}{b} + \frac{\lvert\gamma'\rvert}{c}$

Table 7.2: Formulae used to compute geometric attenuation coefficients for particle distributions with fixed size and orientation. The parameters α', β', and γ' are the incident direction cosines with respect to the particle's local x, y, and z axes (respectively). The parameter $\theta = \cos^{-1}\gamma'$ is the incident angle with respect to the particle's local z axis. The geometrical cross section for a spheroid is provided by Asano [2]. The remaining cross sections are special cases of Equation (7.24). All formulae for volumes provided by Zwillinger [151].

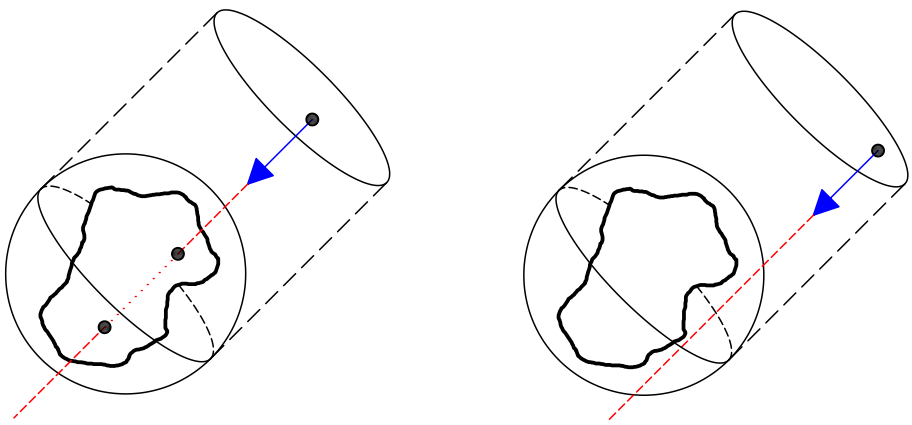

Figure 7.2: Rays are cast toward the bounding sphere of a particle to determine its cross sectional area using Monte Carlo [46] techniques. *Left*: The ray hits intersects the particle. *Right*: The ray misses the particle.

7.5 Computing the Traits of a Particle using Monte Carlo Methods

7.5.1 Geometric Cross Section

If the geometric cross section of a particle cannot be determined analytically, it may be computed using Monte Carlo techniques provided that bounding spheres can be generated and that ray-particle intersections are supported (which is already required by the SPLITS model). To compute the geometric cross section, $G_{\mathbf{v}}$ from a given direction, $\mathbf{v}$, we first compute a bounding sphere for the particle. A ray is then cast in given direction toward the sphere. The origin of this ray is randomly selected from within a disc perpendicular to $\mathbf{v}$, as depicted in Figure 7.2. We then determine if the ray intersects the particle. This process is repeated N times and the number, n, of times an intersection occurs is tracked. The geometric cross section is then estimated as

$$G_{\mathbf{v}} \approx \frac{n}{N}\pi r^2, \tag{7.36}$$

where r is the radius of the bounding sphere. The mean geometric cross section, $\overline{G}$, may be computed by randomizing $\mathbf{v}$.

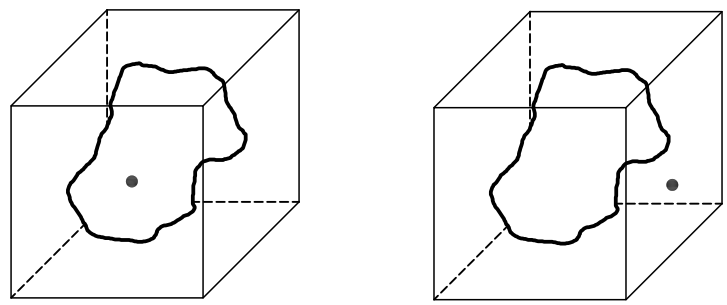

Figure 7.3: Points are selected randomly from within the bounding box of a particle to compute its volume using Monte Carlo [46] techniques. *Left*: The point lies within the particle. *Right*: The point is outside the particle.

7.5.2 Volume

The volume of a particle may be computed in a similar manner provided that bounding boxes* can be generated and provided that the particle supports point-classification (*i.e.*, we can determine if a given point is inside or outside the particle). To do this, we compute a bounding box. A random point, **p**, is then selected uniformly from within the bounding box and we determine whether or not **p** lies inside the particle, as shown in Figure 7.3. After repeating this process N times, the mean particle volume is estimated by

$$V \approx \frac{n}{N} V_{bb}, \tag{7.37}$$

where n is the number of times the randomly generated point lay within the generated particle, and V_{bb} is the volume of the bounding box.

*Another type of bounding shape, of known volume, may be substituted if we can generate a point uniformly at random from within that shape.

Chapter 8

Evaluation

To evaluate the SPLITS model objectively, it is necessary to perform comparisons with measured data directly, so that the results are not confounded by the complexities of a rendering framework [42]. Thus, comparisons were made between measured data [115] and results obtained from the model using virtual goniophotometric [72] and virtual spectrophotometric [9] methods. These comparisons are made in two manners. First, we directly compare the output from the model to measured curves. Additionally, we demonstrate the effects caused by varying individual parameters to show that the resulting changes are in agreement with what is reported in the literature. We also compare the spatial (BRDF) response from the model to qualitative descriptions found in the literature. Additionally, images are presented in this chapter serve to illustrate the colours corresponding to spectral responses obtained from the model, and to demonstrate potential rendering applications.

8.1 Data Availability

Reflectance data for sand covering the visible region and tied to the corresponding characterization data is scarce. There are a few relevant databases available. The United States Geological Survey (USGS) digital spectral library [22] has reflectance curves for several natural and man made materials, including several mineral specimens. This data covers the region of the spectrum from 0.2

to 3.0 μm. However, only one commercially produced sand sample is among these. The ASTER spectral library, which includes data from spectral libraries from John Hopkins University (JHU), the Jet Propulsion Laboratory (JPL) [44], and the aforementioned USGS, also contains reflectance data for many natural and man made materials. Curves for some of these specimens cover the visible region of the spectrum while other curves are limited to the infrared. However, while there are measurements from many soil samples in the ASTER spectral library, few of them are sand and the associated characterization data is limited. Stoner *et al.* [134] provide spectral reflectance plots for various soils, including several sand samples. They also provide the associated characterization data for each sample. However, their data is primarily for the infrared region, and only covers the portion of the visible region of the spectrum beyond 520 nm. This data set is available in tabular format as part of the First ISLSCP Field Experiment (FIFE) [54, 135]. Spectral reflectance data for sands and other granular materials are also provided by the U.S. Army Topographic Engineering Center (TEC) [115]. These data cover a wide range of sands, from desert dune sands to beach sands. The database, however, is lacking the associated characterization data.

8.2 Comparisons with Measured Data

Because the TEC database [115] contains a wide variety of sand samples and since this data covers the entire visible region of the spectrum, this data was chosen for comparison with the SPLITS model. Due to the lack of characterization data, however, precise quantitative comparisons are not feasible. Instead, the parameters were selected from within acceptable ranges (Chapter 5 and Table 6.1) as reported in the literature to attempt to obtain a good match between the measured and modeled curves. This allows us to demonstrate qualitative agreement with measured data, as well as to show that reflectance curves of actual sands are reproducible using the SPLITS model. Four samples were selected from the TEC database [115]: two dune sands, one from Australia (TEC #10019201), and one from Saudi Arabia (TEC #13j9823), a magnetite rich beach sand from central Peru (TEC #10039240), and a sample from a dike outcrop in San Bernardino county, Cali-

fornia (TEC #19au9815).

8.2.1 Measurement Setup

In the experiments performed by Rinker *et al.* [115], reflected radiance is collected from the normal direction and compared to the reflected radiance of a reference white. Based on the measurement setup as outlined by Rinker *et al.* [115], we inferred that the illumination geometry may be appropriately represented using a hemispherical light source. The data provided is therefore in the form of a hemispherical-directional reflectance factor [95]. From a practical perspective, this is a rather difficult measurement to emulate directly using virtual spectrophotometric methods, as it requires collecting reflected rays at a point. One could instead measure a hemispherical-conical reflectance using a small collection cone. However, as most reflected rays would not be reflected in the direction of this small cone, this would require too many rays to be practical. This is especially true if we intend to run this simulation with several combinations of parameters. Fortunately, however, the hemispherical-directional reflectance factor is mathematically equivalent to the directional-hemispherical reflectance [95], which may be simulated easily by casting rays from normal incidence and collecting all rays reflected into the upper hemisphere.

8.2.2 Results of Comparisons

Figure 8.1 shows comparisons between the reflectance curves of these samples and the corresponding curves simulated using SPLITS. The corresponding parameters, along with root-mean-square (RMS) errors, are provided in Table 8.1. According to Jacquemoud *et al.* [64], an RMS error smaller than 0.03 constitutes a good spectral reconstruction. As shown in Table 8.1, all of the RMS errors fall within this bound. Generated images for each of the sand samples are depicted in Figure 8.2. The sand grain pattern was extracted from a photograph and the spectral responses were provided by the SPLITS model. The degree of saturation, $\mathcal{S}$, was also varied from $\mathcal{S} = 0$ to $\mathcal{S} = 1$ within the image to show the darkening effect simulated by the model.

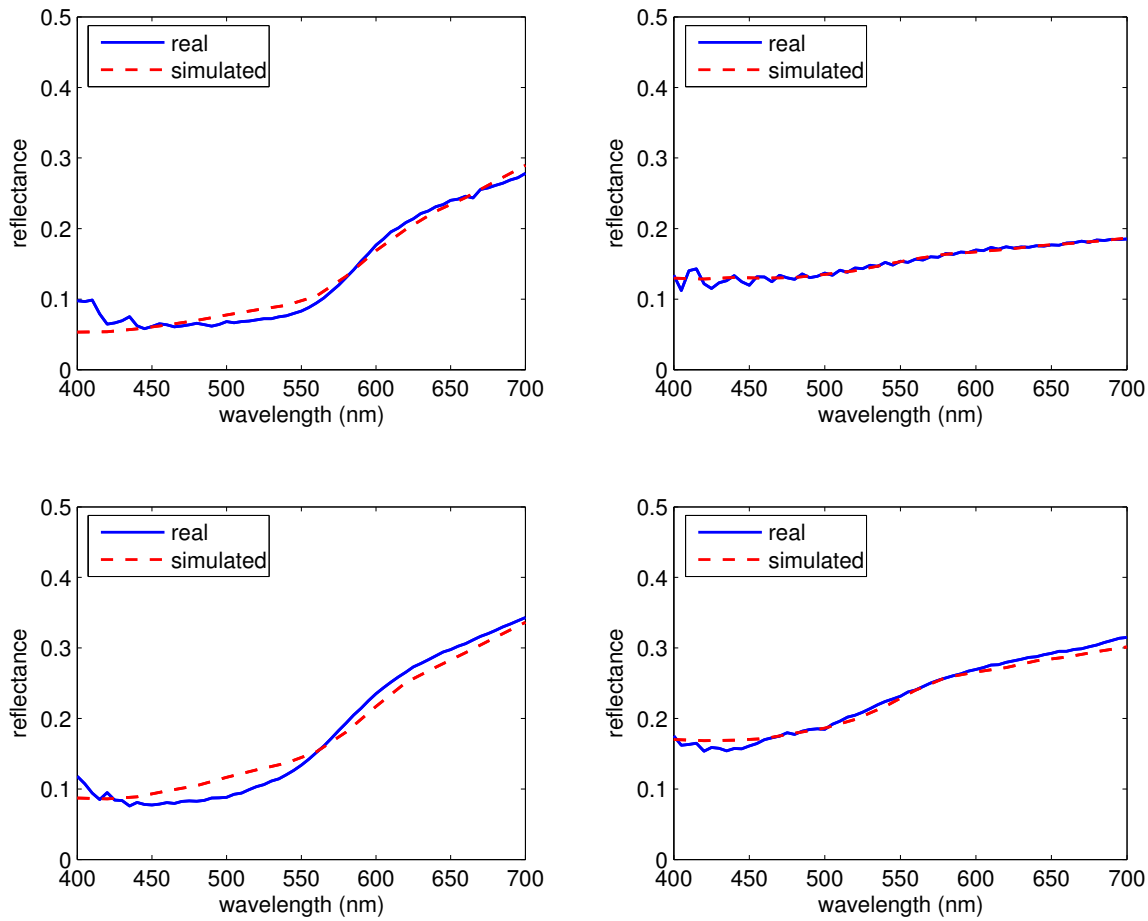

Figure 8.1: Comparisons between real and simulated sand. The solid line indicates the reflectance of the sand sample. The dashed line indicates the modeled reflectance. The parameters used and corresponding RMS errors are provided in Table 8.1. *Top Left*: TEC #10019201, *Top Right*: TEC #10039240, *Bottom Left*: TEC #13j9823, *Bottom Right*: TEC #19au9815.

TEC #	ϑ_{hg}	r_{hg}	ϑ_m	ζ_1	ζ_2	ζ_3	μ'_p	μ'_m	μ'_c	**RMSE**
10019201	0.01	0.738	0.00	0.000	0.150	0.850	0.00	1.00	0.00	0.0138
10039240	0.05	0.359	0.00	0.000	0.150	0.850	0.50	0.00	0.50	0.0047
13j9823	0.01	0.498	0.17	0.000	0.072	0.928	0.00	1.00	0.00	0.0166
19au9815	0.05	0.000	0.00	0.000	0.150	0.850	0.50	0.00	0.50	0.0072

Table 8.1: The parameters used in the SPLITS model for each of the four sand samples, and the root-mean-square error (RMSE) between the actual and simulated reflectances. An RMSE smaller than 0.03 indicates a good spectral reconstruction [64].

Figure 8.2: Images showing variation of sand colour with moisture as predicted by the model. The degree of saturation varies from $\mathcal{S} = 0$ at the top of each image to $\mathcal{S} = 1$ at the bottom. From left to right, the samples are TEC #10019201, TEC #10039240, TEC #13j9823, and TEC #19au9815.

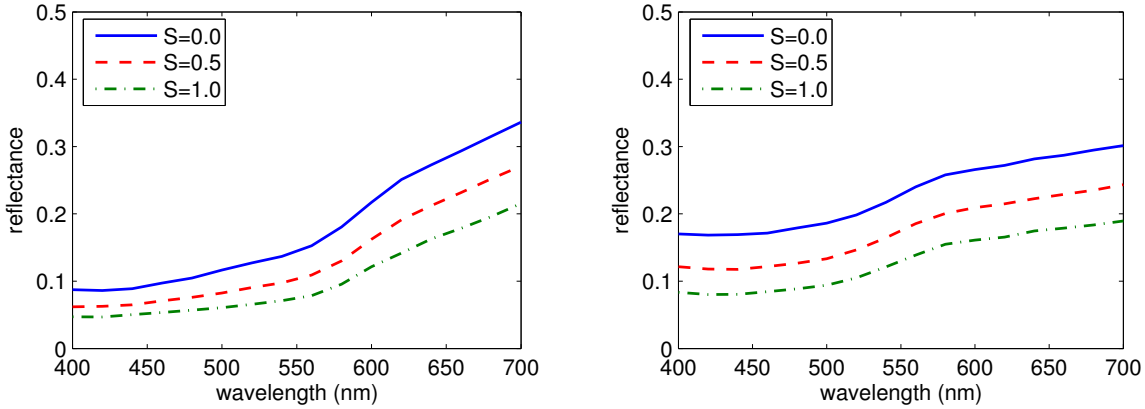

Figure 8.3: Spectral reflectance curves predicted by the SPLITS model for two of the TEC sand samples, varying the degree of saturation, $\mathcal{S}$. *Left*: TEC #13j9823, *Right*: TEC #19au9815.

8.3 Qualitative Characteristics

To show that the SPLITS model qualitatively behaves like sand, we have also conducted simulations varying individual parameters. The variation in the spectral responses resulting from changes to these parameters are shown in Figure 8.4. As expected [11], increasing the iron oxide concentration lowers the reflectance. Note also the shift in reflectance toward the red end of the spectrum when goethite is replaced with hematite (*i.e.*, r_{hg} is increased), as confirmed in the literature [28, 138]. Also, as the particle size was decreased, the reflectance predicted by the model increased, in agreement with the literature [11, 145]. The resulting variation in colour is depicted in Figure 8.5. Additionally, the degree of saturation varied between $\mathcal{S} = 0$ and $\mathcal{S} = 1$ for the four TEC sand samples. The darkening effect, reported in the literature [11, 81], is reflected in the SPLITS model. Simulated

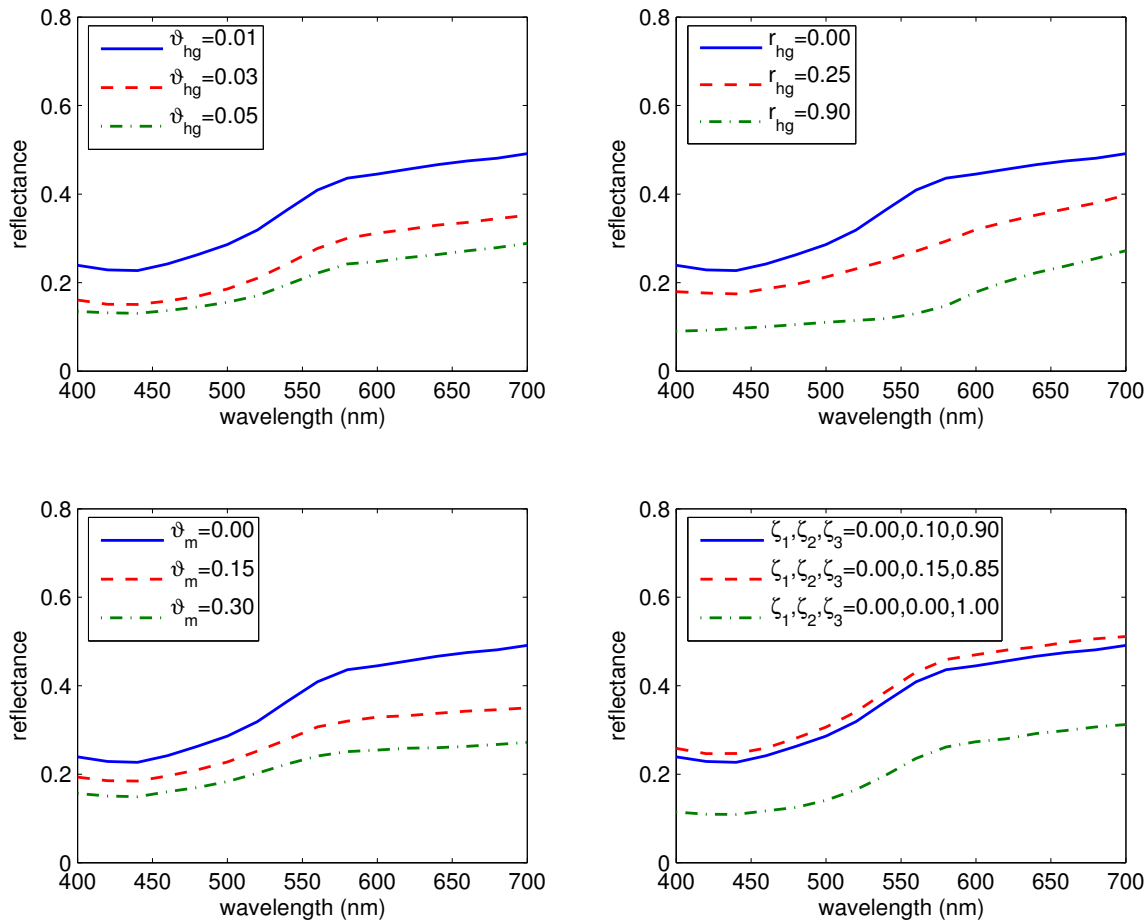

Figure 8.4: Qualitative behaviour of simulated sand. The solid line in each plot indicates the spectral response from the SPLITS model with $\vartheta_{hg} = 0.01$, $r_{hg} = 0.00$, $\vartheta_m = 0.00$, $\zeta_1 = 0.00$, $\zeta_2 = 0.10$, $\zeta_3 = 0.90$, and $\mu'_p = \mu'_m = \mu'_c = 1/3$. *Top Left*: Varying ϑ_{hg}, *Top Right*: Varying r_{hg}, *Bottom Left*: Varying ϑ_m, *Bottom Right*: Varying the texture (ζ_1,ζ_2,ζ_3).

Figure 8.5: Images showing variation of sand colour as various parameters are changed. The image on the left (base image) corresponds to the solid lines in Figure 8.4. The remaining images correspond to the spectral responses from the SPLITS model with the same parameters as in the base image except, from left to right, $\vartheta_{hg} = 0.05$, $r_{hg} = 0.90$, $\vartheta_m = 0.30$, $\zeta_3 = 1.0$.

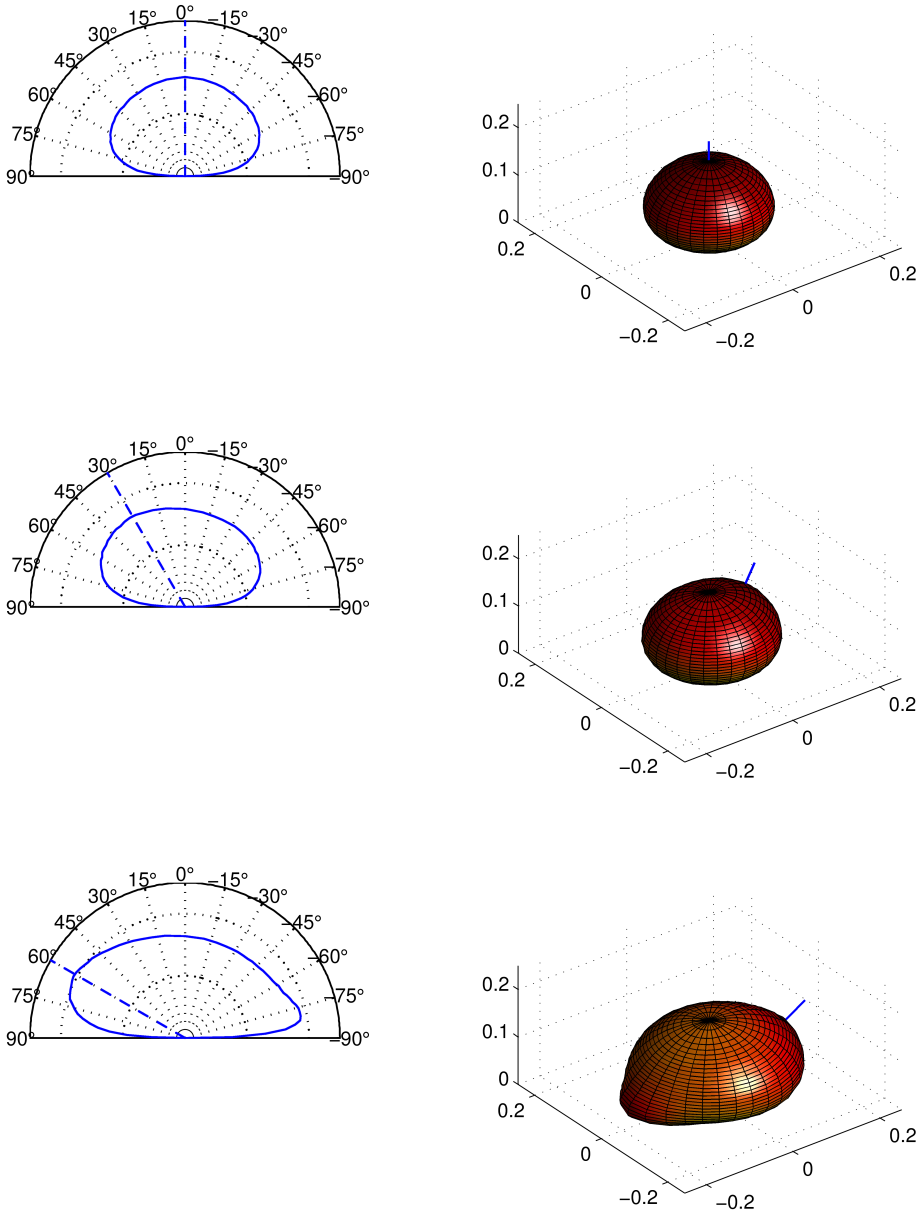

Figure 8.6: BRDF of simulated sand. Profiles along the principal plane are shown on the left (the dashed line indicates the incident direction). Three dimensional plots of the BRDF are shown on the right. *Top*: Normal incidence, *Middle*: For light incident 30° from the normal, *Bottom*: For light incident 60° from the normal.

Figure 8.7: Images demonstrating potential rendering applications of the SPLITS model to provide the spectral response for sands in various scenes.*

reflectance curves for two of these samples are given in Figure 8.3.

A scattering simulation using SPLITS was also conducted to show the spatial distribution predicted by the model. This is shown in Figure 8.6. While the predicted BRDF is diffuse, there is forward scattering and retro-reflection. This is in agreement with the literature (Section 2.2).

8.4 Images

In addition to Figures 8.2 and 8.5, which show the colours associated with the spectral responses obtained from the SPLITS model, spectral responses from the model were also applied to sand in various desert scenes, depicted in Figure 8.7. These images demonstrate potential rendering applications for the SPLITS model.

*Figure 8.7 (*Right*) is based on a photograph courtesy of Miles Hunter.

Chapter 9

Conclusion

We have presented a new model that simulates spectral light transport for sand. Both the spectral and spatial responses (the measurement of appearance [57]) are represented. The model is controlled by parameters that relate to physical and mineralogical properties of sand, and the effects of these parameters on the model show good quantitative and qualitative agreement with what is reported in the literature. There is, however, room for future development. There are two aspects that future work should emphasize: accounting for additional factors that influence light transport in sand (Section 2.2), as well as improving the quantitative accuracy of the model.

9.1 Strengths and Limitations

While there is good qualitative agreement, work still remains to be done to improve the accuracy of the model, so that the reflectance of a provided sand sample may be predicted from the characterization data *for that sample*. Hence, this thesis also serves to point out the lack of and need for spectral BRDF measurements of natural surfaces *along with* the characterization data for those surfaces. Despite the efforts of numerous computer graphics researchers [42, 29, 85], much work still needs to be done in this area. In most cases where the spectral reflectance or BRDF data is available, the corresponding characterization data is not, and *vice versa*. It is therefore difficult to

verify quantitatively any models for these surfaces without making assumptions about the properties of the material in question. However, one can still validate the model qualitatively by demonstrating that modifying input parameters have the expected effect, and quantitatively by showing that it is possible to obtain matches between reflectances from real samples and from the model using plausible input parameters, as we have done.

9.2 Future Work

There is also room for future work in making the model more comprehensive. We chose to focus our attention on the most common types of sands. However, the range of mineralogy present in sands around the world is very diverse [107]. Additionally, the model could be expanded to include other types of soils with varying textures (as defined in Section 2.1). Other factors, such as organic matter, may then become more important. The model could also be expanded to include the infrared region of the spectrum. Absorption by water, for example, would then become an important factor [11, 45]. These improvements would be useful not only to the computer graphics community, but would allow the model to become more useful as a tool to soil and remote sensing scientists for determining soil properties.

Appendix A

Generating a Point on a Spheroid

To implement the SPLITS model using spheroidal particles, it is necessary to generate a random point uniformly on the surface of a particle (see Section 6.3.3).

In the following, we consider a spheroid centered at the origin with its single* axis parallel to the z-axis, as depicted in Figure A.1. We wish to determine the surface area of the spheroid below a plane $z = t$.

A spheroid is the surface of revolution defined by an ellipse

$$\frac{x^2}{a^2} + \frac{z^2}{c^2} = 1, \tag{A.1}$$

where $a > 0$ and $c > 0$, rotated about the z-axis. Solving for $x = f(z)$, we get

$$f(z) = a\sqrt{1 - \frac{z^2}{c^2}}, z \in [-c, c]. \tag{A.2}$$

Let $A_S(t)$ be the surface area of the spheroid below the plane $z = t$. Then [132]

$$A_S(t) = 2\pi \int_{-c}^{t} f(z)\sqrt{1 + (f'(z))^2}\, dz. \tag{A.3}$$

*The single axis is the minor axis for an oblate spheroid and is the major axis for a prolate spheroid.

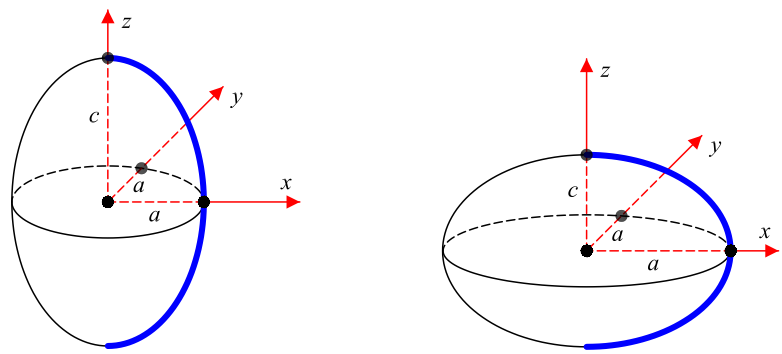

Figure A.1: The two types of spheroids, *Left*: Prolate, *Right*: Oblate. The bold, blue line denotes the indicatrix (Equation (A.2)).

The total surface area of the spheroid is $A_S(c)$. Thus, the fraction of the surface area below the plane $z = t$ is $A_S(t)/A_S(c)$.

Differentiating $f(z)$ yields

$$f'(z) = \frac{-az}{c^2\sqrt{1-\frac{z^2}{c^2}}},$$

and thus

$$(f'(z))^2 = \frac{a^2z^2}{c^4\left(1-\frac{z^2}{c^2}\right)}. \tag{A.4}$$

Substituting Equations (A.2) and (A.4) into the integrand of Equation (A.3) yields

$$\begin{aligned}
&a\sqrt{1-\frac{z^2}{c^2}}\sqrt{1+\frac{a^2z^2}{c^4\left(1-\frac{z^2}{c^2}\right)}} \\
&= a\sqrt{1-\frac{z^2}{c^2}+\frac{a^2z^2}{c^4}} \\
&= a\sqrt{1-\frac{z^2}{c^2}\left(1-\frac{a^2}{c^2}\right)} \text{ or } \sqrt{1+\frac{z^2}{c^2}\left(\frac{a^2}{c^2}-1\right)}.
\end{aligned}$$

We now consider separately two cases: $a < c$ and $a > c$. These correspond to *prolate* and *oblate* spheroids respectively [151, §4.18].

A.1 Prolate Spheroid

For a prolate spheroid, $a < c$, and the *eccentricity*, e, of the spheroid is defined as [128]

$$e = \sqrt{1 - \frac{a^2}{c^2}}. \tag{A.5}$$

Thus, the surface area is

$$A_S(t) = 2\pi a \int_{-c}^{t} \sqrt{1 - e^2 \frac{z^2}{c^2}}\, dz.$$

Let $u = ez/c$. Then $du = e\,dz/c$ and thus $dz = c\,du/e$. Also, as z ranges from $-c$ to t, u ranges from $-e$ to et/c. Substituting, we get

$$A_S(t) = 2\pi \frac{ac}{e} \int_{-e}^{et/c} \sqrt{1 - u^2}\, du.$$

We evaluate the above integration by referring to a table of integrals [151, §5.4.12], yielding

$$\begin{aligned} A_S(t) &= 2\pi \frac{ac}{e} \cdot \frac{1}{2} \left(u\sqrt{1-u^2} + \sin^{-1} u \Big|_{u=-e}^{et/c} \right) \\ &= \pi \frac{ac}{e} \left(\frac{et}{c} \sqrt{1 - \frac{e^2 t^2}{c^2}} + \sin^{-1}\left(\frac{et}{c}\right) + e\sqrt{1-e^2} + \sin^{-1} e \right). \end{aligned}$$

The surface area of the entire spheroid is therefore

$$A_S(c) = 2\pi \frac{ac}{e} \left(e\sqrt{1-e^2} + \sin^{-1} e \right). \tag{A.6}$$

Let $v = t/c$. The fraction $F(v) = A_S(cv)/A_S(c)$ of the surface area below the plane $z = t = cv$ is

$$\begin{aligned} F(v) &= \frac{\pi \frac{ac}{e} \left(e\sqrt{1-e^2} + \sin^{-1} e + ev\sqrt{1-e^2v^2} + \sin^{-1} ev \right)}{2\pi \frac{ac}{e} (e\sqrt{1-e^2} + \sin^{-1} e)} \\ &= \frac{1}{2} \left(1 + \frac{ev\sqrt{1-e^2v^2} + \sin^{-1} ev}{e\sqrt{1-e^2} + \sin^{-1} e} \right). \end{aligned}$$

A.2 Oblate Spheroid

For an oblate spheroid, $a > c$, and the *eccentricity*, e, of the spheroid is defined as [128]

$$e = \sqrt{1 - \frac{c^2}{a^2}}, \tag{A.7}$$

which can be re-expressed as

$$e = \frac{c}{a}\sqrt{\frac{a^2}{c^2} - 1}.$$

Thus, the surface area is

$$\begin{aligned} A_S(t) &= 2\pi a \int_{-c}^{t} \sqrt{1 + \frac{z^2 e^2 a^2}{c^4}}\, dz \\ &= 2\pi \frac{a}{c^2} \int_{-c}^{t} \sqrt{c^4 + z^2 e^2 a^2}\, dz. \end{aligned}$$

Let $u = zea$. Then $du = ea\,dz$ and thus $dz = du/ea$. Also, as z ranges from $-c$ to t, u ranges from $-eac$ to eat.* Substituting, we get

$$A_S(t) = \frac{2\pi}{ec^2} \int_{-eac}^{eat} \sqrt{c^4 + u^2}\, du.$$

Referring to a table of integrals [151, §5.4.11], we get

$$\begin{aligned} A_S(t) &= \frac{2\pi}{ec^2} \cdot \frac{1}{2} \left(u\sqrt{c^4 + u^2} + c^4 \log\left(u + \sqrt{c^4 + u^2}\right) \Big|_{u=-eac}^{eat} \right) \\ &= \frac{\pi}{ec^2} \left(eat\sqrt{c^4 + e^2a^2t^2} + c^4 \log\left(eat + \sqrt{c^4 + e^2a^2t^2}\right) \right. \\ &\qquad \left. + eac\sqrt{c^4 + e^2a^2c^2} - c^4 \log\left(-eac + \sqrt{c^4 + e^2a^2c^2}\right) \right) \\ &= \frac{\pi}{ec^2} \left(eat\sqrt{c^4 + e^2a^2t^2} + eac\sqrt{c^4 + e^2a^2c^2} \right. \\ &\qquad \left. + c^4 \log\left(\frac{eat + \sqrt{c^4 + e^2a^2t^2}}{-eac + \sqrt{c^4 + e^2a^2c^2}} \right) \right). \end{aligned}$$

*mmmmmmm....

The surface area of the entire spheroid is therefore

$$\begin{aligned}
A_S(c) &= 2\pi\frac{a}{c}\sqrt{c^4+e^2a^2c^2}+\pi\frac{c^2}{e}\log\left(\frac{eac+\sqrt{c^4+e^2a^2c^2}}{-eac+\sqrt{c^4+e^2a^2c^2}}\right)\\
&= 2\pi a\sqrt{c^2+e^2a^2}+\pi\frac{c^2}{e}\log\left(\frac{eac+c\sqrt{c^2+e^2a^2}}{-eac+c\sqrt{c^2+e^2a^2}}\right)\\
&= 2\pi a\sqrt{c^2+e^2a^2}+\pi\frac{c^2}{e}\log\left(\frac{ea+\sqrt{c^2+e^2a^2}}{-ea+\sqrt{c^2+e^2a^2}}\right).
\end{aligned}$$

From Equation (A.7), we get that

$$c^2+e^2a^2 = c^2+\left(1-\frac{c^2}{a^2}\right)a^2 = c^2+a^2-c^2 = a^2.$$

Substituting back into the above, we get

$$\begin{aligned}
A_S(c) &= 2\pi a^2+\pi\frac{c^2}{e}\log\left(\frac{ea+a}{-ea+a}\right)\\
&= 2\pi a^2+\pi\frac{c^2}{e}\log\left(\frac{1+e}{1-e}\right).
\end{aligned}$$

Let $v = t/c$. The fraction $F(v) = A_S(cv)/A_S(c)$ of the surface area below the plane $z = t = cv$ is

$$\begin{aligned}
F(v) &= \frac{\frac{\pi}{ec^2}\left(eac\sqrt{c^4+e^2a^2c^2}+eacv\sqrt{c^4+e^2a^2c^2v^2}+c^4\log\left(\frac{eacv+\sqrt{c^4+e^2a^2c^2v^2}}{-eac+\sqrt{c^4+e^2a^2c^2}}\right)\right)}{2\pi a^2+\pi\frac{c^2}{e}\log\left(\frac{1+e}{1-e}\right)}\\
&= \frac{\frac{1}{e}\left(ea\sqrt{c^2+e^2a^2}+eav\sqrt{c^2+e^2a^2v^2}+c^2\log\left(\frac{eav+\sqrt{c^2+e^2a^2v^2}}{-ea+\sqrt{c^2+e^2a^2}}\right)\right)}{2a^2+\frac{c^2}{e}\log\left(\frac{1+e}{1-e}\right)}\\
&= \frac{\frac{1}{e}\left(ea^2+eav\sqrt{c^2+e^2a^2v^2}+c^2\log\left(\frac{eav+\sqrt{c^2+e^2a^2v^2}}{-ea+a}\right)\right)}{2a^2+\frac{c^2}{e}\log\left(\frac{1+e}{1-e}\right)}.
\end{aligned}$$

Dividing the numerator and denominator by a^2, and dividing the numerator and denominator in the

logarithm, yields

$$
\begin{aligned}
F(v) &= \frac{\frac{1}{e}\left(e + ev\sqrt{\frac{c^2}{a^2} + e^2v^2} + \frac{c^2}{a^2}\log\left(\frac{ev+\sqrt{\frac{c^2}{a^2}+e^2v^2}}{1-e}\right)\right)}{2 + \frac{c^2}{ea^2}\log\left(\frac{1+e}{1-e}\right)} \\
&= \frac{\frac{1}{e}\left(e + ev\sqrt{1-e^2+e^2v^2} + (1-e^2)\log\left(\frac{ev+\sqrt{1-e^2+e^2v^2}}{1-e}\right)\right)}{2 + \frac{1-e^2}{e}\log\left(\frac{1+e}{1-e}\right)} \\
&= \frac{e\left(1 + v\sqrt{1-e^2+e^2v^2}\right) + (1-e^2)\log\left(\frac{ev+\sqrt{1-e^2+e^2v^2}}{1-e}\right)}{2e + (1-e^2)\log\left(\frac{1+e}{1-e}\right)}.
\end{aligned}
$$

Appendix B

Mixing Minerals

This appendix deals with issues concerning the relationships between mass and volume fractions of a mixture of materials with varying densities. These issues arose frequently during the specification of the SPLITS model (Chapter 6).

B.1 Density of a Mixture

As we will see, to convert between mass and volume fractions, we must first determine the density, γ, of the mixture. Consider a series of m minerals, with densities $\gamma_1, \ldots, \gamma_m$. Let V_j and M_j be the volume and mass of the jth mineral, respectively, and define

$$V = \sum_j V_j$$

to be the total volume, and

$$M = \sum_j M_j$$

to be the total mass. The density is then $\gamma = M/V$. In general, however, we will know the V_j but not the M_j, or *vice versa*.

If we are given the volumes, V_j, for $1 \leq j \leq m$, and thus the total volume, V, we may re-express

the density as

$$\gamma = \frac{\sum_j M_j}{V}.$$

Noting that $\gamma_j = M_j/V_j$, we have

$$\gamma = \frac{\sum_j \gamma_j V_j}{V} = \sum_j \gamma_j \frac{V_j}{V}.$$

Thus, defining the volume *fractions* $\nu_j = V_j/V$ of each constituent j, we have

$$\gamma = \sum_j \gamma_j \nu_j. \tag{B.1}$$

If, instead, we are provided with the masses, M_j, of each of the minerals, then we write the density as

$$\gamma = \frac{M}{\sum_j V_j}.$$

As $\gamma_j = M_j/V_j$,

$$\gamma = \frac{M}{\sum_j \frac{M_j}{\gamma_j}} = \frac{1}{\sum_j \frac{M_j}{\gamma_j M}}.$$

Now we define the mass fractions $\mu_j = M_j/M$. Substituting yields

$$\gamma = \left(\sum_j \frac{\mu_j}{\gamma_j} \right)^{-1}. \tag{B.2}$$

Note that Equations (B.1) and (B.2) may be used to compute the density of a particle given the volume (respectively mass) concentrations of its mineral constituents. It may also be used to compute the mean particle density given the densities and volume (respectively mass) fractions of each of the different types of particles.

B.2 Converting Between Mass and Volume Fractions

The data provided in the literature describing fractions is often in the form of *mass* fractions (*e.g.*, the sand separate fractions, ζ_1, ζ_2, and ζ_3). However, the SPLITS model requires that these be

converted into *volume* fractions. We must, therefore, determine how to perform this conversion.

By definition, $\mu_j = M_j/M$ and $\nu_j = V_j/V$. Since $\gamma_j = M_j/V_j$ and $\gamma = M/V$, we have

$$\mu_j = \frac{\gamma_j V_j}{\gamma V} = \frac{\gamma_j}{\gamma}\nu_j. \tag{B.3}$$

Similarly, $\nu_j = \gamma\mu_j/\gamma_j$.

B.3 Coated Particles

In the SPLITS model, some particles consist of a pure core with a mixed coating (Section 6.2.5). Given

- γ_c, the density of the core,
- γ_m, the density of the coating matrix,
- γ_i, the density of the inclusions in the coating,
- ϑ_i, the mass fraction of the inclusions over the whole particle, and
- ν_{coat}, the volume fraction of the coating,

we require the mass fraction ϑ_m of the matrix over the whole particle.

Let V be the volume of the entire particle and V_c, V_m, V_i be the volumes of the core, matrix, and inclusions respectively. Hence,

$$V = V_c + V_m + V_i. \tag{B.4}$$

Similarly, let M be the mass of the particle and M_c, M_m, M_i be the masses of the core, matrix, and inclusions. Now we may express the overall mass fraction of the inclusions as

$$\vartheta_i = \frac{M_i}{M} = \frac{\gamma_i V_i}{M}. \tag{B.5}$$

Similarly,

$$\vartheta_m = \frac{\gamma_m V_m}{M}.$$

From Equation (B.4), we now have

$$\begin{aligned}\vartheta_m &= \frac{\gamma_m (V - V_c - V_i)}{M} \\ &= \frac{\gamma_m (V - V_c)}{M} - \frac{\gamma_m V_i}{M} \\ &= \frac{\gamma_m (V - V_c)}{M} - \frac{\gamma_m}{\gamma_i}\left(\frac{\gamma_i V_i}{M}\right).\end{aligned}$$

Substituting Equation (B.5) into the preceding yields

$$\vartheta_m = \frac{\gamma_m (V - V_c)}{M} - \frac{\gamma_m}{\gamma_i}\vartheta_i.$$

Recalling that ν_{coat} is the volumetric fraction of the coating, and noting that $V - V_c$ is the volume of the coating, we have $V - V_c = \nu_{coat} V$. Therefore,

$$\vartheta_m = \frac{\gamma_m \nu_{coat} V}{M} - \frac{\gamma_m}{\gamma_i}\vartheta_i. \tag{B.6}$$

Expanding M, we get

$$M = M_c + M_m + M_i = \gamma_c V_c + \gamma_m V_m + \gamma_i V_i.$$

By expressing Equation (B.4) in terms of V_m and substituting into the preceding, we get

$$\begin{aligned}M &= \gamma_c V_c + (V - V_c - V_i)\gamma_m + \gamma_i V_i \\ &= \gamma_c V_c + \gamma_m (V - V_c) + (\gamma_i - \gamma_m) V_i \\ &= \gamma_c V_c + \gamma_m (V - V_c) + \left(\frac{\gamma_i - \gamma_m}{\gamma_i}\right)\gamma_i V_i.\end{aligned}$$

As $\vartheta_i = \gamma_i V_i / M$, we have

$$M = \gamma_c V_c + \gamma_m (V - V_c) + \left(\frac{\gamma_i - \gamma_m}{\gamma_i}\right)\vartheta_i M.$$

We have now expressed M in terms of itself. Solving for M yields

$$M = \frac{\gamma_c V_c + \gamma_m (V - V_c)}{1 - \left(\frac{\gamma_i - \gamma_m}{\gamma_i}\right) \vartheta_i}$$

By multiplying the top and bottom by γ_i, and once again substituting $V_c = (1 - \nu_{coat})V$, we get

$$M = \gamma_i \cdot \frac{\gamma_c (1 - \nu_{coat})V + \gamma_m \nu_{coat} V}{\gamma_i - (\gamma_i - \gamma_m)\, \vartheta_i}$$

Substituting back into Equation (B.6),

$$\begin{aligned}
\vartheta_m &= \frac{\gamma_m \nu_{coat} V\,(\gamma_i - \gamma_i \vartheta_i + \gamma_m \vartheta_i)}{\gamma_i\,(\gamma_c (1 - \nu_{coat})V + \gamma_m \nu_{coat} V)} - \frac{\gamma_m}{\gamma_i} \vartheta_i \\
&= \frac{\gamma_m}{\gamma_i} \left(\frac{\gamma_i \nu_{coat} - \gamma_i \nu_{coat} \vartheta_i + \gamma_m \nu_{coat} \vartheta_i}{\gamma_c (1 - \nu_{coat}) + \gamma_m \nu_{coat}} - \vartheta_i \right) \\
&= \frac{\gamma_m}{\gamma_i} \left(\frac{\gamma_i \nu_{coat} (1 - \vartheta_i) + \gamma_m \nu_{coat} \vartheta_i - \gamma_c (1 - \nu_{coat}) \vartheta_i - \gamma_m \nu_{coat} \vartheta_i}{\gamma_c (1 - \nu_{coat}) + \gamma_m \nu_{coat}} \right) \\
&= \frac{\gamma_m}{\gamma_i} \left(\frac{\gamma_i \nu_{coat} (1 - \vartheta_i) - \gamma_c (1 - \nu_{coat}) \vartheta_i}{\gamma_c (1 - \nu_{coat}) + \gamma_m \nu_{coat}} \right).
\end{aligned}$$

Bibliography

[1] J. Arvo. *Analytic Methods for Simulated Light Transport*. PhD thesis, Yale University, December 1995.

[2] S. Asano. Light scattering properties of spheroidal particles. *Applied Optics*, 18(5):712–723, March 1979.

[3] F. Aurenhammer. Voronoi diagrams — a survey of a fundamental geometric data structure. *ACM Computing Surveys*, 23(3):345–405, September 1991.

[4] M.V. Baikov, A.N. Ponyavina, A.P. Prishivalko, V.V. Sviridov, and N.I. Sil'vanovich. Effect of the microstructure of closely packed ultradisperse hematite layers on their spectral properties. *Journal of Applied Spectroscopy*, 63(3):297–303, 1996.

[5] P.C. Bailey. Absorption and reflectivity measurements on some rare earth iron garnets and α-Fe_2O_3. *Journal of Applied Physics*, 31(5):39S–40S, May 1960.

[6] G.V.G. Baranoski, A. Krishnaswamy, and B. Kimmel. Revisiting the foundations of subsurface scattering. Technical Report CS-2003-45, University of Waterloo, December 2003.

[7] G.V.G. Baranoski, A. Krishnaswamy, and B. Kimmel. An investigation on the use of data-driven scattering profiles in Monte Carlo simulations of ultraviolet light propagation in skin tissues. *Physics in Medicine and Biology*, 49(20):4799–4809, October 2004.

[8] G.V.G. Baranoski, A. Krishnaswamy, and B. Kimmel. Increasing the predictability of tissue subsurface scattering simulations. *The Visual Computer*, 24(4):265–278, May 2005.

[9] G.V.G. Baranoski, J.G. Rokne, and G. Xu. Virtual spectrophotometric measurements for biologically and physically based rendering. *The Visual Computer*, 17(8):506–518, November 2001.

[10] V. Barron and L. Montealegre. Iron oxides and color of triassic sediments: Application of the Kubelka-Munk theory. *American Journal of Science*, 286(10):792–802, December 1986.

[11] M.F. Baumgardner, L.F. Silva, L.L. Biehl, and E.R. Stoner. Reflectance properties of soils. *Advances in Agronomy*, 38:1–43, 1985.

[12] A. Bedidi and B. Cervelle. Light scattering by spherical particles with hematite and goethite-like optical properties: Effect of water impregnation. *Journal of Geophysical Research*, 98(B7):11941–11952, July 1993.

[13] N. Bell, Y. Yu, and P.J. Mucha. Particle-based simulation of granular materials. In *Proceedings of the Eurographics/ACM SIGGRAPH Symposium on Computer Animation*, pages 77–86, July 2005.

[14] J.F. Blinn. Simulation of wrinkled surfaces. In *Computer Graphics (SIGGRAPH Proceedings)*, volume 12, pages 286–292, August 1978.

[15] C.F. Bohren and D.R. Huffman. *Absorption and Scattering of Light by Small Particles*. John Wiley and Sons, New York, NY, 1983.

[16] M. Born and E. Wolf. *Principles of Optics*. Pergamon Press, Oxford, England, 6th edition, 1980.

[17] N.C. Brady. *The Nature and Properties of Soils*. Macmillan Publishing Co., Inc., New York, NY, 8th edition, 1974.

[18] N.C. Brady and R.R. Weil. *Elements of the Nature and Properties of Soils*. Prentice-Hall, Inc., Upper Saddle River, NJ, 2000.

[19] B. Chanclou, A. Luciani, and A. Habibi. Physical models of loose soils dynamically marked by a moving object. In *Computer Animation '96*, pages 27–35, June 1996.

[20] J. Cierniewski. A model for soil surface roughness influence on the spectral response of bare soils in the visible and near-infrared range. *Remote Sensing of Environment*, 23:92–115, 1987.

[21] J. Cierniewski and A. Karnieli. Virtual surfaces simulating the bidirectional reflectance of semi-arid soils. *International Journal of Remote Sensing*, 23(19):4019–4037, 2002.

[22] R.N. Clark, G.A. Swayze, A.J. Gallagher, T.V.V. King, and W.M. Calvin. The U.S. Geological Survey digital spectral library: Version 1: 0.2 to 3.0 microns. United States Geological Survey Open File Report 93-592, 1993. http://speclab.cr.usgs.gov.

[23] K.D. Cooper and J.A. Smith. A Monte Carlo reflectance model for soil surfaces with three-dimensional structure. *IEEE Transactions on Geoscience and Remote Sensing*, GE-23(5):668–673, September 1985.

[24] R.M. Cornell and U. Schwertmann. *The Iron Oxides*. Wiley-VCH GmbH & Co. KGaA, Weinheim, Germany, 2nd edition, 2003.

[25] K.L. Coulson, G.M. Bouricius, and E.L. Gray. Optical reflection properties of natural surfaces. *Journal of Geophysical Research*, 70(18):4601–4611, September 1965.

[26] K.L. Coulson and D.W. Reynolds. The spectral reflectance of natural surfaces. *Journal of Applied Meteorology*, 10(6):1285–1295, 1971.

[27] A.J. Criddle. Microscope-photometry, reflectance measurement, and quantitative color. In J.L. Jambor and D.J. Vaughan, editors, *Advanced Microscopic Studies of Ore Minerals*, vol-

ume 17, chapter 6, pages 135–170. Mineralogical Association of Canada, Ottawa, ON, May 1990. Short Course Handbook.

[28] T.J. Cudahy and E.R. Ramanaidou. Measurement of the hematite:goethite ratio using field visible and near-infrared reflectance spectrometry in channel iron deposits, Western Australia. *Australian Journal of Earth Sciences*, 44(4):411–420, 1997.

[29] K.J. Dana, B. van Ginneken, S.K. Nayar, and J.J. Koenderink. Reflectance and texture of real world surfaces. *ACM Transactions on Graphics*, 18(1):1–34, January 1999.

[30] D. Despan, A. Bedidi, and B. Cervelle. Bidirectional reflectance of rough bare soil surfaces. *Geophysical Research Letters*, 27(17):2777–2780, September 1999.

[31] W.G. Egan and T. Hilgeman. Spectral reflectance of particulate materials: A Monte Carlo model including asperity scattering. *Applied Optics*, 17(2):245–252, January 1978.

[32] W.G. Egan and T.W. Hilgeman. *Optical Properties of Inhomogeneous Materials: Applications to Geology, Astronomy, Chemistry, and Engineering*. Academic Press, New York, NY, 1979.

[33] D.D. Egbert. A practical method for correcting bidirectional reflectance variations. In *Proceedings of the Fourth Annual Symposium on Machine Processing of Remotely Sensed Data*, pages 178–189, 1977.

[34] P.G. Embrey and A.J. Criddle. Error problems in the two-media method of deriving the optical constants n and k from measured reflectances. *American Mineralogist*, 63:853–862, 1978.

[35] A.G. Emslie and J.R. Aronson. Spectral reflectance of particulate materials. 1: Theory. *Applied Optics*, 12(11):2563–2572, November 1973.

[36] P.A. Farrant. *Color in Nature: A Visual and Scientific Exploration*. Blandford Press, 1999.

[37] P. Fearing. Computer modelling of fallen snow. In *Computer Graphics Proceedings, Annual Conference Series*, pages 37–46, July 2000.

[38] J.A. Galantini, N. Senesi, G. Brunetti, and R. Rosell. Influence of texture on organic matter distribution and quality and nitrogen and sulphur status in semiarid pampean grassland soils of Argentina. *Geoderma*, 123(1–2):143–152, November 2004.

[39] A.I. Galuza, V.V. Eremenko, and A.P. Kirichenko. Analysis of hematite reflection spectrum by the Kramers-Kronig method. *Soviet Physics – Solid State*, 21(4):654–656, April 1979.

[40] L.S. Galvão and I. Vitorello. Role of organic matter in obliterating the effects of iron on spectral reflectance and colour of Brazilian tropical soils. *International Journal of Remote Sensing*, 19(10):1969–1979, 1998.

[41] J. Gerrard. *Fundamentals of Soils*. Routledge, New York, NY, 2000.

[42] D.P. Greenberg, J. Arvo, E. Lafortune, K.E. Torrance, J.A. Ferwerda, B. Walter, B. Trumbore, P. Shirley, S. Pattanaik, and S. Foo. A framework for realistic image synthesis. In *Computer Graphics Proceedings, Annual Conference Series*, pages 477–494, August 1997.

[43] C.D. Gribble and A.J. Hall. *Optical Mineralogy: Principles and Practice*. Chapman & Hall, New York, NY, 1993.

[44] C.I. Grove, S.J. Hook, and E.D. Paylor II. Laboratory reflectance spectral of 160 minerals, 0.4 to 2.5 micrometers. JPL Publication 92-2, Jet Propulsion Laboratory, Pasadena, CA, 1992.

[45] G.M. Hale and M.R. Querry. Optical constants of water in the 200-nm to 200-μm wavelength region. *Applied Optics*, 12(3):555–563, March 1973.

[46] J.M. Hammersley and D.C. Handscomb. *Monte Carlo Methods*. Methuen & Co., Ltd., London, England, 1967.

[47] P. Hanrahan and W. Krueger. Reflection from layered surfaces due to subsurface scattering. In *Computer Graphics (SIGGRAPH Proceedings)*, volume 27, pages 165–174, August 1993.

[48] B. Hapke. Bidirectional reflectance spectroscopy. 1. theory. *Journal of Geophysical Research*, 86(B4):3039–3054, April 1981.

[49] B. Hapke. Bidirectional reflectance spectroscopy. 4. the extinction coefficient and the opposition effect. *Icarus*, 67(2):264–280, August 1986.

[50] B. Hapke and E. Wells. Bidirectional reflectance spectroscopy. 2. experiments and observations. *Journal of Geophysical Research*, 86(B4):3055–3054, April 1981.

[51] P.S. Heckbert. Survey of texture mapping. In *Proceedings of Graphics Interface'86 and Vision Interface '86*, pages 207–212, May 1986.

[52] L.G. Henyey and J.L. Greenstein. Diffuse radiation in the galaxy. *Astrophysical Journal*, 93:70–83, 1941.

[53] W.P. Hsu and E. Matijević. Optical properties of monodispersed hematite hydrosols. *Applied Optics*, 24(11):1623–1630, June 1985.

[54] K.F. Huemmrich. Soil reflectance data (FIFE). Data set, 1994. Oak Ridge National Laboratory, Oak Ridge, TN. http://www.daac.ornl.gov.

[55] G.R. Hunt and J.W. Salisbury. Visible and near-infrared spectra of minerals and rocks: I. silicate minerals. *Modern Geology*, 1(4):283–300, November 1970.

[56] G.R. Hunt, J.W. Salisbury, and C.J. Lenhoff. Visible and near-infrared spectra of minerals and rocks: III. oxides and hydroxides. *Modern Geology*, 2(3):195–205, May 1971.

[57] R. Hunter and R. Harold. *The Measurement of Appearance*. John Wiley and Sons, New York, NY, 2nd edition, 1987.

[58] H.R. Ingleby and T.G. Crowe. Reflectance models for predicting organic carbon in saskatchewan soils. *Canadian Agricultural Engineering*, 42(2):57–63, 2000.

[59] J.R. Irons and J.A. Smith. Soil surface roughness characterization from light scattering observations. In *Proceedings of the IEEE International Geoscience and Remote Sensing Symposium*, volume 2, pages 1007–1010, 1990.

[60] W.M. Irvine. Multiple scattering by large particles. *Astrophysical Journal*, 142(4):1563–1575, November 1965.

[61] A. Ishimaru. *Wave Propagation and Scattering in Random Media*, volume 1. IEEE Press, New York, NY, 2nd edition, 1987.

[62] K. Islam, B. Singh, and A. McBratney. Simultaneous estimation of several soil properties by ultra-violet, visible, and near-infrared reflectance spectroscopy. *Australian Journal of Soil Research*, 41:1101–1114, 2003.

[63] S. Jacquemoud and F. Baret. PROSPECT: A model of leaf optical properties spectra. *Remote Sensing of Environment*, 34(2):75–92, 1990.

[64] S. Jacquemoud, S.L. Ustin, J. Verdebout, G. Schmuck, G. Andreoli, and B. Hosgood. Estimating leaf biochemistry using PROSPECT leaf optical properties model. *Remote Sensing of Environment*, 56:194–202, 1996.

[65] H.W. Jensen, J. Legakis, and J. Dorsey. Rendering of wet materials. In *Proceedings of the Eurographics Workshop on Rendering*, pages 273–282, 1999.

[66] M. Kass and G. Miller. Rapid, stable fluid dynamics for computer graphics. In *Computer Graphics (SIGGRAPH Proceedings)*, volume 24, pages 49–57, 1990.

[67] M. Kerker. *The Scattering of Light, and Other Electromagnetic Radiation*. Academic Press, New York, NY, 1969.

[68] M. Kerker, P. Scheiner, D.D. Cooke, and J.P. Kratohvil. Absorption index and color of colloidal hematite. *Journal of Colloid and Interface Science*, 71(1):176–187, August 1979.

[69] J. Königsberger. Über messungen des reflexionsmögens und bestimmung der optischen konstanten. *Annalen der Physik*, 43:1205–1222, 1913.

[70] H.A. Kramers. La difusion de la lumiere pa les atoines. In *Atti del Congresso Internazionale de Fisici*, pages 545–557, Como, 1927.

[71] A. Krishnaswamy and G.V.G. Baranoski. A biophysically-based spectral model of light interaction with human skin. *Computer Graphics Forum*, 23(3):331–340, 2004.

[72] A. Krishnaswamy, G.V.G. Baranoski, and J.G. Rokne. Virtual goniophotometric measurements protocol. Technical Report CS-2002-21, University of Waterloo, July 2002.

[73] R. Kronig. On the theory of the dispersion of X-rays. *Journal of the Optical Society of America*, 12:547–557, 1926.

[74] W.C. Krumbein. Measurement and geological significance of shape and roundness of sedimentary particles. *Journal of Sedimentary Petrology*, 11(2):64–72, August 1941.

[75] P. Kubelka and F. Munk. Ein beitrag zur optik der farbanstriche (An article on optics of paint layers). *Zeitschrift für Technische Physik*, 12:593–601, August 1931.

[76] M. Kühl and B.B. Jørgensen. The light field of microbenthic communities: Radiance distribution and microscale optics of sandy coastal sediments. *Limnology and Oceanography*, 39(6):1368–1398, 1994.

[77] D.J. Leu. Visible and near-infrared reflectance of beach sands: A study on the spectral reflectance/grain size relationship. *Remote Sensing of Environment*, 6(3):169–182, 1977.

[78] X. Li and J.M. Moshell. Modeling soil: Realtime dynamic models for soil slippage and manipulation. In *Computer Graphics (SIGGRAPH Proceedings)*, volume 27, pages 361–368, August 1993.

[79] Z. Li, A.K. Fung, D.P. Gibbs, C.L. Betty, S. Tjuatja, and J.R. Irons. A modeling study of bidirectional reflectance from soil surfaces. In *Proceedings of the IEEE International Geoscience and Remote Sensing Symposium*, volume 3, pages 1835–1837, August 1994.

[80] Z. Li, A.K. Fung, S. Tjuatja, D.P. Gibbs, C.L. Betty, and J.R. Irons. A modeling study of backscattering from soil surfaces. *IEEE Transactions on Geoscience and Remote Sensing*, 34(1):264–271, January 1996.

[81] D.B. Lobell and G.P. Asner. Moisture effects on soil reflectance. *Soil Science Society of America Journal*, 66(3):722–727, May 2002.

[82] J.E. Marsden and M.J. Hoffman. *Elementary Classical Analysis*. W.H. Freeman and Company, New York, NY, 2nd edition, 1993.

[83] L.A. Marusak, R. Messier, and W.B. White. Optical absorption spectrum of hematite, αFe_2O_3 near IR to UV. *Journal of the Physics and Chemistry of Solids*, 41(9):981–984, 1980.

[84] A.D. Matthias, A. Fimbres, E.E. Sano, D.F. Post, L. Accioly, A.K. Batchily, and L.G. Ferreira. Surface roughness effects on soil albedo. *Soil Science Society of America Journal*, 64(3):1035–1041, May 2000.

[85] W. Matusik, H. Pfister, M. Brand, and L. McMillan. A data-driven reflectance model. *ACM Transactions on Graphics*, 22(3):759–769, July 2003.

[86] M. Messiter and Y. Shamash. Product and sum separable functions. *IEEE Transactions on Automatic Control*, AC-30(7):694–697, July 1985.

[87] M. Minnaert. The reciprocity principal in lunar photometry. *Astrophysical Journal*, 93(3):403–410, May 1941.

[88] H. Momiji. *Mathematical Modelling of the Dynamics and Morphology of Aeolian Dunes and Dune Fields*. PhD thesis, University of London, November 2001.

[89] R.V. Morris and D.C. Golden. Goldenrod pigments and the occurrence of hematite and possibly goethite in the Olympus-Amazonis region of Mars. *Icarus*, 134:1–10, 1998.

[90] A. Mottana, R. Crespi, and G. Liborio. *Simon and Schuster's Guide to Rocks and Minerals*. Simon and Schuster, Inc., New York, NY, 1978.

[91] R.H. Muller. Definitions and conventions in ellipsometry. *Surface Science*, 16:14–33, 1969.

[92] T. Nagano, H. Isobe, S. Nakashima, and M. Ashizaki. Characterization of iron hydroxides in a weathered rock surface by visible microspectroscopy. *Applied Spectroscopy*, 56(5):651–657, 2002.

[93] D.L. Neema, A. Shah, and A.N. Patel. A statistical optical model for light reflection and penetration through sand. *International Journal of Remote Sensing*, 8(8):1209–1217, 1987.

[94] D. Nickerson. History of the Munsell color system and its scientific application. *Journal of the Optical Society of America*, 30(12):575–645, December 1940.

[95] F.E. Nicodemus, J.C. Richmond, J.J. Hsia, I.W. Ginsberg, and T. Limperis. *Geometrical Considerations and Nomenclature for Reflectance*. National Bureau of Standards, United States Department of Commerce, October 1977.

[96] H. Nishimori and N. Ouchi. Formation of ripple patterns and dunes by wind-blown sand. *Physical Review Letters*, 71(1):197–200, July 1993.

[97] T. Nishita and Y. Dobashi. Modeling and rendering of various natural phenomena consisting of particles. In *Proceedings of the Computer Graphics International Conference*, pages 149–156, July 2001.

[98] J.M. Norman, J.M. Welles, and E.A. Walter. Contrasts among bidirectional reflectance of leaves, canopies, and soils. *IEEE Transactions on Geoscience and Remote Sensing*, GE-23(5):659–667, September 1985.

[99] T. Nousiainen, K. Muinonen, and P. Räisänen. Scattering of light by large Saharan dust particles in a modified ray optics approximation. *Journal of Geophysical Research*, 108(D1):AAC 12–1–17, January 2003.

[100] G.S. Okin and T.H. Painter. Effect of grain size on remotely sensed spectral reflectance of sandy desert surfaces. *Remote Sensing of Environment*, 89:272–280, 2004.

[101] J. Ollerhead. Light transmittance through dry, sieved sand: Some test results. *Ancient TL*, 19(1):13–17, 2001.

[102] K. Onoue and T. Nishita. A method for modeling and rendering dunes with wind-ripples. In *Proceedings of the Pacific Conference on Computer Graphics and Applications*, pages 427–428, October 2000.

[103] K. Onoue and T. Nishita. Virtual sandbox. In *Proceedings of the Pacific Conference on Computer Graphics and Applications*, pages 252–259, October 2003.

[104] K. Onoue and T. Nishita. An interactive deformation system for granular material. *Computer Graphics Forum*, 24(1):51–60, March 2005.

[105] M. Oren and S.K. Nayar. Generalization of Lambert's reflectance model. In *Computer Graphics Proceedings, Annual Conference Series*, pages 239–246, 1994.

[106] F.L. Pedrotti and L.S. Pedrotti. *Introduction to Optics*. Prentice Hall, Upper Saddle River, NJ, 2nd edition, 1993.

[107] F.J. Pettijohn, P.E. Potter, and R. Siever. *Sand and Sandstone*. Springer-Verlag, New York, NY, 2nd edition, 1987.

[108] H.R. Phillip. Silicon dioxide (SiO_2), type α, (crystalline). In E.D. Palik, editor, *Handbook of Optical Constants and Solids*, volume 1, pages 719–747. Academic Press, 1985.

[109] S.I. Popova, T.S. Tolstykh, and L.S. Ivlev. Optical constants of Fe_2O_3 in the infrared range of the spectrum. *Optics and Spectroscopy*, 35(5):551–552, November 1973.

[110] S.A. Prahl. *Light Transport in Tissue*. PhD thesis, University of Texas at Austin, December 1988.

[111] S. Premŏze. Analytic light transport approximations for volumetric materials. In *Proceedings of the Pacific Conference on Computer Graphics and Applications*, pages 48–57, October 2002.

[112] A.P. Prishivalko and E.K. Naumenko. A nephelometric method for determining the transparency of dispersion media. *Zhurnal Prikladnoi Spektroskopii*, 17(4):687–694, October 1972. (Russian).

[113] T. Radhakrishnan. Further studies on the temperature variation of the refractive index of crystals. In *Proceedings of the Indian Acadamy of Sciences. Section A*, volume A33, pages 22–34, 1951.

[114] N.A. Riley. Projection sphericity. *Journal of Sedimentary Petrology*, 11(2):94–95, August 1941.

[115] J.N. Rinker, C.S. Breed, J.F. McCauley, and P.A. Corl. Remote sensing field guide — desert. Technical Report ETL-0588, U.S. Army Topographic Engineering Center, Fort Belvoir, VA, September 1991.

[116] S.M. Ross. *A First Course in Probability*. Prentice Hall, Upper Saddle River, NJ, 5th edition, 1998.

[117] P. Roudier, B. Peroche, and M Perrin. Landscape synthesis achieved through erosion and deposition process simulation. *Computer Graphics Forum*, 12(3):375–383, September 1993.

[118] H.L. Royden. *Real Analysis*. Prentice Hall, Englewood Cliffs, NJ, 3rd edition, 1988.

[119] A. Schlegel, S.F. Alvarado, and P. Wachter. Optical properties of magnetite (Fe_3O_4). *Journal of Physics C: Solid State Physics*, 12(6):1157–1164, March 1979.

[120] D.J. Shaw. *Introduction to Colloid and Surface Chemistry*. Butterworth-Heinemann, Oxford, England, 4th edition, 1992.

[121] D.M. Sherman and T.D. Waite. Electronic spectra of Fe^{3+} oxides and oxide hydroxides in the near IR to near UV. *American Mineralogist*, 70:1262–1269, 1985.

[122] M.A. Shirazi and L. Boersma. A unifying quantitative analysis of soil texture. *Soil Science Society of America Journal*, 48(1):142–147, 1984.

[123] M.A. Shirazi, L. Boersma, and J.W. Hart. A unifying quantitative analysis of soil texture: Improvement of precision and extention of scale. *Soil Science Society of America Journal*, 52(1):181–190, 1988.

[124] M.A. Shirazi, L. Boersma, and C.B. Johnson. Particle-size distributions: Comparing texture systems, adding rock, and predicting soil properties. *Soil Science Society of America Journal*, 65(2):300–310, March 2001.

[125] P. Shirley. *Physically Based Lighting Calculations for Computer Graphics*. PhD thesis, Department of Computer Science, University of Illinois at Urbana-Champaign, December 1990.

[126] R.A. Shuchman and D.K. Rea. Determination of beach sand parameters using remotely sensed aircraft reflectance data. *Remote Sensing of Environment*, 11:295–310, 1981.

[127] R.B. Singer. Spectral evidence for the mineralogy of high-albedo soils and dust on Mars. *Journal of Geophysical Research*, 87(B12):10159–10168, November 1982.

[128] J.P. Snyder. *Map Projections: A Working Manual*. United States Government Printing Office, Washington, 1987. U.S. Geological Survey Professional Paper 1395.

[129] Soil Science Division Staff. *Soil Survey Manual*. Soil Conservation Service, 1993. United States Department of Agriculture Handbook 18.

[130] I.N. Sokolik and O.B. Toon. Incorporation of mineralogical composition into models of the radiative properties of mineral aerosol from UV to IR wavelengths. *Journal of Geophysical Research*, 104(D8):9423–9444, April 1999.

[131] R. Soulié, S. Mérillou, O. Terraz, and D. Ghazanfarpour. Modélisation et rendu de matériaux granuleux hétérogènes. In *Actes du Group de Travail Rendu et Visualisation*, April 2004.

[132] M. Spivak. *Calculus*. Publish or Perish, Inc., Houston, TX, 3rd edition, 1994.

[133] J. Stam. An illumination model for a skin layer bounded by rough surfaces. In P. Hanrahan and W. Purgathofer, editors, *Rendering Techniques 2001 (Proceedings of the 12th Eurographics Rendering Workshop)*, pages 39–52, London, England, June 2001. Springer-Verlag.

[134] E.R. Stoner, M.F. Baumgardner, L.L. Biehl, and B.F. Robinson. Atlas of soil reflectance properties. Research Bulletin 962, Agricultural Experiment Station, Purdue University, West Lafayette, Indiana, May 1980.

[135] D.E. Strebel, D.R. Landis, K.F. Huemmrich, and B.W. Meeson. Collected data of the First ISLSCP Field Experiment, vol. 1: Surface observations and non-image data sets. CD-ROM, 1994. National Aeronautics and Space Administration, Goddard Space Flight Center, Greenbelt, MD. Available from http://www.daac.ornl.gov.

[136] R.W. Sumner, J.F. O'Brien, and J.K. Hodgins. Animating sand, mud, and snow. In *Proceedings of Graphics Interface '98*, pages 125–132, Vancouver, British Columbia, Canada, June 1998.

[137] R.W. Sumner, J.F. O'Brien, and J.K. Hodgins. Animating sand, mud, and snow. *Computer Graphics Forum*, 18(1):17–27, January 1999.

[138] J. Torrent, U. Schwertmann, H. Fechter, and F. Alferez. Quantitative relationships between soil color and hematite content. *Soil Science*, 136(6):354–358, December 1983.

[139] W.J. Tropf, M.E. Thomas, and T.J. Harris. Properties of crystals and glasses. In M. Bass, E.W. Van Stryland, D.R. Williams, and W.L. Wolfe, editors, *Handbook of Optics*, volume 2, chapter 33. McGraw-Hill, 2nd edition, 1995.

[140] S.A. Twomey, C.F. Bohren, and J.L. Mergenthaler. Reflectance and albedo differences between wet and dry surfaces. *Applied Optics*, 25(3):57–84, February 1986.

[141] A. Uesugi, W.M. Irvine, and Y. Kawata. Formation of absorption spectra by diffuse reflection from a semi-infinite planetary atmosphere. *Journal of Quantitative Spectroscopy and Radiative Transfer*, 11(6):797–808, June 1971.

[142] H.C. van de Hulst. *Light Scattering by Small Particles*. Dover Publications, New York, NY, 1981.

[143] M.J. Vepraskas and D.K. Cassel. Sphericity and roundness of sand in coastal plain soils and relationships with soil physical properties. *Soil Science Society of America Journal*, 51(5):1108–1112, 1987.

[144] R.C. Vernon. Extinction coefficient of single-crystal hematite in the region 3600–6000 Å. *Journal of Applied Physics*, 33(6):2140–2141, June 1962.

[145] R.K. Vincent and G.R. Hunt. Infrared reflectance from mat surfaces. *Applied Optics*, 7(1):53–59, January 1968.

[146] H. Wadell. Volume, shape, and roundness of rock particles. *Journal of Geology*, 40:443–451, 1932.

[147] C.L. Walthall, J.M. Norman, J.M. Welles, G. Campbell, and B.L. Blad. Simple equation to approximate the bidirectional reflectance from vegetation canopies and bare soil surfaces. *Applied Optics*, 24:383–387, 1985.

[148] L.B. Wolff. Diffuse-reflectance model for smooth dielectric surfaces. *Journal of the Optical Society of America A (Optics, Image Science, and Vision)*, 11(11):2956–2968, November 1994.

[149] H. Wopfner and C.R. Twindale. Formation and age of desert dunes in the Lake Eyre depocentres in central Australia. *Geologische Rundschau*, 77(3):815–834, 1988.

[150] Y. Zhu and R. Bridson. Deformable models: Animating sand as a fluid. *ACM Transactions on Graphics*, 24(3):965–972, July 2005.

[151] D. Zwillinger. *CRC Standard Mathematical Tables and Formulae*. Chapman & Hall/CRC, 31st edition, 2003.

Index

absorbance, 27
absorption coefficient, 20
absorption index, 20
aeolian transport, 14
air, 5, 9, 39, 53
ASTER spectral library, 80
attenuation coefficient, 20, 54
attenuation index, 20

beach sand, 1, 9, 29, 80
birefringence, 21, 27
BRDF, 39, 79, 85–87
British Standards Institute, 6
BSI, *see* British Standards Institute
bump mapping, 1, 14

calcite, 8, 21
cation exchange capacity, 11
CEC, *see* cation exchange capacity
characterization data, 1, 39, 79, 80, 87
convex, 71, 74
cross section
    geometric, 67, 68, 74, 76, 77
cumulative density function, 60
    normal, 50

degree of saturation, 31, 41, 42, 53, 81, 83
density, 28, 48, 50, 57, 95–97
    particle, *see* particle density
desert, 1, 17, 80
dielectric constant, 21
dike, 80
directional-hemispherical reflectance, 81
double refraction, *see* birefringence
dune, 14, 29, 30, 80
dune field, 14

e-ray, *see* extraordinary ray
eccentricity, 75, 76, 91, 92
extended boundaries, 42, 51, 53, 55, 56, 59
extinction coefficient, 20
extinction index, 20
extraordinary ray, 21, 26, 27

FIFE, *see* First ISLSCP Field Experiment
First ISLSCP Field Experiment, 80
Fresnel equations, 23, 51, 56

geometric attenuation coefficient, 54, 65–68, 73, 75, 76
geometric extinction coefficient, 66
geometrical ray optics, *see* ray optics
goethite, 8, 9, 25, 26, 39, 41, 44, 46, 47, 49, 83
  chemical formula, 26
  concentration, 45, 47
  density, 26, 41
  ratio relative to hematite, 46
  refractive index, 28, 35
goniophotometry
  virtual, *see* virtual goniophotometry
gypsum, 8

height map, 14
hematite, 8, 9, 17, 25–27, 30, 39, 41, 44, 46, 47, 49, 83
  chemical formula, 26
  concentration, 45, 46
  density, 26, 41
  ratio relative to goethite, 46
  refractive index, 27, 28, 34
hemispherical-conical reflectance, 81
hemispherical-directional reflectance factor, 81
Henyey-Greenstein phase function, 15, 16
human activity, 11
humus, *see* organic matter
hydrogen bonding, 9
hydrosol, 28

illite, 9, 26, 30
ilmenite, 9
International Soil Science Society, 6
iron oxide, 8–10, 25
  concentration, 45, 83
ISSS, *see* International Soil Science Society

Jet Propulsion Laboratory, 80
JHU, *see* John Hopkins University
John Hopkins University, 80
joint probability density function, 61
JPL, *see* Jet Propulsion Laboratory

kaolinite, 9, 26, 30, 39, 41, 44, 46, 47, 49
  chemical formula, 26
  density, 26, 41
  refractive index, 37
Kramers-Kronig analysis, 27
Kubelka-Munk theory, 16
Königsberger equations, 28

Lambert's Law, 57
Lambertian, 8
limonite, *see* goethite
logarithmic normal distribution, 49, 54, 72

magnetite, 9, 26, 39, 41, 44, 80

chemical formula, 26
concentration, 45
density, 26, 41
refractive index, 36
masking, 17
Maxwell Garnett theory, 21, 44
measurement of appearance, 3, 39, 87
Mie theory, 40
Monte Carlo, 15, 77, 78
mud, 14

normal distribution, 49, 54, 72

o-ray, *see* ordinary ray
opposition effect, 56
ordinary ray, 21, 26, 27
organic matter, 5, 10, 11, 18, 88
orientation, *see* particle orientation

parent material, 8, 9
particle density, 48, 96
particle distribution, 59, 60, 63, 67, 74–76
abstract, 62
continuous, 63, 66, 67
discrete, 66
fixed, 64, 66
separable, 67–70, 72
particle geometry, 60, 62
particle orientation, 70, 74
particle size distribution, 5, 8, 29, 49, 54, 55, 57, 73, 83
phase function, 3
Henyey-Greenstein, 15, 16
polarization, 17
pore space, 5, 9, 31, 39, 42, 53, 56
porosity, 31, 41, 42
probability density function, 60, 67, 68, 71
normal, 54, 73

quartz, 8, 9, 17, 26, 27, 39, 41, 44, 46, 47, 50
chemical formula, 26
density, 26, 41
refractive index, 26, 27, 33

random variable, 63
canonical, 54, 55
exponential, 54, 60–63, 66, 67
normal, 29, 50
ray optics, 40
red ochre, *see* hematite
redness rating, 16
reflectance, 8
at a plane surface, 23
directional-hemispherical, 81
hemispherical-conical, 81
transverse electric, 24
transverse magnetic, 24

unpolarized light, 24

reflectance factor

hemispherical-directional, 81

reflection

internal, 9

multiple, 17

retro-reflection, 8, 86

specular, 8, 17

refractive index, 9, 27

complex, 19–23, 26, 44, 57

imaginary part, 20

real part, 20

relative, 23

remote sensing, 2

retro-reflection, 8, 86

Riley sphericity, 10

river sand, 9

RMS error, 81, 82

RMSE, *see* RMS error

rock, 5, 6, 8, 29

root-mean-square error, *see* RMS error

roughness

particle, 44

surface, 11, 17

roundness, 9, 10, 29, 30, 41, 44

separable

function, 67

particle distribution, 67–70, 72

shadowing, 17

silicate, 8

snow, 14

soil separate, 50

soil separates, 5, 49

clay, 5–7, 29, 41

sand, 5–7, 29, 41

silt, 5–7, 29, 41

soil texture, 5, 7, 31, 41, 50, 88

sand, 6, 7, 29

spectral library

ASTER, 80

TEC, 80

USGS, 79

spectrophotometry

virtual, *see* virtual spectrophotometry

specular reflection, 8

sphericity, 9, 29, 30, 41, 48, 49, 54, 70, 72, 73

projection, 9

Riley, 10, 43, 73

spheroid, 76

oblate, 75, 90, 92

prolate, 43, 48, 54, 55, 70, 72, 73, 75, 90, 91

surface area to volume ratio, 48, 72

TEC, *see* U.S. Army Topographic Engineering Center
texture mapping, 1, 5
texture triangle, 7
tillage, 11
transverse electric, 24
transverse magnetic, 24

U.S. Army Topographic Engineering Center, 80
United States Department of Agriculture, 5, 6, 29
United States Geological Survey, 79, 80
  spectral library, 79
unpolarized, 24
USDA, *see* United States Department of Agriculture
USGS, *see* United States Geological Survey

virtual goniophotometry, 79
virtual spectrophotometry, 79, 81
volumetric water content, 42

water, 5, 8, 9, 11, 16, 26, 31, 39, 41, 42, 53, 88
  chemical formula, 26
  density, 26
  refractive index, 26, 32
water content, 31
weathering, 5
  aeolian, 9

yellow ochre, *see* goethite